The origin of cold gas in the center of massive elliptical galaxies

David Peter Schlachtberger

Munich 2014

The origin of cold gas in the center of massive elliptical galaxies

Master Thesis

at the

Ludwig–Maximilians–Universität (LMU) München

submitted by

David Peter Schlachtberger

(Matr. Nr.: 10108076)

born on April 27, 1988 in Starnberg

supervised by
Prof. Dr. Andreas Burkert

and
Rhea-Silvia Remus, Klaus Dolag

Munich, May 15, 2014

Evaluator: Prof. Dr. Andreas Burkert

Contents

Contents

1. Introduction

New telescopes like ALMA will allow a very detailed observation of the cold and molecular gas content of elliptical galaxies. Already existing observations like ATLAS[3D] already indicate that a large fraction of elliptical galaxies contain a significant amount of cold gas. In this thesis we want to study the origin of this cold gas by using re-simulations of elliptical galaxies at very high resolution within a cosmological framework.

In chapter 2 we will present the selection of the four halos from the parent simulation, explain the generation of the initial conditions for the re-simulations and discuss numerical issues that need to be taken into account when re-simulating the halos with Dark Matter and Gas particles at high resolutions. The scientific results of our analysis of the present-day properties of those re-simulated galaxies, their mass accretion and star formation histories, their circularity-evolution and finally the origin of their cold gas content at $z = 0$ are presented in chapter 3. A summary and discussion of our results is provided in chapter 4.

1.1. Cosmological background and galaxy formation

In recent years, modern cosmology developed a concordance model of the large scale structure and dynamics of the universe. It assumes that the gravitating matter in the universe consists only to a small fraction of visible, baryonic matter. The dominant part is *Dark Matter* (DM), which interacts only gravitationally, but has been detected with several indirect methods, e.g. through its influence on the velocity profile of spiral galaxies (Clemens, 1985).

Another important ingredient of this model is Hubble's discovery of 1929 (Hubble, 1929) that there is a linear velocity-distance relation

$$v = H_0 r \tag{1.1}$$

for galaxies, with H_0 known as the *Hubble constant.* It implies that, on average, any two galaxies move away from each other at a speed v that is proportional to the distance r between the objects. This is a natural consequence if the space between them expands over time. An observable effect of this is that the wavelength of light gets longer, and therefore red-shifted, as it travels through the expanding space. The fraction by which the emitted wavelength λ_e is longer than the observed wavelength λ_o is called *redshift z*

$$z = \frac{\lambda_o - \lambda_e}{\lambda_e} \tag{1.2}$$
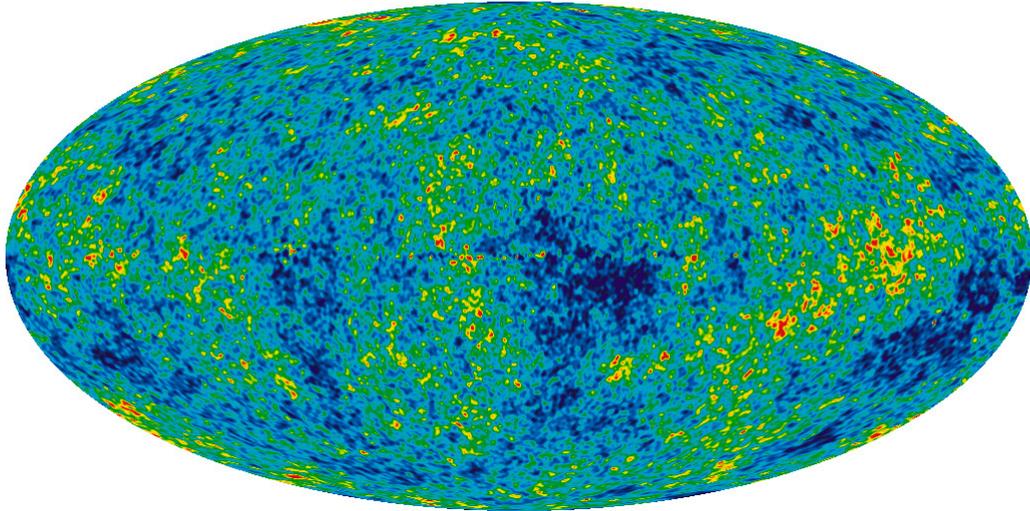
Figure 1.1.: A high resolution map of the CMB temperature variations over the whole sky as observed by the WMAP satellite (Bennett et al., 2013). These fluctuations have grown over time and eventually led to the cosmic structure observed today. Image courtesy of the NASA / WMAP Science Team.

and is a dimensionless measure of time. As the universe is expanding, it is assumed that it started as a *Big Bang* and H_0^{-1} sets a timescale for its age. Modern observations of Type 1a supernovae (Riess et al. (1998), Perlmutter et al. (1999)) and the Cosmic Microwave Background (CMB) radiation (Komatsu et al., 2011), an echo of the very early universe, even give strong indications that the expansion of the universe is accelerating. This led to the introduction of a cosmological constant Λ, usually associated with the yet little understood *Dark Energy*, often interpreted as vacuum energy fluctuations (Longair, 2008, p. 207).

The resulting best fit model is called ΛCDM, which assumes a homogeneous and isotropic universe with a flat curvature, where todays total energy density is dominated by the energy density of dark energy $\Omega_\Lambda = 0.73$, and which contains a significant amount of DM with energy density $\Omega_{DM} = 0.23$. It is described by a small set of cosmological parameters, that can be fitted by observations of the CMB (Hinshaw et al., 2009).

Detailed studies of the power spectrum of the CMB reveal that the universe was indeed very isotropic and homogeneous at very early times, as assumed in the cosmological model. But it also had small density fluctuations of the order of 10^{-5} around the mean (see figure 1.1). The fact that we can observe these perturbations on very small scales implies that DM must have been dynamically cold (CDM) at the time of recombination, because the alternative of hot DM would imply that fluctuations on the smallest scales would be smeared out as the hot DM would have high velocities and could escape from small potential wells.

These early fluctuations are considered the seeds of todays structures like galaxies, clusters, and the cosmic web. They grow in a hierarchical order where, after an
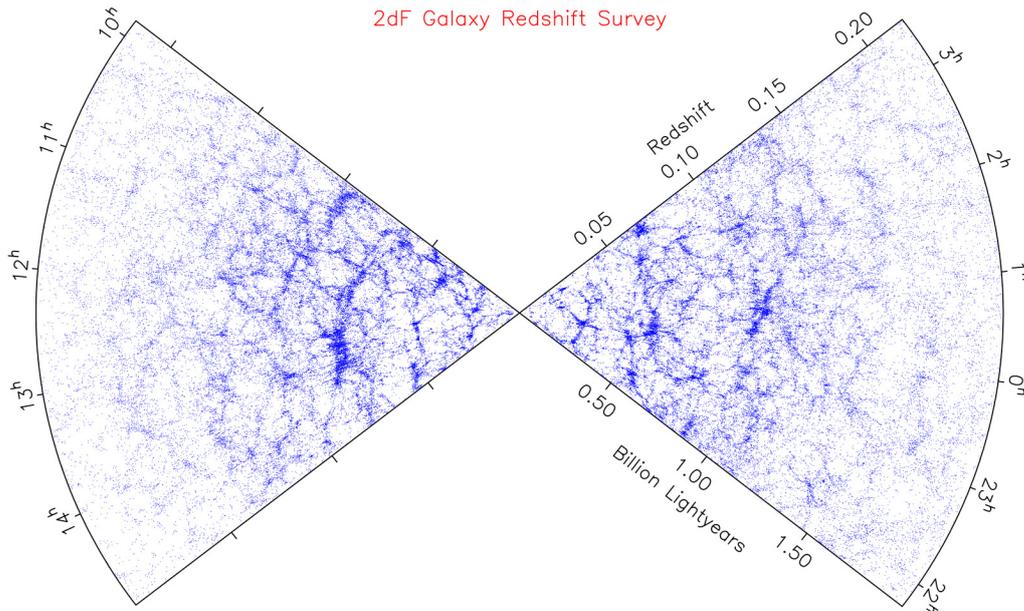
Figure 1.2.: The distribution of galaxies on a scale of $600Mpc$ as observed by the 2dF Galaxy Survey (Colless et al., 2001). The cosmic web is visible as a large scale structure with filamentary high density regions enclosing voids of low density. Image courtesy of the 2dFGRS team.

initial linear growth of the density perturbations by self-gravity, the smallest scales collapse first and then form larger and larger structures. Simulations that predict this formation process (e.g. *Millenium* by Springel et al. (2005)) are in good agreement with observations of the local cosmic web (Colless et al. (2001), see figure 1.2). This web is formed by thin sheets or filaments with a relatively high density of galaxies. The filaments are attracted towards the local potential well where they contribute to the accretion of the locally most massive object. Since this web is essentially self-similar, this happens on many scales. At places where the density is highest, clusters of galaxies can have hundreds of members, but in the low density environment of a void between large filaments, single galaxies can be the local attractor and be fed by streams along small filaments.

The much smaller baryonic mass of the universe follows this structure formation and falls into the local potential wells created by the DM where it forms, through various physical processes, the galaxies we can observe today.

1.2. Elliptical galaxies

Galaxies are very complex and dynamical objects that exist in a large variety of shapes and their formation and evolution are difficult to understand. Before the advent of modern, precise astronomical instruments, they were classified purely based on their morphological appearance. The classical scheme called the *Hubble sequence*

1. Introduction
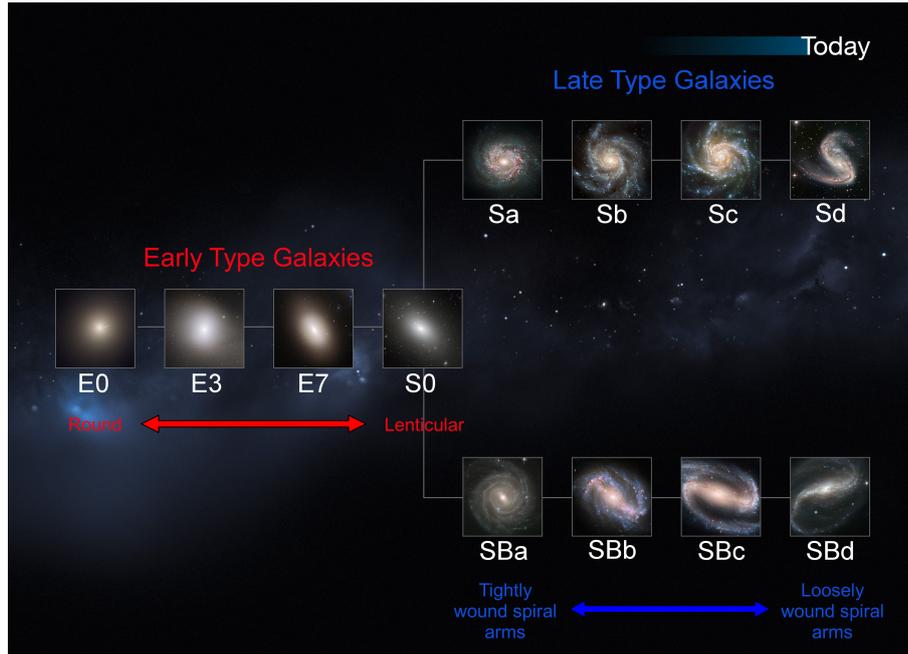
Figure 1.3.: The Hubble sequence of early and late type galaxies. Image courtesy of NASA, ESA, M. Kornmesser.

(see figure 1.3) was introduced by Hubble (1936) and distinguishes between two main classes, elliptical and spiral galaxies.

Hubble's original idea was that the roundish and rather smooth ellipticals would evolve into the more structured spirals, so he called them early-type (ETG) and late-type (LTG) galaxies, respectively. ETGs also include a transitional element between ellipticals and spirals, the lenticular galaxies (S0). They are shaped like (often thick) disks without prominent spiral arms but have otherwise similar properties to ellipticals. The definition as early- and late-type galaxies is still in common use even though we nowadays assume that their evolution is usually the other way around.

Today, ETGs are often associated with having dominantly red optical colors due to their old stellar populations, a relative lack of cold gas, dust and young stars, and a lower metallicity, when compared to spiral galaxies which appear blue due to more recent star-formation. This difference in the two types of galaxies can best be seen in a color-magnitude-diagram like the one from the Sloan Digital Sky Survey (SDSS) of galaxies shown in the left panel of figure 1.4. There is a clear dichotomy between ETGs and spirals. The early type galaxies have dominantly red colors and thus reside mainly in the upper part of the diagram in a *red sequence*. The spirals are generally bluer and are therefore located in the lower part of the diagram and form the *blue sequence*. The low number of galaxies in the so called *green valley* between the two types of galaxies indicate that the transition from the blue to the red sequence must be rather rapid. From a dynamical point of view, the elliptical
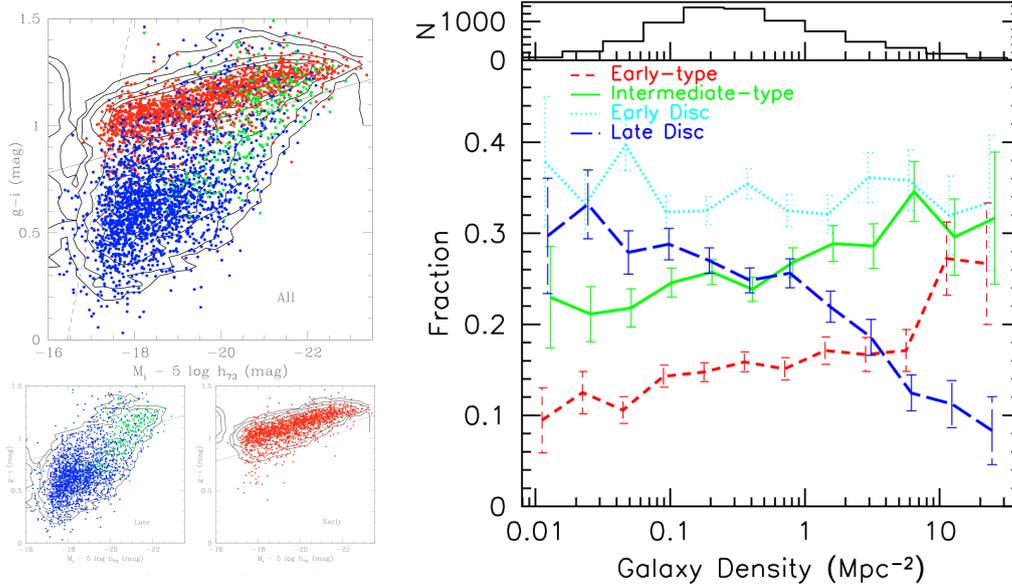
Figure 1.4.: *Left*: Figure 3 of Gavazzi et al. (2010). Color-Magnitude-diagram of the galaxies in the Coma supercluster color-coded by their Hubble type: red = early-type galaxies; blue = disk galaxies; green: bulge galaxies. *Right*: The observed morphology-environment relation for four types of galaxies, as presented in figure 12 of Goto et al. (2003). The dashed red line shows that the fraction of ETGs is low in low density environments and gets larger at the highest densities.

galaxies have mainly unordered stellar orbits with a high velocity dispersion, whereas the spirals are rotationally supported against gravitational collapse.

Elliptical galaxies are found in all kind of environments even though they are relatively rare in the *field* where the density of galaxies is low, and are seen more often in the dense environment of *clusters of galaxies*, as shown by Goto et al. (2003) from observational data (see right panel of figure 1.4). This increase in the fraction of elliptical galaxies with increasing environmental density together with the strong decrease in the fraction of disk type galaxies with increasing environmental density gave further indication for a morphological transition of late type galaxies into early type galaxies through merging, as the likelihood for mergers strongly increases with environmental density.

Elliptical galaxies cover a large range of masses. The smallest are *dwarf ellipticals* like M32, a prominent companion of the Andromeda galaxy, with a mass of $1.3 \times 10^9 M_\odot$ (Richstone and Sargent, 1972). The largest ellipticals are the most massive galaxies in the universe with stellar masses around $M_\star = 1 - 3 \times 10^{12} M_\odot$ (Kravtsov et al., 2014), which are located in the center of galaxy clusters and are therefore called *brightest cluster galaxies* (BCG). For comparison, NGC 1961, one of the most massive known spiral galaxies has a stellar mass of about $3 \times 10^{11} M_\odot$ (Rubin et al., 1979; Anderson and Bregman, 2011). Most BCGs are dominated by an old stellar population with higher metallicities than field ellipticals (Loubser et al., 2009). They

have round shapes and they show basically no evidence for cold gas or dust. But there are also some BCGs with strong cold flows, for example in the Phoenix cluster, where the BCG has a starburst of $800 M_\odot/\mathrm{yr}$ and contains currently a molecular gas mass of $M(H_2) = 2.2 \times 10^{11} M_\odot$ (McDonald et al., 2014). These BCGs are normally in the centers of cool core clusters where the cold gas that fuels the starformation most likely cooled rapidly out of the very dense hot intracluster medium (Fabian and Nulsen, 1977; McNamara et al., 2006; McDonald et al., 2012).

1.2.1. Formation and evolution

There are several known mechanisms for the formation of elliptical galaxies. In the following we describe some of those considered most dominant in a cosmological context.

The fact that the probability of finding elliptical galaxies is highest in regions of high density and at high masses suggests that they formed through merging of smaller objects, in accordance with the picture of hierarchical growth. This would also explain several of the properties stated above, e.g. their relative lack of internal structure. Simulations of idealized mergers (Hernquist, 1992; Naab et al., 2006; Johansson et al., 2009) showed that if two galaxies with similar masses get close to each other, although they do not collide due to their sparse distribution of stars, they merge and get heavily disturbed, but then settle into a new equilibrium relatively fast through a process called *violent relaxation* (Lynden-Bell, 1967). The strong interactions lead to heavy phase mixing of stellar orbits and a complete redistribution of their potential energies. This new equilibrium is then dominated by random motion and the high velocity dispersion that is observed in ellipticals. The gas that the initial galaxies brought is collisional, however, and can distribute its energy very efficiently, thereby looses most of its angular momentum and gets funneled to the potential minimum in the center of the new system. Physical mechanisms like the energetic feedback from a burst of starformation or an active galactic nucleus (AGN) can then heat up the gas and even eject it from the galaxy. If this happens efficiently it can quench starformation and leave the newly formed elliptical gas-poor. Due to the limited lifetime of the bright and massive blue stars, the galaxy gets dominated by red stars on the order of $1 - 10$ Gyrs if it can not form sufficiently more new stars.

Observations find clear indications for major mergers at low redshifts, so this is a still ongoing process of formation of ellipticals. Outstanding examples of interacting galaxies are the *mice* galaxies (NGC 4676A+B) and the *atoms-for-peace* galaxy (NGC 7252) (see figure 1.5). The latter is also a good example of the shell structures that develop in late, gas poor *dry* mergers as predicted by Hernquist and Quinn (1988).

If the merging happens at high redshifts $z \sim 1.5$, the progenitors are likely to be rich in gas. In some cases the gas fraction can be as high as $50\% - 65\%$ at that redshift (Daddi et al., 2010). The result of such an early, *wet* merger is not necessarily an elliptical galaxy but can also be a spiral, possibly with a spherical
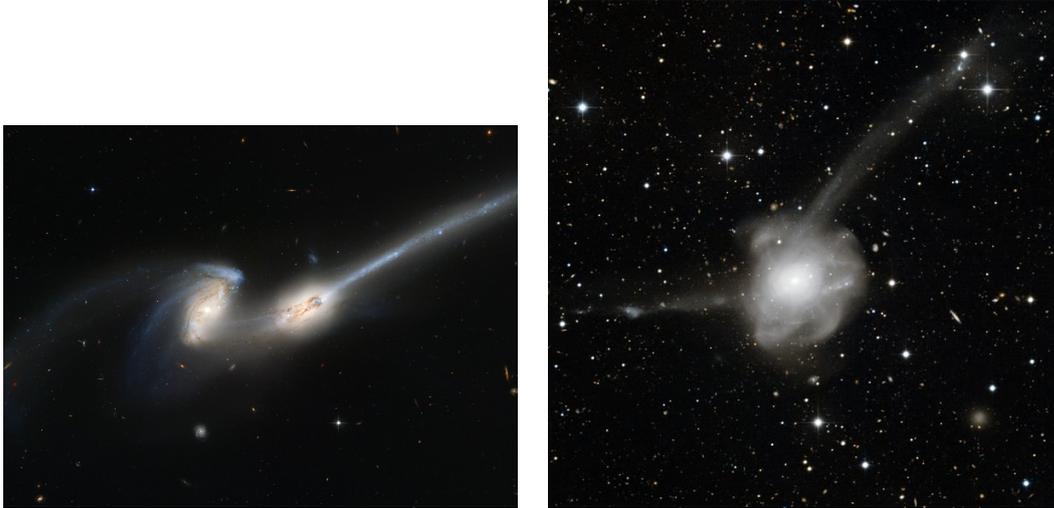
Figure 1.5.: Left panel: the two colliding galaxies NGC 4676A+B as seen by the ACS camera on the HST (Credit: ACS Science & Engineering Team, NASA). Right panel: the shell structures formed by a recent merger in NGC 7252 as seen by the Wide Field Imager on the MPG/ESO 2.2-metre telescope at ESO's La Silla Observatory in Chile (Credit: ESO).

bulge component as not all the cold gas gets consumed or destroyed but can settle again into a disk.

Especially in low density environments, it is possible that an object already merged or gravitationally bound all neighboring systems at high redshifts, and does not experience any further significant merging later on, but only grows due to smooth accretion in size but not significantly in mass. Ponman et al. (1994) observed remnants of such systems called *fossil groups* and find that they also have old stellar populations and relax dynamically over the course of a few 10^9 yrs into massive elliptical galaxies.

Major mergers are not the only way of forming massive galaxies as observational results by van Dokkum et al. (2008) and van de Sande et al. (2013) and cosmological simulations (Naab et al., 2009; Oser et al., 2010) indicate. They find a significant amount of compact massive galaxies with stellar masses $M_\star \sim 2 \times 10^{11} M_\odot$ and effective radii $r_{eff} \sim 0.9 kpc$ at $z \gtrsim 2$. As $M_\star$ is already of the order of the most massive ellipticals observed today, but their sizes are a factor 5 smaller, they suggest a growth mechanism via multiple minor mergers, which tend to puff up the galaxy to the correct size by adding mass preferentially to the outskirts without increasing the mass as much as a major merger would.

1.2.2. Dynamical properties

Recently, a new survey of local elliptical galaxies was done by the ATLAS[3D] project (Cappellari et al., 2011a). It is as a complete, volume-limited sample of 260 nearby morphologically selected early-type galaxies with stellar masses $M_\star \gtrsim 6 \times 10^9 M_\odot$.

The ETGs were observed in a broad range of wavelengths and also have detailed two-dimensional kinematics of the stellar population and of cold atomic and molecular gas, and of ionized gas. Emsellem et al. (2011) find a distinction of ETGs into different classes based on their stellar kinematics, that is likely correlated to their formation history. Fast rotators are often nearly oblate and resemble thick, gas-poor disks that where probably not assembled in a major merger event. This is the dominant class especially among less massive systems. The more massive galaxies tend to be slow rotators with a more spherical shape and kinematic properties that indicate a more violent past, e.g. with major mergers (see Cappellari et al. (2011b)).

1.3. Gas in elliptical galaxies

Elliptical galaxies are known to have a predominately old stellar population, little atomic and molecular gas, and thus little ongoing starformation. Since all objects where gas-rich at high redshifts, the ellipticals must have removed most of the cold gas during their evolution. There are different mechanisms to deplete the cold gas reservoir of a galaxy. They include gravitational interactions, like the major merger scenario described above, that increase the starformation rate, but also energetic feedback from AGN or supernovae that destroy the cold gas and heat it to high temperatures, and a combination of these effects. Massive ellipticals especially in dense cluster environments often have a halo of hot gas that is observable at X-ray wavelengths. It can shock-heat infalling gas to its high temperature, thus preventing further accretion of cold gas.

However, beginning in the early 1990's, several ellipticals have been detected in various tracers of cold, molecular gas, e.g. CO (Lees et al., 1991). This shows that todays early-type galaxies are not completely devoid of cold gas, even though they are relatively poor in cold gas when compared to spirals. The recent large survey of massive elliptical galaxies by the ATLAS^{3D} project revealed that a surprisingly large fraction of at least $22 \pm 3\%$ contain a significant amount of cold gas (Young et al., 2011). In the most recent publications of the project they find an even higher fraction of at least 40% (Young et al., 2013). The origin of this cold gas is not yet well understood.

It could come from internal stellar mass loss as discussed e.g. by Mathews and Brighenti (2003). They propose that the cooling times of the gas that is lost by evolving stars can be short especially in the centers of massive ellipticals. Massive stars can return approximately half of their mass back to the interstellar medium over their lifetime, so this might be enough to generate significant amounts of cold gas. This scenario is similar to a chase where the central gas of a massive hot halo starts to condensate and cool due to its high density, which is recently observed in cool core clusters (McDonald et al., 2012).

The cold gas could also be acquired from external sources such as stripping or merging with other galaxies, or via a more smooth accretion along filaments (Dekel et al., 2009; Nelson et al., 2013). In contrast to the first considerations of this

scenario in the early 1980's, that assumed that all such infalling gas gets shock-heated to the virial temperature of the halo $T \sim 10^6 K$, Kereš et al. (2005) find in simulations that also *cold mode* accretion is important. It is named so because the gas never gets shocked and stays colder than $T < 10^5 K$. The cold mode dominates in the low mass regime for halo masses $M_{halo} \lesssim 10^{11.4} M_\odot$ and occurs often along the direction of filaments. The classical *hot mode* is more common for massive galaxies and usually spherical. This indicates that galaxies with less massive hot halos can only shock a fraction of the cold, dense gas that is transported in filaments, which makes this a viable method for cold gas accretion.

The origin of the cold gas can be distinguished observationally via its kinematic trace, as done by Davis et al. (2011) for the ATLAS[3D] sample. Gas of internal origin must have a similar angular momentum orientation as the stars. External gas can have a random angular momentum orientation and is likely misaligned. Davis et al. (2011) find a strong dependence of the alignment with the environment. Ellipticals in a dense environment have predominantly aligned molecular gas, indicating an internal origin, whereas roughly half of the field ellipticals show indications for an origin from mergers and accretion.

Young et al. (2011) report from the ATLAS[3D] sample that the detected masses of cold gas in the early-type galaxies range from $10^7 - 10^9 M_\odot$ and are relatively independent of internal properties of the galaxies. The largest cold gas masses of $10^9 M_\odot$ are similar to that of the Milky Way which is somewhat unexpected for elliptical galaxies. Their host galaxies tend to lie is relatively low density environments, indicating that external accretion is an important way for them to acquire cold gas.

There is clear observational evidence for significant masses of cold gas in a surprisingly large fraction of elliptical galaxies. We want to understand the origin of this cold gas, as this might allow important insights into the formation process of todays massive ellipticals. This is the main motivation for this thesis.

1.4. SPH-Simulations

Numerical simulations are a very powerful tool to study cosmology and the evolution of galaxies in the chaotic, non-linear phase of the collapse of structures. The general approach is to model dark matter (DM) and stars as perfect, collisionless fluids as the collision-timescales at feasible resolutions are assumed to be longer than the age of the universe. The diffuse baryonic gas that is composed mainly of hydrogen and helium is treated with the hydrodynamical equations applicable to a collisional fluid under gravity.

This has been implemented with two different numerical techniques. One is based on the Eulerian approach to discretize the fluid onto a spatially fixed grid and to solve the fluid equations for each grid-point. This method is called adaptive mesh refinement (AMR; Teyssier (2002)). The other numerical technique uses the Lagrangian approach to follow the fluid by to discretizing it into moving particles. The hydrodynamical equations are then solved by averaging over nearest neighbors.

1. Introduction

This is called smoothed particle hydrodynamics (SPH; Monaghan (1992)) and is our method of choice. It has been implemented in the GADGET-code by Springel et al. (2001b); Springel (2005) together with an intrinsically energy-conserving formalism that allows to solve the gravitational N-body problem very precisely and efficiently.

2. Simulations

A cosmological simulation box provides a large volume of self-consistent cosmological environment but can only be simulated at moderate spacial resolutions to keep computational costs reasonable. To achieve high resolutions within a cosmological framework, we focusing on a smaller region within this volume. These "zoom-in simulations", or "re-simulations", are useful to study the detailed formation history of one object of interest at a time.

This chapter describes the selection of objects in section 2.1, the generation of their high resolution initial conditions in section 2.2, the re-simulations that were done during the course of this thesis are introduced in section 2.3, and the problems encountered in those steps are discussed in section 2.3.4.

2.1. Object selection

The main goal of this thesis is to understand the origin of the cold gas that can be observed in some of todays elliptical galaxies. Therefore , we need simulations of spheroidal galaxies that have sufficient resolution to resolve the gas in their very center. The very first step to achieve this is to find a way to select objects that are likely to be ellipticals that contain cold gas at $z = 0$.

2.1.1. The parent simulation

The objects of interest for this study were selected from a cosmological N-Body simulation called DIANOGA described by Borgani and Viel (2009). It is based on a flat Λ cold dark matter (ΛCDM) cosmological model with cosmological parameters $\Omega_\Lambda = 0.76$ the cosmological constant density parameter, $\Omega_m = 0.24$ the matter density parameter, $\Omega_{bar} = 0.04$ the fraction of baryons, $h = 0.72$ the Hubble parameter, $\sigma_8 = 0.8$ the rms matter fluctuations, and $n_s = 0.96$ the spectral power-law index. We use the usual convention of writing the present day Hubble constant as $H_0 = 100\,h\,\mathrm{kms}^{-1}\mathrm{Mpc}^{-1}$. DIANOGA was performed with the TreeSPH code GADGET-3, an updated version of the GADGET-2 code by Springel (2005), to simulate a periodic dark matter (DM) only box with a comoving size of $L_{Box} = 1h^{-1}Gpc$ per side, and $N_{Box} = 1024^3$ particles of mass $m_{DM,Box} = 6.2 \times 10^{10}h^{-1}M_\odot$. We call this the "parent simulation".

Object name	M_{vir} $[10^{13}h^{-1}M_\odot]$	r_{vir} $[h^{-1}kpc]$	d_{eff} $[h^{-1}Mpc]$	$d_{Cluster}$ $[h^{-1}Mpc]$	Selection Method
Bat	1.085	492.5	18.2	41.3	2nd
Frogout	1.265	480.5	18.3	34.2	2nd
Pig	1.042	451.4	3.3	69.3	1st
Frog	1.253	487.1	10.8	43.4	3rd
D1	1.253	492.6	4.5	52.5	1st

Table 2.1.: The target objects chosen with our different methods. $d_{eff} = min(d/(r_{vir} + r_{vir,neigh}))$, $d_{Cluster}$ is the distance to the next nearest cluster of galaxies.

2.1.2. Galaxy selection

In this thesis we focus on objects with a dark matter halo mass in the range of $M_{Halo} = 1 - 1.5 \times h^{-1}10^{13}M_\odot$, which ensures to find an object of this shape. We chose a very large box as the parent simulation because it samples a considerable volume of the observable universe and therefore includes large structures and large voids which are more uncommon in smaller boxes. These low density regions can contain very isolated ellipticals which we select as our zoom targets, because they are usually cheaper to re-simulate due to the fact that the volume that has to be re-simulated with high resolution is smaller for isolated objects then for objects in dense environments. In addition, the likelihood for an elliptical galaxy to still contain a significant amount of cold gas is higher in less dense environments because the probability for violent interactions that destroy the cold gas content is lower.

In order to find the target candidates in the parent simulation, we used the halos identified by the halo-finder SUBFIND ((Springel et al., 2001a)) integrated in GADGET (Springel, 2005) and applied the above mentioned mass cut for M_{Halo}. In order to find the most isolated objects in this mass range we used three different selection approaches. The selected halos are listed in table 2.1.

The first method is to calculate for each target candidate the minimum distance d_{obj} to the nearest heavier object with mass $M_{obj} > 2 \times 10^{13}h^{-1}M_\odot$ and also the minimum distance $d_{cluster}$ to the nearest cluster with $M_{cluster} > 10^{14}h^{-1}M_\odot$. The left panel in figure 2.1 shows these values for all candidates with $d_{cluster} > 10Mpc$. We then chose the most extreme outliers, labeled in the figure, as re-simulation targets D1 and Pig (see table 2.1). This simple method is designed to ensure that the target object dominates the local potential well, while being far way from the influence of the nearest cluster. However, it did not proof to be sufficient to reliably find isolated ellipticals, because it does not account for nearby objects that are only slightly less massive than the target galaxy. The apparently most isolated object in this figure, marked in orange and called D1, had to be discarded later because it turned out to be a group of smaller galaxies rather than a single galaxy (see lower left panel of figure 2.3.

The second method overcomes this difficulty by calculating distances $d_{eff} = min(d/(r_{vir} + r_{vir,neigh}))$ in units of the virial radius r_{vir} of a halo and it's neigh-
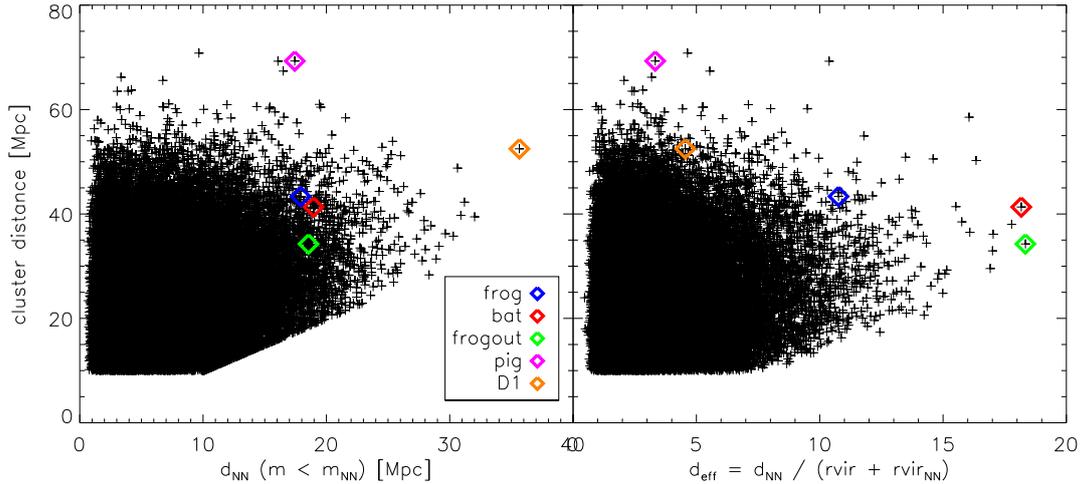
Figure 2.1.: Halo selection criteria: *Left:* The distance to the next cluster with $M_{clust} \geq 10^{14} h^{-1} M_\odot$ versus the distance to the next halo with more than $M_{obj} > 2 \times 10^{13} h^{-1} M_\odot$ for all halos in the mass range of $1 - 1.5 \times 10^{13} h^{-1} M_\odot$. Colored symbols mark the five different halos chosen with the different methods. *Right:* Same as left panel but for d_{eff} instead of d_{obj}

bor. This penalizes large and heavy neighbors which have a large region of influence $r_{infl} \approx 3$–$4 \ r_{vir}$ that could blow up the required Lagrangian region, making the simulation more expensive. The right panel in figure 2.1 shows the distribution of d_{eff} of all halos. There is a tail of a few outliers with very high values of d_{eff}. We selected the two objects with the largest values as re-simulation targets, called Bat and Frogout.

The third method is based on direct void detection. In his Bachelor thesis, F. Stecker used the void finder ZOBOV to identify voids in our parent simulation. He found that our targets are located at the edges of voids, which can be seen in the right panels of figure 2.2. For one object, Frogout, which is located at the edge of a large void with a diameter $d_{void} \approx 100 Mpc$, he found another candidate halo with a mass of $M \approx 10^{13} M_\odot$ in the center of this void by visual inspection (see figure 2.2) which we included as Frog in our sample.

Figure 2.3 shows the three orthogonal projections of the environment in a $40 \, h^{-1}$ Mpc box around each of our sample galaxies selected with the first two methods. The blue diamonds are objects in our mass cut range, green diamonds mark objects with a larger mass, and red circles show the virial radius of every object found by the FoF algorithm. Only objects within a sphere of radius $r_{10} = 10 h^{-1} Mpc$ around the central target halo, marked as black circle, are plotted in the lower right panel. As can be seen in Figure 2.3a and 2.3b, the objects selected with the second method are very isolated with only a few neighbors around them and no object resolved in the parent simulation closer than r_{10}. However, figure 2.3d shows that the first approach fails because it can not guarantee that there is no other object of similar
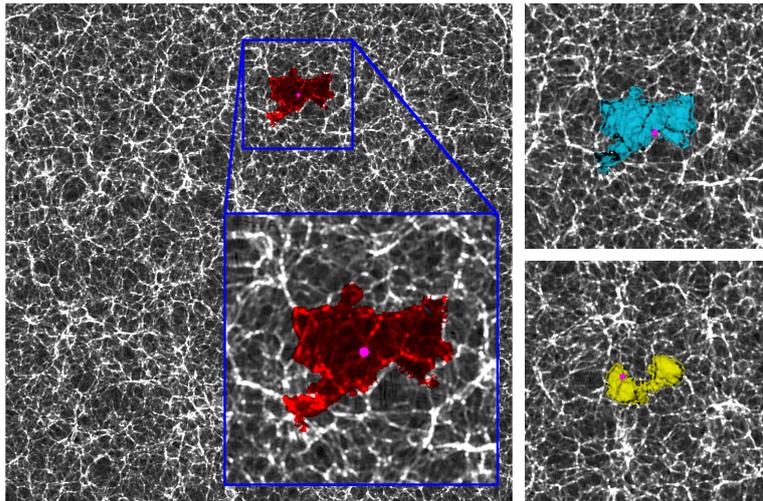
Figure 2.2.: Slice through the DIANOGA parent simulation, DM marked by white points. *Left:* full box with box length of $1h^{-1}Gpc$. Marked in red is the void which has one of the targets, Frog, in its center shown as pink point. *Upper Right:* A $300h^{-1}Mpc$ area cut out of the full box centered around the same void as in the left panel, marked in blue. At its border the target object Frogout is marked as pink dot. *Bottom Right:* Same as the upper panel but centered around the void (yellow area) with the target object Bat marked at its border in pink. Image courtesy of F. Stecker.

mass in the vicinity as it is the case for the target halo D1. The other object selected with this method (see figure 2.3c) is also not isolated but it has at least no other object of similar mass within the r_{10} sphere but shows a peculiar environment where several small objects are lined up in a string around the object, indicating that it is the local attractor of a filamentary structure. Due to its interesting environment we keep the halo Pig in our sample.

2.2. Zooming

After we identified the targets in the parent simulation, we re-simulated them individually. This is an iterative process of selecting an appropriate region around the object, running the simulation with an increased spatial and mass resolution in this area, then checking for contamination with low resolution (LR) particles, and finally adapting the initial region if intruders (lower mass particles) are present in the high resolution area. The steps required for this procedure are described in the following in detail.

2.2.1. First guess

We begin by selecting all particles in the full box at $z = 0$ that are inside a sphere of radius r_{tr} around the targeted object. For this first guess we chose a trace radius

(a) Bat

(b) Frogout

(c) Pig

(d) D1
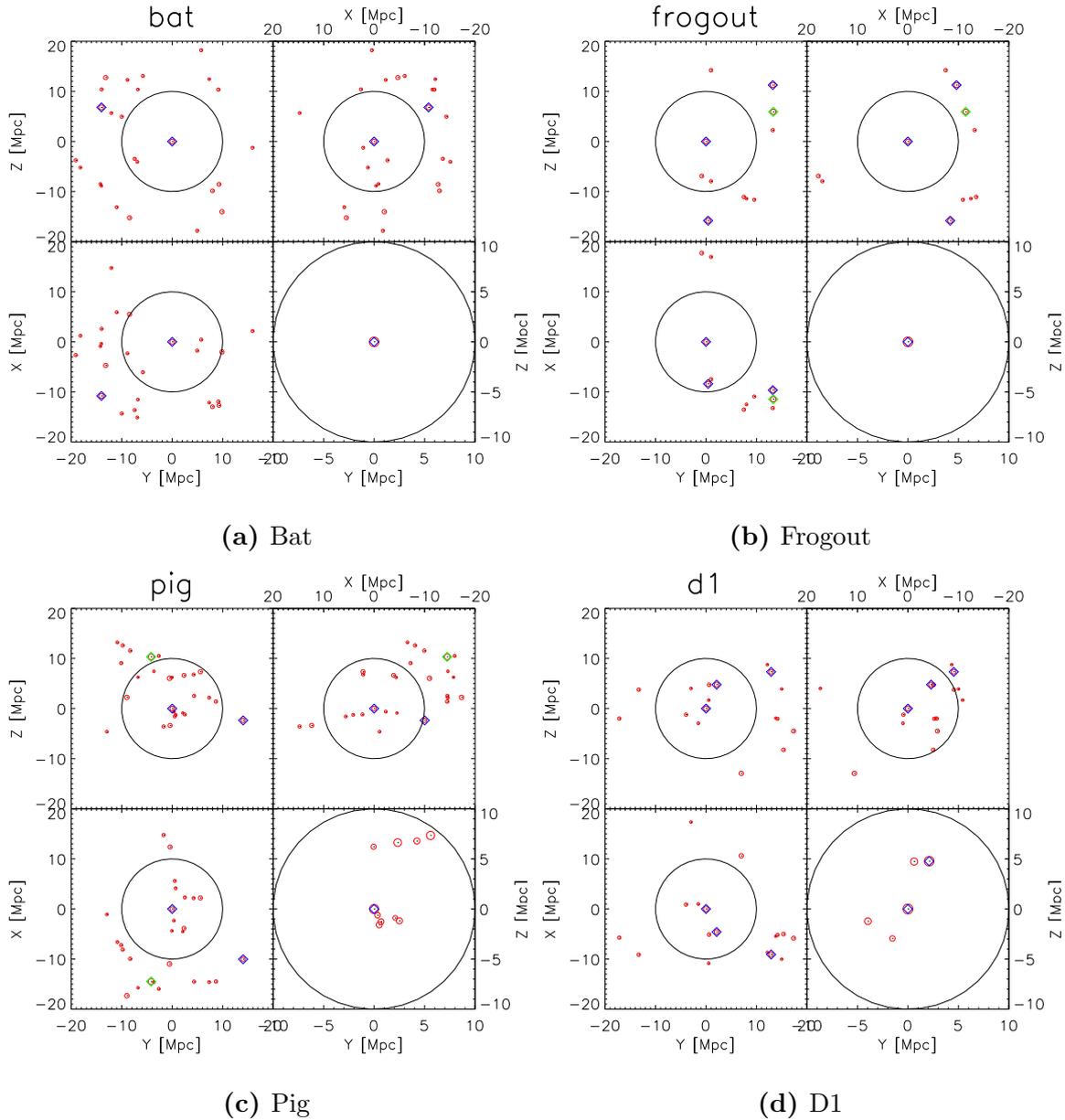
Figure 2.3.: Environments for the four halos chosen with the first two selection criteria. Red circles: virial radii of all objects found in the parent simulation within the shown area. Blue diamonds: Halos with $1 - 1.5 \times 10^{13} h^{-1} M_\odot$. Green diamonds: Halos with $M > 1.5 \times 10^{13} h^{-1} M_\odot$. Black circles: $r_{10} = 10 h^{-1} Mpc$ sphere around the target halo. The lower right plots always show only halos within r_{10} around the target halo, the other three panels show the three different projection of a box of $40 h^{-1} Mpc$ around the target halo.

$r_{tr} = 4h^{-1}Mpc$, approximately 8–10 times the typical virial radius of the target galaxies. This is a relatively large region, so it ensures that there is no contamination with low resolution (LR) particles, which is to be avoided, and it is still cheap to simulate at the first resolution level. A contamination with those LR particles is problematic for the re-simulations because the intruder represents an unphysical local potential minimum due to its higher mass and thus can cause the particles in the simulation to clump around it, introducing substructures where none should be. Therefore, to keep the high resolution area free of intruders is a very important step.

2.2.2. Track

Following the procedure of Tormen et al. (1997), we trace the previously selected particles by ID to their positions in the unperturbed initial conditions (ICs) of the parent simulation. There they occupy a Lagrangian volume V_{La} which is enclosed in a cube of size L_{HR}. We found $L_{HR} = 1/64\ L_{Box}$–$1/32\ L_{Box} \approx 15.6$ Mpc–31.2 Mpc and call this the high resolution (HR) box. We find the shape of V_{La} by mapping the tracked particles on a 16^3 3D-grid inside the HR box and marking cells which are occupied. In a few cases it was necessary to mark additional cells by hand to fill small holes and ensure that the selected region is compact. In our case V_{La} occupies a fraction of the HR box of 10–35 per cent, with larger values if the smaller HR box can be used. A typical slice through the center of this grid can be seen in the left panel of figure 2.4. The colored pixels mark the chosen V_{La}, with blue being the grid cells that contain tracked LR particles and red an additional buffer zone that also makes the region more compact.

2.2.3. Zoomed Initial Conditions (ZIC)

Once we have defined a HR Lagrangian volume where we want to increase the resolution, we can generate multi-mass initial conditions using the Zoomed Initial Conditions (ZIC) technique (Tormen et al., 1997). In the HR region V_{La}, marked as the red area in the right panel of figure 2.4, an increased number of particles with lower mass are at first put on a regular grid. It gets surrounded by a sphere of radius $\approx L_{HR}$ of particles that have the same mass as in the parent simulation, in order to reproduce the local force field. Outside of that, the number of particles representing the long range tidal forces can be minimized if they are binned on a spherical grid with constant angular resolution $d\theta = d\phi$, and $dr = rd\theta$ such that the cells are approximately cubic. Due to that method, the number of particles decreases and their masses increase with increasing distance from the HR region. The total number of these LR particles is $\approx 2 \times 10^6$ with $d\theta = 1.5\,°$. The right panel of figure 2.4 shows a projection of the initial conditions of the whole cosmological box generated with this method.

In the next step, we then perturb this distribution by using the power spectrum of the parent simulation. This means that the same density fluctuations appear as in the parent simulation, recreating the original cosmological structure. Since the HR
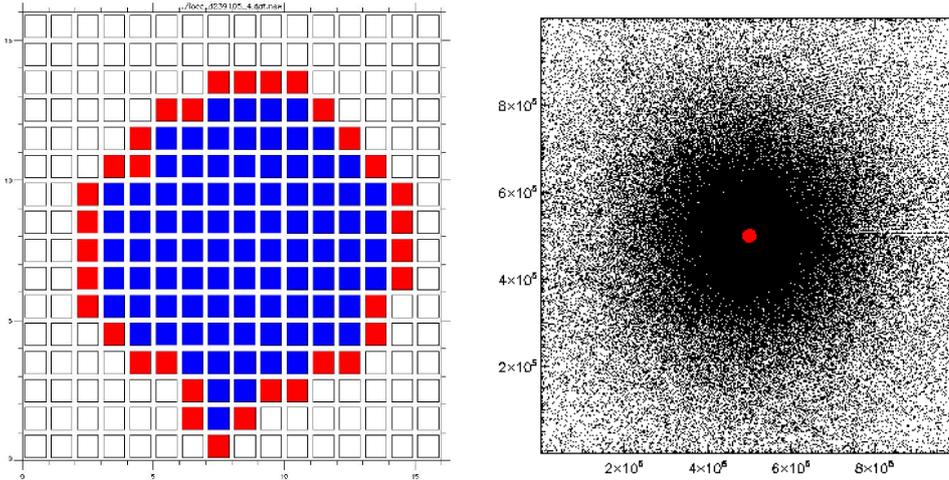
Figure 2.4.: *Left:* Occupation of the HR box. Blue squares: area occupied by HR particles. Red squares: additional safety area around the HR region. *Right:* Projection of the zoomed initial conditions of the whole $1h^{-1}Gpc$ cosmological box. The low resolution particles in black have a low density at the edges where only the information on the large scale tidal forces is needed, and have the highest density close to the HR region in the center for an improved resolution of the local force field. The red area in the center that marks the HR region is very small due to the typical size of the target objects.

region now also resolves smaller spacial scales, it has to be perturbed with additional smaller wavelengths that did not appear in the ICs before. The initial redshift of the simulation has to be increased in order to stay in the linear regime of cosmological evolution even for the smaller scales according to the Zeldovich approximation.

This method was used successfully for re-simulating clusters (see e.g. Bonafede et al. (2011)), but we found some numerical limitations for zooms on galaxies in large boxes, where large resolution jumps between parent and re-simulation can occur. Those limitations are discussed in the following.

Limitations by resolution of the parent simulation

One relevant limitation is that there is a minimum size L_{HR} of the HR box given by the size and the spacial resolution Δ_{Box} of the parent simulation. During the generation of the additional small scale perturbations in the HR region, the LR and the HR power spectra have to be matched. This is only possible if they have some overlap, i.e. $\lambda_{Box,min} < \lambda_{HR,max}$, that is the smallest wavelength in the parent simulation $\lambda_{Box,min}$, has to be smaller than the largest wavelength $\lambda_{HR,max}$ in the HR region. Tormen et al. (1997) therefore introduce the requirement

$$\frac{\lambda_{Box,min}}{L_{HR}} \geq 4 \tag{2.1}$$

in their code, and take $\lambda_{Box,min} = n_{safe}\,\lambda_{Box,Ny} = 2\,n_{safe}\,\Delta_{Box}$ with $\lambda_{Box,Ny}$ the wavelength according to the Nyquist frequency, and a safety factor $n_{safe} = 2$. For
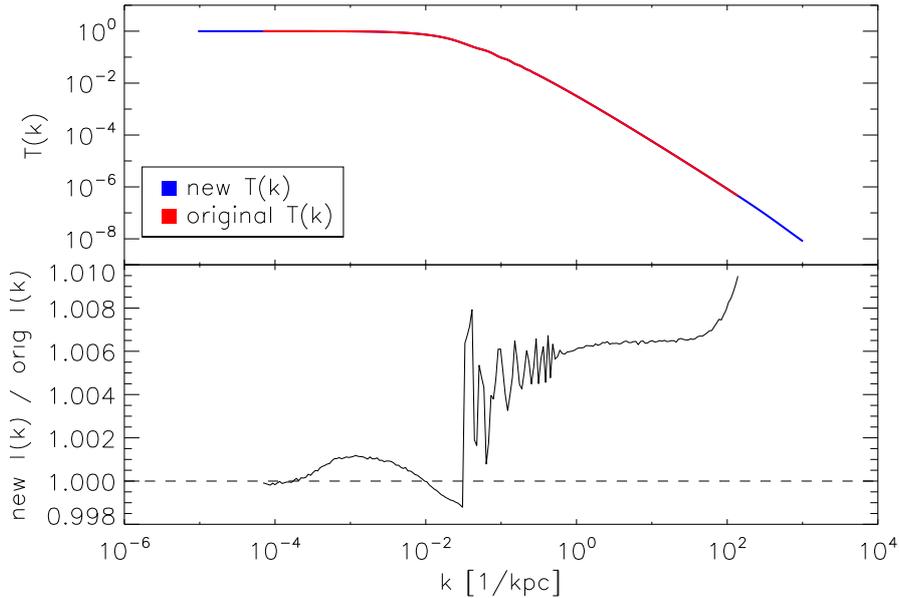
Figure 2.5.: The original transfer function (red line) was too short for the highest resolution run and was extended to larger k values (blue line). The deviation from the original is relatively constant for large k values.

our simulations, this results in

$$L_{HR} \geq 8n_{safe}\Delta_{Box} = \frac{L_{Box}}{64} = 15.6h^{-1}Mpc \qquad (2.2)$$

with $\Delta_{Box} = L_{Box}/1024$ in our case. This is a rather large lower limit for zooms on galaxies and can only be circumvented by increasing the resolution in the parent simulation.

Maximum HR resolution

The Fourier mesh used to calculate the perturbations in the HR region must be fine enough to reliably sample the particle distribution at the highest required resolution. This grid should stay fixed throughout all resolution steps to conserve the perturbations on larger scales exactly and only add small scale perturbations. The minimum mesh size is at the Nyquist frequency $n_{HR,Ny} = 2 \times L_{HR}/\Delta_{HR}$. A large fixed L_{HR} as in equation 2.2 and the small typical mean particle separations Δ_{HR} for galaxy simulations with high resolution can lead to $n_{HR} = n_{HR,Ny} > 1024$. The code implementation of ZIC requires an indexing of n_{HR}^3 3D grid points which has to be done with the 8-byte integer data type for $n_{HR} > 1024$, as the usual 4-bit integer data type can only represent smaller numbers. This leads to a doubling in the required random access memory (RAM) size to values > 30 GB just for indexing, which can pose technical limitations on some machines and increases computational cost significantly.

Power spectrum

For reasons of consistency the same power spectrum $P(k)$ used for the parent simulation is also used for the generation of the zoomed initial conditions. It must therefore extend to large enough wave numbers k to resolve perturbations on the smallest scales. This was not the case for our parent simulation, so we had to generate a new, extended transfer function using the code CAMB by Lewis et al. (2000), with cosmological parameters as close as possible to the original ones[1]. We could not reproduce the original transfer function exactly, but the new function is only used at the largest k values where the relative error is relatively constant around $\approx 0.6\%$, as shown in figure 2.5. Our new $T(k)$ is sampled at almost ten times more k values than the original. This helps to reduce errors in the interpolation of k values and the generation of perturbations. We compared the ICs generated with the new and the original power spectrum and did not find any significant differences.

Initial Redshift

With increasing resolution, the ICs have to be generated at increasingly large initial redshift z_{ini} to ensure that even the smallest resolved scales stay in the linear, non-chaotic regime of cosmological evolution that can be approximated analytically. Simulations only have to follow the chaotic, turbulent regime. The ZIC code uses a very conservative estimate of the initial redshift which can be as large as $z_{ini} = 180 - 300$ in our case due to the very high resolution that we reach. Using higher order perturbation theory of the cosmological evolution could help to mitigate numerical integration errors at these high redshifts, but was beyond the scope of this thesis.

2.3. Re-Simulations

The new ICs generated with the ZIC method described above were then evolved with the newest version of the same code used to run the parent simulation, the cosmological TreePM SPH code GADGET-3. This is done in two steps, first by a purely gravitational dark matter simulation to get contamination-free initial conditions, then with baryonic physics. These steps are described in detail in the next two subsections. We encountered some difficulties with the numerical precision and the choice of the gravitational softening length that are described at the end of this section.

2.3.1. Simulating with DM only

As the first step we use pure dark matter (DM) physics, i.e. no baryonic physics, to evolve the ICs to the final redshift $z = 0$. The targeted object is again identified by the halo-finder SUBFIND at all redshifts and we construct a merger tree. As

---

[1]Actually not the original ones because they were not available so we reconstructed the missing information from the power spectrum of the parent simulation.

explained in the previous section, it is important at this point to check if there are any intruding massive, low resolution particles in the vicinity of the target galaxy. We require at least $r_{clean} \geq 7 \times r_{vir}$ at $z = 0$ of cleaned region as a buffer zone in order to avoid contamination with LR particles. We also checked that there are no intruders within r_{vir} at all redshifts. Otherwise the HR-box size must be increased and the whole procedure of constructing the ICs must be repeated. However, this criterion was usually met easily with typically $r_{clean} \approx 8\text{--}12 \times r_{vir}$.

Once the simulation region is cleaned, we re-track the particles again to generate new ICs with a larger particle number, and repeat the procedure at a higher resolution. The advantage of taking consecutive resolution steps is that a clean Lagrangian region can be found with minimal computational cost by using a relatively small resolution to approximate the targeted region so that in the most expensive final step the region is found after just one or two tries.

2.3.2. Simulating with baryons

We include baryons by splitting all HR DM particles that end up inside $5 \times r_{vir}$ into gas and DM particles with a mass ratio according to the cosmic baryon fraction $f_b = 0.15$. The particles are displaced by the mean inter-particle distance while conserving mass and momentum. Figure 2.6 shows projections of the resulting distribution of HR particles. A large fraction of the DM particles is split, but there is still a buffer zone of unsplit DM particles left which hinder LR particles from entering the baryonic volume.

The code follows the baryonic physics with cooling and the standard star formation recipe by Hernquist and Springel (2003). For the highest resolution runs, level 4, we also include splitting of star forming gas particles into two particles of half the original mass. For the first runs with low resolution we use the standard cubic-spline kernel for SPH. For the high resolution levels 3 and 4 we use the Wendland C6 kernel with 295 neighbors and a time-dependent artificial viscosity scheme.

2.3.3. Summary of Re-Simulations

For this work we performed simulation runs of our four halos in the highest resolution possible, i.e. a particle mass resolution of $M_{DM}^{part} = 4 \times 10^6 h^{-1} M_{\odot}$ and $M_{Bar}^{part} = 6.2 \times 10^5 h^{-1} M_{\odot}$. These runs are used in chapter 3 for the scientific part of this work. Since those runs at this resolution are computationally very expensive, we needed to find the best possible numerical parameters to use, i.e. select a softening, test for convergence within the runs of different resolutions and solve precision issues. Those studies were performed using the halo Bat as a test case and in the remaining part of this chapter we present the results of these studies.

Table 2.2 lists the parameters for all simulation runs used in this work. R1 to R4 denotes the resolution of the re-simulation, R1 has particle masses of $M_{DM}^{part} = 1 \times 10^9 h^{-1} M_{\odot}$ and $M_{Bar}^{part} = 1.6 \times 10^8 h^{-1} M_{\odot}$, R2 has $M_{DM}^{part} = 8.4 \times 10^7 h^{-1} M_{\odot}$ and $M_{Bar}^{part} = 1.6 \times 10^7 h^{-1} M_{\odot}$, R3 has $M_{DM}^{part} = 4 \times 10^7 h^{-1} M_{\odot}$ and $M_{Bar}^{part} = 6.2 \times$
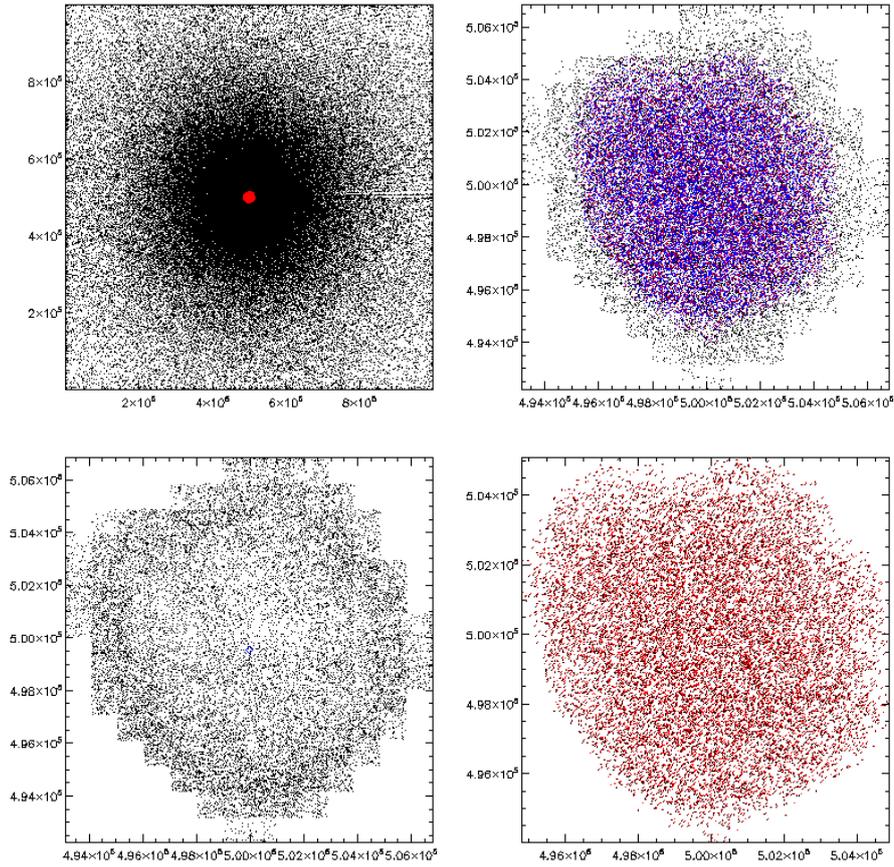
Figure 2.6.: Splitting Gas and DM particles. The upper right and the lower panels show the distribution of the HR particles. In color are the split DM and gas particles and in black are unsplit DM particles. The signature of the HR grid is visible. The red area in the upper left panel shows the size of the HR region in the box (same as the right panel of figure 2.4).

2. Simulations

$10^6 h^{-1} M_\odot$ and R4, as mentioned above, has $M_{DM}^{part} = 4 \times 10^6 h^{-1} M_\odot$ and $M_{Bar}^{part} = 6.2 \times 10^5 h^{-1} M_\odot$. As mentioned in subsection 2.3.2, runs use either the standard cubic-spline kernel, denoted as *standard* in table 2.2, or the more advanced Wendland C6 kernel and include time-dependent artificial viscosity, denoted *wendland+*. The more technical issues of precision and softening issues are discussed in the following subsection 2.3.4 in detail.

As described beforehand we also performed DM-only simulations of all runs at all resolutions to find the ICs and exclude intruder problems. Since we do not use these DM-only simulations for any further study in this work, they are not listed in table 2.2.

Object	Resolution	Version	Numerical precision	softening	time resolution
Bat	R1	standard	float	large	103
		wendland+	double	small	103
		wendland+	double	large	103
	R2	standard	float	large	103
		wendland+	double	small	103
		wendland+	double	large	103
	R3	standard	float	small	103
		standard	double	small	103
		standard	double	large	103
		wendland+	double	small	103
	R4	standard	float	small	103
		standard	double	small	103
Frog	R4	wendland+	double	small	103
		wendland+	double	small	925
Frogout	R4	wendland+	double	small	103
Pig	R4	wendland+	double	small	103

Table 2.2.: List of Re-Simulations used in this work.

Time resolution

All of our re-simulations are resolved with 103 snapshots spaced almost equally in physical time. This gives a decent time resolution for most of our analysis while keeping computational cost and space requirements at acceptable levels. However, the merger history of some of our objects is rather violent and we could not resolve certain events very well. For that reason we re-ran one of the simulations, Run 4 of frog, with a much higher time resolution of 925 snapshots. With that we were able to see much more details and events in an animation of the projected galaxy and other time dependent properties of the object. A comparison of the star formation rate histories between the normal and the high temporal resolution runs can be seen in figure 2.7. More and sharper peaks are resolved in the left panel, especially around

(a) High time resolution. **(b)** Normal time resolution.
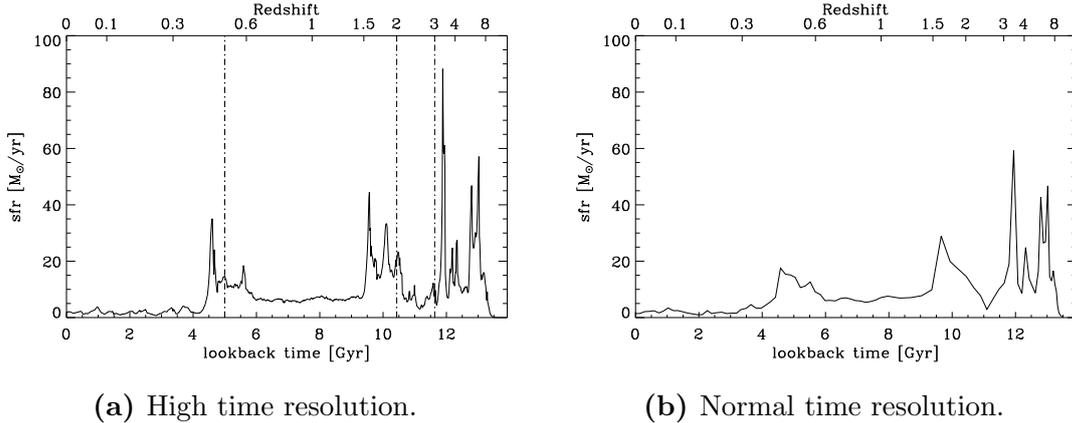
Figure 2.7.: Comparison between the star formation rates versus time for the high and normal time resolutions. Note the increased number and sharpness of the peaks in the left panel (high time resolution) around the merger events that are marked by the dash-dotted vertical lines.

the times of merger events marked by the dash-dotted lines. There are three clearly distinguishable peaks at the event around $z = 2$ in the high resolution run that are completely blurred out at normal resolution. This demonstrates the strength of a high time resolution, but it comes at the cost of a large storage requirement (≈ 1.3 TB) and much larger computational cost for the analysis.

2.3.4. Precision, softening and convergence tests

We encountered some numerical issues during the simulation process that will be described in the following. All the test were done with the object bat and the other objects confirm the results.

Numerical precision

Highly parallelized cosmological simulations are usually memory limited. The amount of required memory per particle can be drastically reduced if most quantities like positions are stored as 32-bit floating-point numbers ("float") instead of 64-bit numbers ("double"). The main difference is that a float number can only store $\approx 6 - 7$ significant digits, whereas a double stores ≈ 15.

The HR region is usually placed in the center of the parent simulation. In our case of $L_{Box} = 1h^{-1}Gpc$ and code units of $h^{-1}kpc$, the numerical position values are at $x \approx 500000$. Storing x as float means numerical round-off errors on the order of $\Delta x = 0.1 - 1kpc$. This is not problematic for simulations with relatively low resolutions such as typical full box simulations or our first zooming steps where the mean particle separations and gravitational softening are at least an order of magnitude larger than Δx. This can be seen in the upper panels of figure 2.8 where we show the density profiles of stars (red) and DM (black) in resolution R1 and R2,

with single precision runs as dashed and double precision runs as straight lines. The deviations in the density profile are small and well below the resolution limits of the runs.

But as soon as the resolution is large enough to resolve scales of order Δx, the round-off errors become dominant and lead to artificial cores in the stellar and DM density that affect scales even an order of magnitude larger than Δx. The lower panels in figure 2.8 show the density profiles dor the runs with resolutions R3 and R4, and demonstrate that this effect becomes more significant with resolution and effectively reduces the resolution of these runs to $> 20 kpc$.

We want to resolve scales of the order of kpc in a Gpc box and therefore use double precision for all of our final simulations.
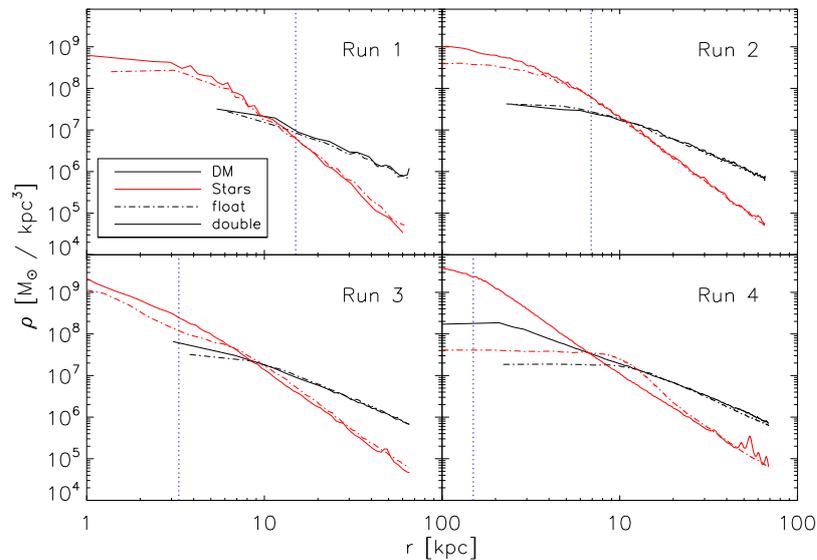
Figure 2.8.: Convergence test of numerical precision. Black and red lines show the density profiles of DM and stars, respectively, for the same halo at increasing resolution. Continuous lines are for simulations with double precision, dash-dotted lines are single precision. The vertical, dotted blue line marks the minimum resolved scale ($= 3 \times \epsilon_{grav}$). Note the large deviation from the expected power law profile in the highest resolution runs with float precision.

Gravitational softening and convergence tests

The gravitational force F_g between to objects at distance r scales as $F_g \propto 1/r^2$ and therefore diverges for very small r. Since a N-body code numerically treats particles as point masses, they can get arbitrarily close to each other. However, the resulting strong two-body encounters are unphysical as our simulation particles represent huge numbers of objects that do not collide. It is therefore necessary to soften the force between two particles on small scales so that the collision of computational particles

does not cause numerical artifacts. The scale on which the gravitational force is adapted is called the *softening length* ϵ and sets the effective spatial resolution of the simulation. It is therefore a compromise between resolution and limiting numerical noise that depends on the properties of the physical objects one wants to simulate. Dehnen (2001) finds that ϵ should be scaled with the particle density n as $\epsilon \propto n^{-1/3}$. In a cosmological simulation, n changes over time and space as the simulated objects grow. Adapting ϵ over time is possible. However, a spatially dependent ϵ changes the equation of motion in a way that they are no longer intrinsically energy-conserving. This property can be restored for systems where all particles have the same mass, such as typical DM-only simulations. However, simulations that follow dark matter as well as baryonic physics are usually set up with particles with different masses like our simulations as described in section 2.3.2. In this case the matter density and the particle number density are not longer the same and it is theoretically unclear which of the two quantities should be used for the scaling (Price and Monaghan, 2007; Iannuzzi and Athanassoula, 2013).

However, the usual approach in the literature is to avoid this issue and set a spatially fixed ϵ, dependent on the mass resolution m of the simulation as $\epsilon \propto m^{1/3}$. We define the proportionality constant ϵ_0 using

$$\epsilon = \epsilon_0 \left(\frac{m_{DM}}{10^9 h^{-1} \, M_\odot} \right)^{1/3} \tag{2.3}$$

where the mass of a simulated dark matter particle m_{DM} is scaled to the mass resolution of our parent simulation. There is a large range of proposed values for ϵ_0 in the literature. Some authors use the same softening length for DM and baryons while others scale it to the respective particle mass with $\epsilon \propto m^{1/3}$. There are also a variations on whether or when to change the temporal dependence from fixed in comoving coordinates to fixed in physical coordinates.

Since there is no agreement on the optimal solution yet, we tested two different settings. One is used in re-simulations of clusters in our parent simulation described by Bonafede et al. (2011). They use the same $\epsilon_0 = \epsilon_{DM} = \epsilon_{Baryons}$ for DM and baryonic particles and start with a relatively high value of $\epsilon_0 = 15 h^{-1} kpc$ fixed in comoving coordinates for $z > 2$, and $\epsilon_0 = 5 h^{-1} kpc$ fixed in physical coordinates afterwards. We refer to this as the "large" ϵ. The other is used by Oser et al. (2010), as well as in the simulations used for the theoretical modeling in the ATLAS[3D] project (Naab et al., 2013), and is relatively small. Here, $\epsilon_{DM} = 3.2 h^{-1} kpc$ and $\epsilon_{Baryons} = 1.7 h^{-1} kpc$ are scaled with the respective masses of DM and baryons, but are fixed in comoving coordinates at all times. We call this the "small" ϵ. As mentioned above, improves a smaller ϵ improves the effective resolution and is preferred as long as the risking of numerical heating is small.

We simulated our test object at increasing resolution levels (see table 2.2) for the small softening and found that the density profiles are well converged for DM and stars outside the resolution limit, as shown in the upper panels of figure 2.9. The gas profiles, however, change dramatically between runs and apparently switch between

two distinct configurations. The second highest resolution level, Run 3 (red lines), has a much denser atmosphere of hot gas than the lower Run 2 (blue lines) and the higher Run 4 (black lines) resolutions.
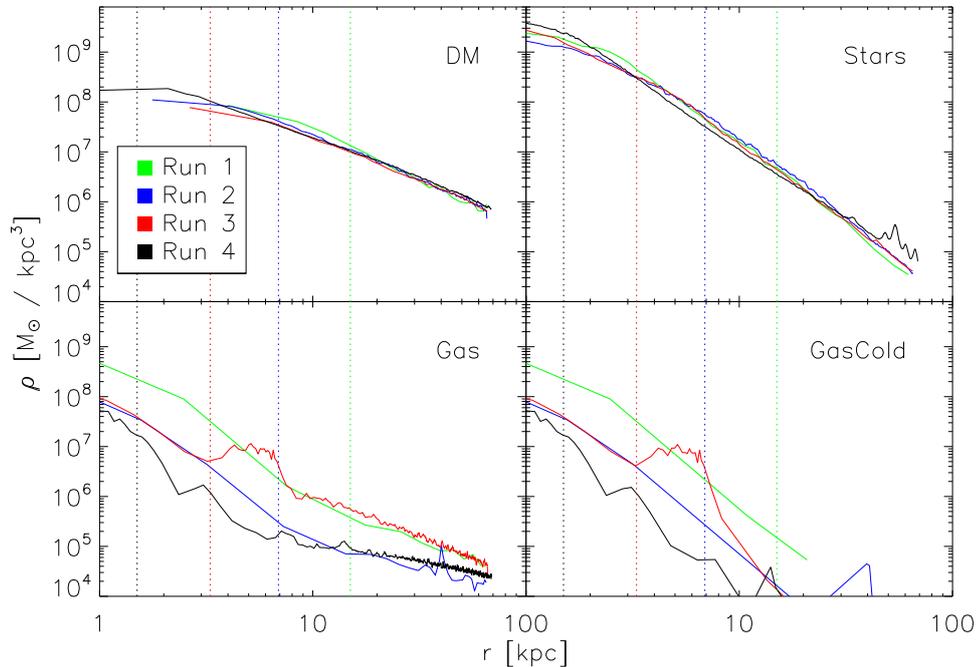

Figure 2.9.: Convergence test between resolutions. Density profiles for resolution R1 (green), resolution R2 (blue), resolution R3 (red) and resolution R4 (black lines). Dashed lines mark the minimum resolved scales ($= 3 \times \epsilon_{grav}$) for the different runs, colored respectively. *Upper left:* Profiles for DM particles. *Upper right:* Profiles for stellar particles. *Lower left:* Profiles for all gas particles. *Lower right:* Profiles for cold gas particles only.

The same dichotomy is visible when comparing both softening settings for the same mass resolution Run 3 in figure 2.10, where we plot the density profiles for runs with different softenings. The larger ϵ does not produce the dense hot atmosphere as seen for the smaller ϵ, but is in very good agreement with the higher resolution Run 4 with a small softening.

We also find a strong difference between large and small ϵ for Run 3 in the way gas is accreted. There are two different gas accretion modes for galaxies, depending on the virial mass M_{vir}, as described by Kereš et al. (2005). Galaxies with $M_{vir} \gtrsim 10^{12} M_{\odot}$ are usually able to shock-heat accreted gas to the virial temperature ($T_{vir} \sim 10^6$ K for a Milky Way type galaxy). This is called *hot mode* accretion, and could be expected for our halos. In the *cold mode* the gas that falls in along filaments is dense enough to efficiently cool the smaller shock-heating of the halos and never reaches T_{vir}. However, Kereš et al. (2005) also find cold mode accretion in some more massive galaxies.

We traced all gas particles that are inside $10\% r_{vir}$ at $z = 0$ back in time to
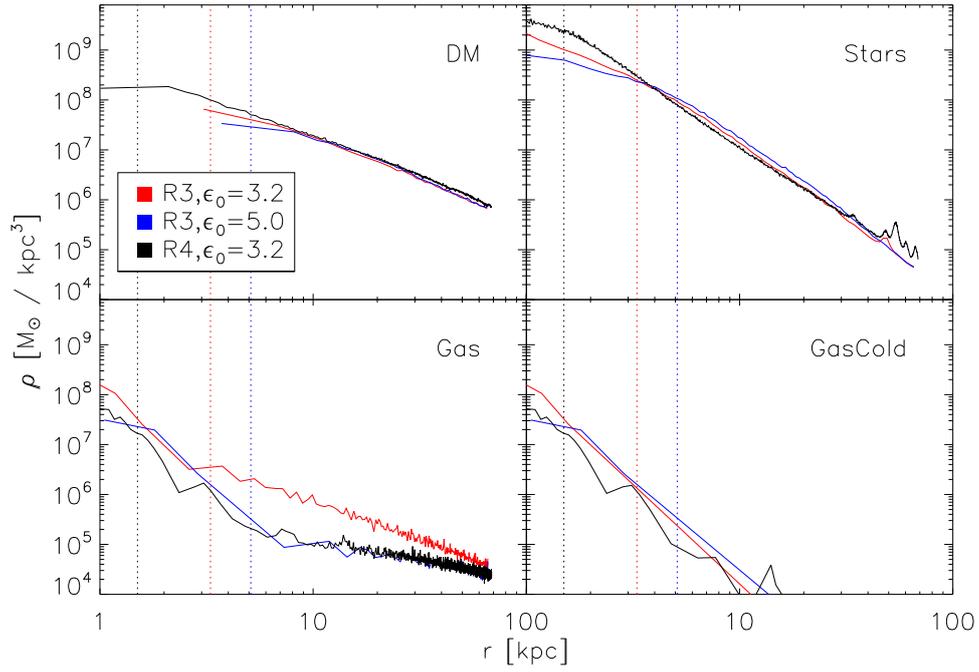
Figure 2.10.: Softening test. Density profiles for the small ϵ in resolution R3 (red), large ϵ in resolution R3 (blue) and small ϵ in resolution R4 (black lines). Dashed lines again mark the minimum resolved scales ($= 3 \times \epsilon_{grav}$) for the different runs, colored respectively. Panel distribution as in figure 2.9.
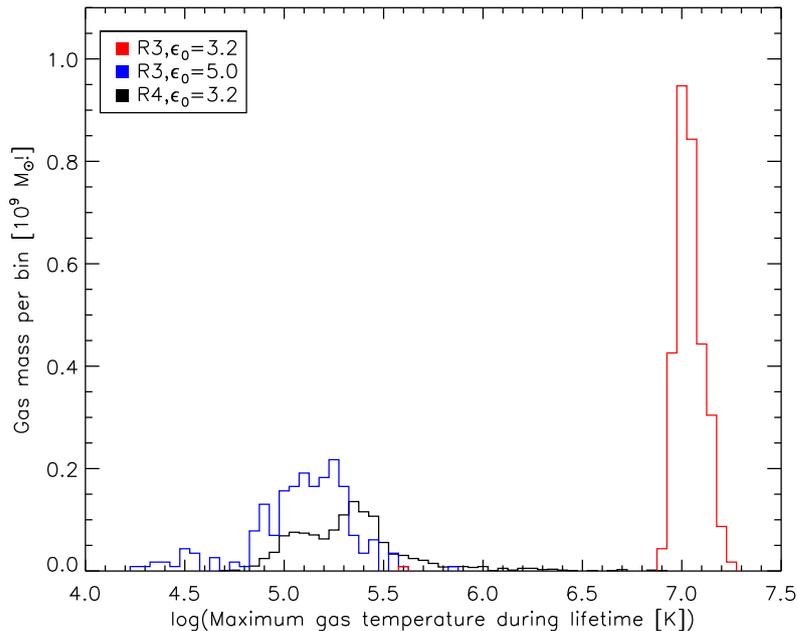
Figure 2.11.: Hot/Cold mode accretion

calculate their maximum temperatures T_{max}. Figure 2.11 shows the mass weighted distribution of T_{max} for the simulations with different ϵ. The red line clearly shows the hot mode accretion of the small softening in Run 3, while both the Run 3 with large softening and Run 4 with small softening show almost exclusively cold mode accretion.

When looking only at the lower resolution Run 3, there is a clear distinction between the gas properties when simulating with different ϵ and a comparison with observations seems to indicate that a smaller softening produces more realistic results. However, this is not stable against a higher mass resolution which is numerically more reliable. Run 4 is clearly much more in agreement with the larger softening setting in Run 3. This leaves only the explanation that the result from the small ϵ is not of physical, but of numerical origin. The softening was small enough to trigger significant numerical heating in the densest regions. This prevented efficient cooling of dense regions which are then more easily shock-heated at infall. Furthermore this effect decreases the star formation rate, leaving more gas in infalling structures that can contribute to the hot atmosphere and would otherwise have turned to stars. The missing stars are not visible in the stellar density because the difference in gas mass is several orders of magnitude smaller.

This shows that ϵ is an important parameter in SPH simulations that, if only slightly changed, can even change the macroscopic behavior. Agreement with some observational indicators is not necessarily the best way to fix numerical parameters in such complex simulations, as some results can also be produced by numerical artifacts that are not stable against mass resolution.

3. Results

In this chapter we describe the results of the analysis of the four objects we selected in section 2.1. We use only simulations at the highest mass resolution level, i.e. particle masses of $M_{DM}^{part} = 4 \times 10^6 h^{-1} M_\odot$ and $M_{Bar}^{part} = 6.2 \times 10^5 h^{-1} M_\odot$, with a softening length of $\epsilon_{DM} = 0.5 h^{-1} kpc$ and $\epsilon_{Bar} = 0.27 h^{-1} kpc$ and double precision, since those configurations give the best results as discussed in the previous chapter. In section 3.1 of this chapter we present the properties at $z = 0$ of our four galaxies, like masses and sizes, and profiles for densities and velocity dispersions. We also provide a comparison with state-of-the-art observations. In section 3.2 we analyse the formation histories of our galaxies, and in section 3.3 we finally study the cold gas content in the centers of our galaxies and its origin.

3.1. Properties at redshift z=0

We first study the properties of our objects at redshift $z = 0$ to check that they are comparable with observations of present day galaxies in a similar mass range. Table 3.1 lists some properties like the virial radius r_{vir}, the stellar half mass radius $r_{1/2}$ calculated inside $0.1 r_{vir}$, and the mass of different components inside these radii. The virial masses of our four halos range from $M_{vir} = 1.26 - 1.81 \times 10^{13} M_\odot$ with $r_{vir} = 608 - 686 kpc$ which is comparable to observations (see Kravtsov (2013)), as shown in Figure 3.1. This figure, taken from Kravtsov (2013) (figure 1 in that paper), provides a summary of different observed galaxies covering a large range of 8 magnitudes in masses by plotting the virial masses $M_{vir} \approx M_{200}$ with the stellar halfmass radii $r_{1/2}$. Our galaxies are overplotted as green stars, and they are in good agreement with the observations. It can clearly be seen that our galaxies are at the upper mass range, where no spiral galaxies are observed anymore, but they are well within the mass-size-relation seen for early-type galaxies.

In our simulation, we define gas to be cold if it has a temperature below $5 \times 10^5 K$ or is currently forming stars. All other gas is considered hot. The objects Bat and Frogout are the most massive ones in our sample and have almost identical size and mass properties. Even though all objects have otherwise proportionally very similar properties, the slightly lighter objects Frog and Pig have a significantly smaller amount of gas inside $r_{1/2}$. This could be a mass effect, as heavier objects can have deeper potential wells and bind more gas to their centers. Another possibility is that it might be an environmental effect as the first two were selected as the most isolated objects and the latter two are from a slightly more crowded cosmological environment.
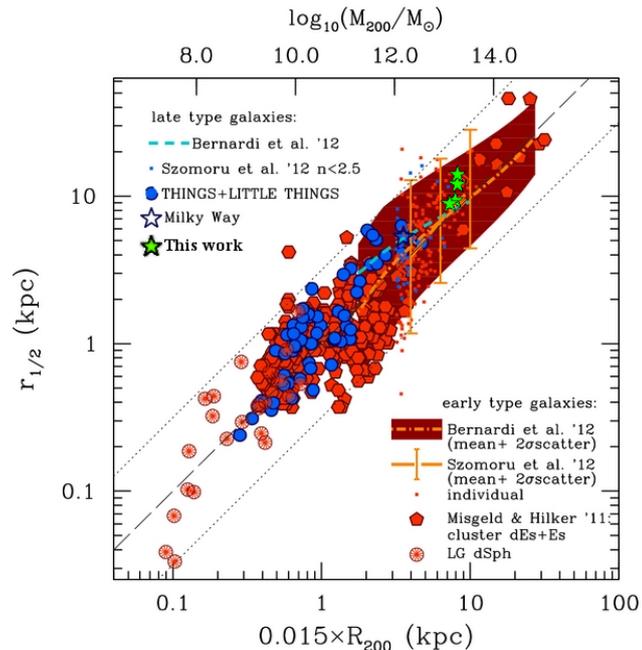
Figure 3.1.: Figure 1 taken from Kravtsov (2013), with our four galaxies overplotted as green stars. The figure shows the stellar halfmass radius of galaxies against the virial mass respectively the 0.015× the virial radius of the whole halo. The dashed line shows the linear relation $r_{1/2} = 0.015R_{200}$, the dotted lines are $0.5dex$ offsets to this relation.

A visualization of the galaxies can be found in figure 3.2, where we show the mass weighted stellar density inside $0.1r_{vir}$ along two principal axes of the stellar distribution. The pixel size used for binning is $0.5kpc$. All four objects have the expected elliptical shape of early type galaxies. While Bat and Frog both show oblate shapes, albeit much stronger for Frog than for Bat which is more roundish, Frogout is clearly triaxial, whereas Pig has a prolate shape. Their local environment is very homogeneous apart from some minor satellites, and Bat and Frog both have a distinguishable but small companion. All of the cold gas in this volume is overplotted as blue dots. Most of it is close to the galaxy centers, but there are also some accumulations of cold gas in the outskirts that are not associated with any visible stellar structure, best visible in Frog. They are close to the galaxy and far inside the halo, so it is likely that they were recently stripped by ram-pressure from infalling substructures visible at similar radii, and are not necessarily numerical artifacts as described by Kaufmann et al. (2009).

3.1.1. Density profiles

In order to study radially dependent properties of the galaxies we take radial bins of equal mass and average over the mass within these spherical shells. This allows a good sampling of the profiles with constant statistical significance. The components are separately binned with an equal particle number of 500. For the gaseous
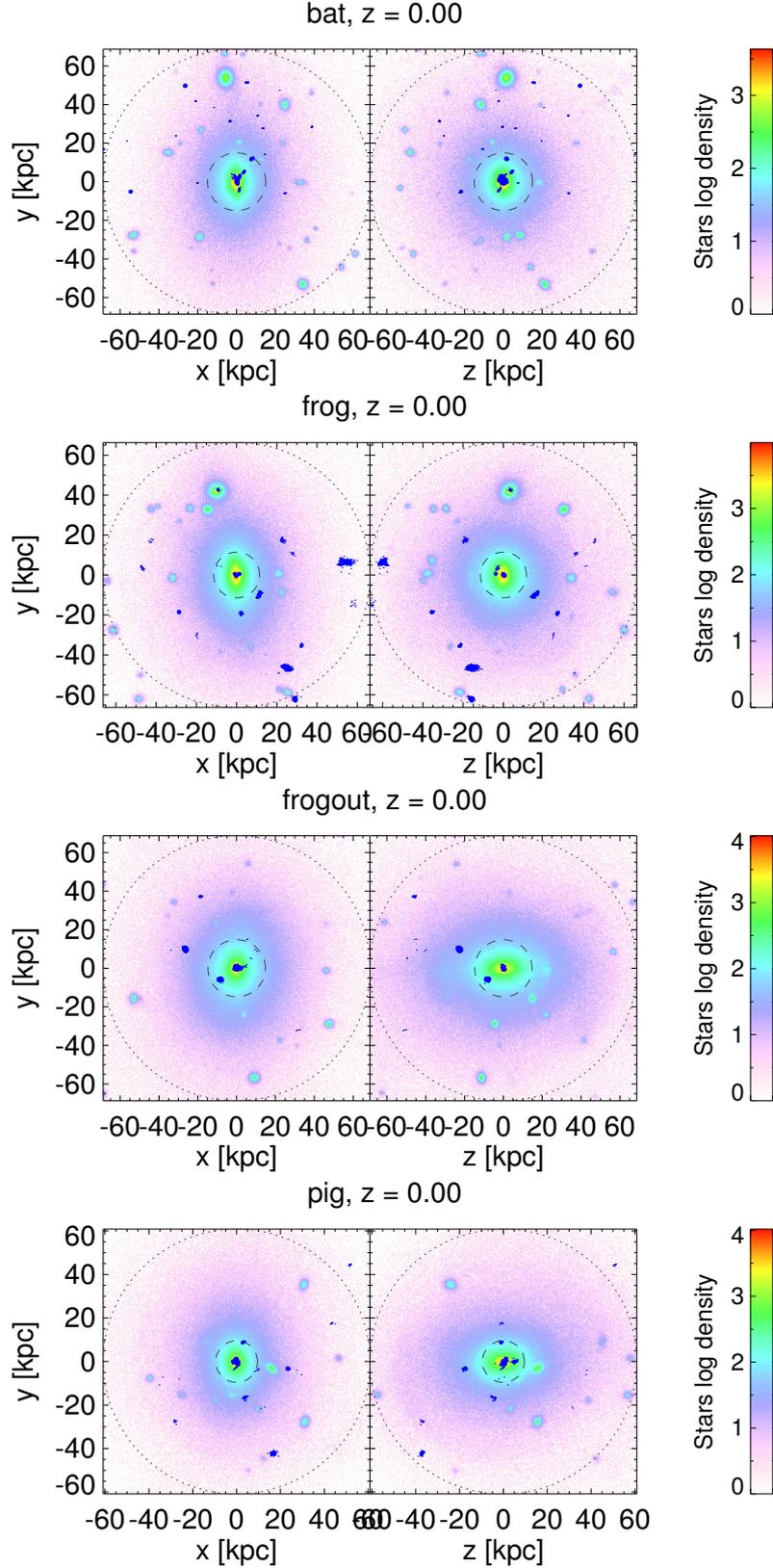
Figure 3.2.: Projections of the stellar mass weighted density along the principal axes. The dotted line marks $10\%r_{vir}$, the dashed line the stellar $r_{1/2}$. Overplotted in blue are the positions of cold and starforming gas particles.

3. Results

Table 3.1.: Properties of the four objects at redshift z=0.

Name	M_{vir}	r_{vir}	$r_{1/2}$	M_{DM} $(< r_{vir})$	M_{HotGas} $(< r_{vir})$	M_{Stars} $(< r_{1/2})$	M_{Gas} $(< r_{1/2})$	$M_{ColdGas}$ $(< r_{1/2})$
	$[10^{13} M_\odot]$	[kpc]	[kpc]	$[10^{13} M_\odot]$	$[10^{12} M_\odot]$	$[10^{11} M_\odot]$	$[10^{9} M_\odot]$	$[10^{9} M_\odot]$
Bat	1.28	686.5	15.0	1.81	1.30	3.50	2.51	1.21
Frog	1.07	663.2	11.4	1.63	1.23	2.92	1.12	0.43
Frogout	1.23	686.9	14.8	1.81	1.36	3.23	2.39	1.19
Pig	0.90	608.5	9.6	1.26	1.00	2.23	0.91	0.58

components we take a smaller number of 50 particles in order to extend the profile to small radii.
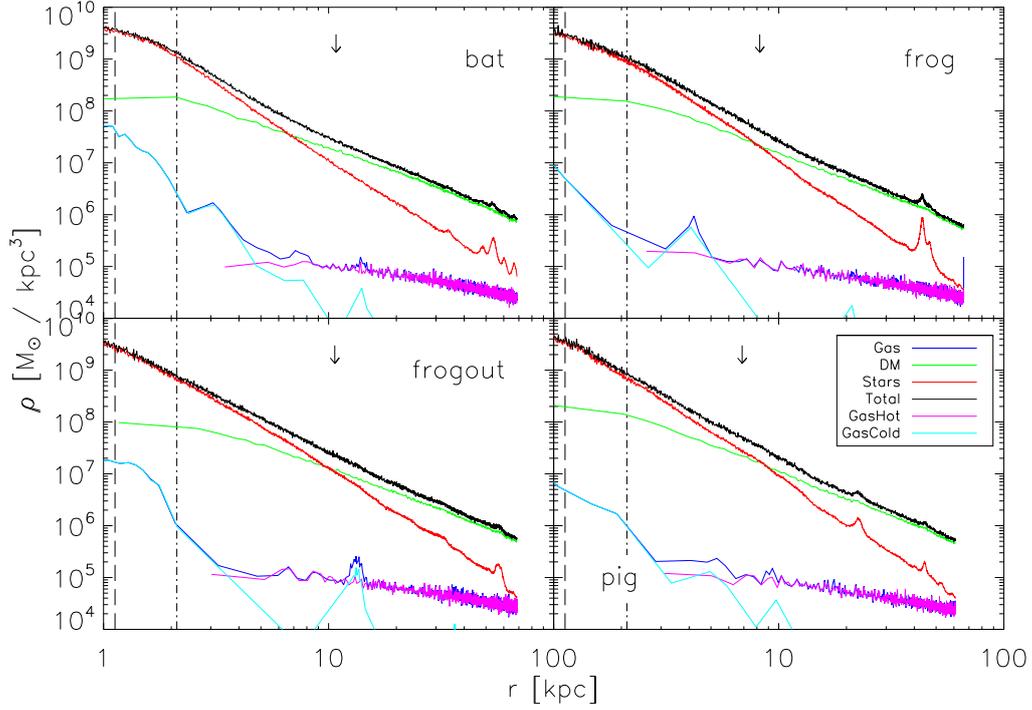
The density profiles of our objects are shown in figure 3.3. All four have total density slopes that are fit well by a power law with slopes γ for $\rho \propto r^\gamma$ down to the resolution limit in the stellar and DM component. The slope of the total profile is for all halos around $\gamma = -2$, in agreement with the results presented in Remus et al. (2013), as shown in figure 3.4.

This figure shows the slope of the total density γ_{tot} against the halfmass radius for the simulation sample from Remus et al. (2013), that consists of re-simulated spheroidals from a cosmological simulation (filled dark grey circles) and spheroidals from isolated binary mergers (light grey filled circles). Our galaxies are shown as green filled stars in that figure. This figure also includes observations of COMA cluster ellipticals (Thomas et al. (2007), blue open circles) and strong lensing ellipticals (Auger et al. (2010); Barnabè et al. (2011); Sonnenfeld et al. (2012), black, dark blue and light blue open circles respectively). Our galaxies also agree well with the observed values for the density slopes.

In our total density profiles, we see a slight increase of the density below $r \lesssim 10kpc$, where the stellar component starts to dominate the total density profile. This might be due to missing AGN feedback in the center which was not included in our simulations. In the cases of Bat and Frog, the stellar density shows peaks at the positions of the small companions mentioned already previously.

The gas distribution of all galaxies is dominated by cold gas inside the central $r \lesssim 3 - 4kpc$, with a very step incline in its density towards the center. Outside of this radius there is hardly any cold gas, but all galaxies have a halo of hot gas with $\rho \approx 10^5 M_\odot/kpc^3$ and flat slopes extending to large radii.

Observers often assume that the X-ray halo seen in clusters traces the DM profile. This requires that both of them follow the same potential and therefore have a similar slope in their densities. But in our halos, the density slopes of the hot halos are significantly flatter then the DM slopes. This could mean that the galaxies in our simulations have not developed a significant hot halo as it is observed in clusters of galaxies, which would agree with the observations of isolated elliptical galaxies which normally have a hot but not yet X-ray bright gas halo.

Figure 3.3.: Density profiles of the four objects at $z = 0$ for the different components. The stellar components are shown as red lines, the DM components as green lines, and the combined profiles of stellar and DM component are shown as black lines. The gas component (dark blue) was split into hot (magenta) and cold (light blue) gas. There were too few (< 50) hot gas particles at small radii for further binning. The vertical lines mark the resolution limits at $3 \times \epsilon_{grav}$ from the different gravitational softenings of DM (dash-dotted) and stars/gas (dashed). The vertical arrows mark the stellar $r_{1/2}$. The profiles are cut of at $0.1 \, r_{vir}$.
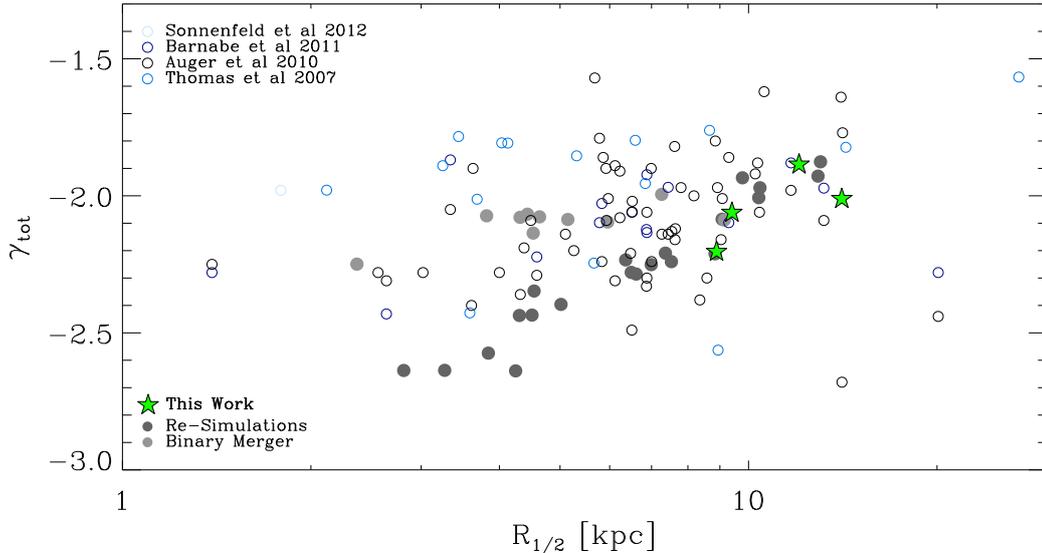
Figure 3.4.: Total density slopes against halfmass radii. Green stars show the results of the four speroidals from this work. Open circles show the observations as indicated in the legend, filled circles show the results from simulations from Remus et al. (2013), also indicated in the legend.
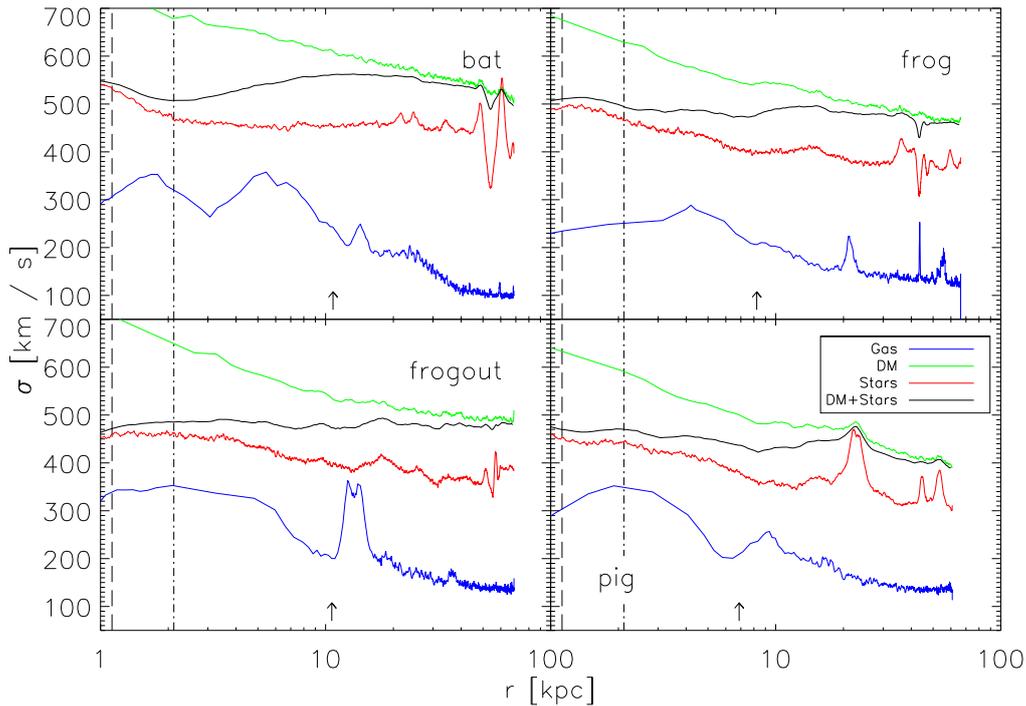
3.1.2. Velocity dispersion profiles

We also studied the radial velocity dispersion profiles of our four objects. The radial binning was done in the dame equal mass bins used for the density profiles, and for all but the total velocity dispersion σ_{tot} of DM and stellar component combined, the σ in each bin was calculated as

$$\sigma = \sqrt{\sigma_x^2 + \sigma_y^2 + \sigma_z^2} \tag{3.1}$$

with $\sigma_x = \sqrt{\langle v_x^2 \rangle - \langle v_x \rangle^2}$ and σ_y and σ_z respectively. To calculate the total velocity dispersion, σ_{tot}, that represents the whole potential of the halo, we need to mass-weight the intrinsic velocity dispersions for both components, DM and stars, within each shell, because DM and star particles have different masses. We calculate σ_{tot} as

$$\sigma_{tot} = \sqrt{\frac{M_{DM} \times \sigma_{DM}^2 + m_* \times \sigma_*^2}{m_{DM} + m_*}} \tag{3.2}$$

The results are shown in figure 3.5 for all our galaxies. In all cases, the stellar (red line) and DM (green line) intrinsic velocity dispersion profiles show a decrease with increasing radius, while the total intrinsic velocity dispersion profiles (black lines) are nearly flat, indicating that the halos are isotropic. This is again in agreement with the results presented in Remus et al. (2013)

Figure 3.5.: Velocity dispersion profiles of the four objects at $z = 0$. The black line is the σ calculated from the combination of DM and star particles, red lines show the stellar profiles, green lines the DM profiles and blue lines the total gas profiles. The vertical lines mark the resolution limits as in figure 3.3. The arrows mark the $r_{1/2}$. The profiles are cut of at $0.1\,r_{vir}$.

The values for the stellar velocity dispersions within $r_{1/2}$ are between $400 - 500km/s$, which agrees with observed velocity dispersions for very massive present day ellipticals, for example for M87 ($\sigma(1 - 10kpc) \approx 350 - 450km/s$, from Murphy et al. (2014)) and the sample of ellipticals presented in Gebhardt et al. (2000) where the most massive ellipticals have velocity dispersions around $\sigma \approx 350 - 400km/s$ within $R_{1/2}$.

As already seen in the density, the substructures show strong peaks in the stellar velocity dispersions of the ellipticals Bat and Frog, as well as in Pig where a very small substructure causes a very strong peak in the stellar velocity dispersion. While some peaks in the stellar velocity dispersion can therefore be clearly identified to be cause by substructures, some smaller peaks have no visible counterparts. Those structures, prominent especially in the stellar velocity dispersion profile of Frog around $10kpc$, could be either due to shell structures caused by recent mergers, or be a sigma-bump (see Schauer et al. (2014)). To distinguish between those two possibilities would require a detailed analysis of the evolution of the stellar velocity dispersion profile with time, which is beyond the scope of this work, albeit an interesting question.

The velocity dispersion profiles of the gas show a similar behaviour as the DM profiles at large radii where the hot component is dominating the gas. In the inner parts, where the cold gas gets dominant, we see a general but weak trend towards higher dispersions, but this could be due to the low number of particles in this region, introducing large errors into the calculation of the gas velocity dispersion at those radii. One special feature can be seen in Frogout (lower left panel of figure 3.5): between $10-20kpc$ there is a strong peak, also visible in the density of the cold gas component of Frogout in the lower left panel of figure 3.3. This feature is caused by a clump of cold gas, which can also be seen in figure 3.2 and which could either be a stripped gas component from a substructure that merged with the galaxy, or a Kaufmann blob. We will look into the properties of the cold gas in section 3.3 of this work in more detail.

3.2. Evolution

We have seen that the properties if our galaxies at $z = 0$ fit well with properties of present day massive elliptical galaxies from observations. In this section, we now want to understand the formation of our object over comic times. Therefore, we follow each of our objects over the different output times, using a merger tree. We used a standard algorithm to construct a tree that connects each halo identified by SUBFIND at a given output with its most massive progenitor at the previous time (see section 2.1). This tree also contains informations on the virial mass M_{vir} and the virial radius r_{vir} of the halo at each redshift, and we always use $10\%r_{vir}$ to estimate the size of the galaxy.

In the first subsection we analyse the mass histories of our halos and their according star formation rates to understand the formation mechanisms for the individual objects. In the second subsection we study the circularities in order to understand the gas and star properties that led to our present day ellipticals.

3.2.1. Mass accretion and star formation history

Galaxies with similar properties at $z = 0$ can have very different formation histories. One important aspect in the formation and evolution of a galaxy is how it accumulated its mass. As discussed in the introduction 1.2.1,there can be phases when the mass grows very rapidly through merging with another galaxy of similar mass in a so called "major merger", or it can grow more slowly and smoothly through accumulation of multiple smaller satellites or clumpy structure in "minor merger" events. If the object is very isolated or has already accreted all of its massive companions it enters a starved state with dominantly secular evolution.

This can be studied via the mass accretion history (MAH) and the evolution of the star formation rate (SFR) with time. We calculated both by following the most massive progenitor of a galaxy along the merger tree. For the MAH we sum over all masses inside r_{vir} to trace the whole halo, to identify the galaxy at the halos center
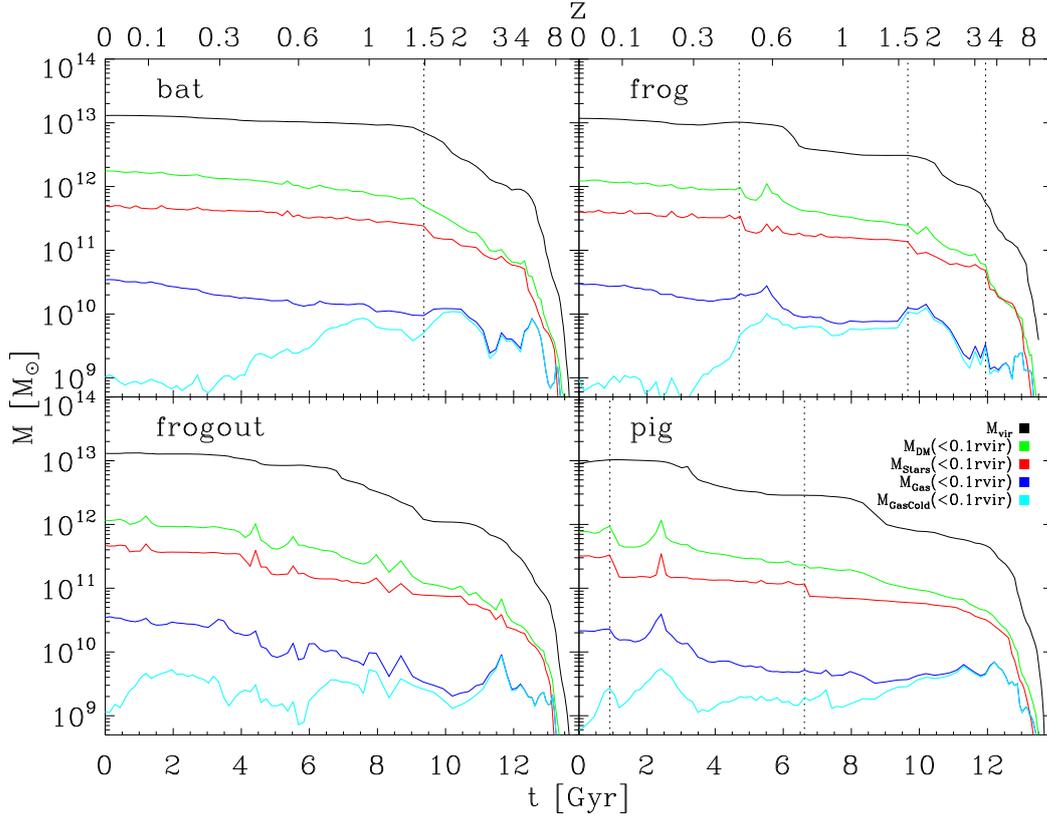
Figure 3.6.: Mass accretion history of the four objects Bat, Frog, Frogout, and Pig (left to right and top to bottom). Plotted is the total mass M_{vir} of the galaxy (black), and the mass of different components inside $0.1\,r_{vir}$: DM, stars, total gas, and cold gas (green, red, dark blue, light blue). The dotted vertical lines indicate mergers as described in the text.

we additionally follow the different components inside $0.1\,r_{vir}$ as shown in figure 3.6 for all our objects. The SFR is calculated by summing over the internal SFR of all multi-phase gas particles inside $0.1\,r_{vir}$. Its evolution is shown in figure 3.7.

We identify a merger by a sudden increase of the stellar mass inside $0.1\,r_{vir}$ (red lines in figure 3.6) and correlate this with the visual impressions from a time series of ray-traced projections, as shown in the Appendix. The latter is important to find real mergers and avoid misidentification. Galaxies, especially of similar mass, usually do not merge immediately if their relative velocities are too high, but often have multiple encounters after which they emerge again as individual objects before the final merging. Sometimes the relative velocity is higher than the gravitational escape velocity even at close encounters. In this case a fly-by occurs and the galaxies do not merge at all, even though the more massive object might gravitationally strip some weakly bound parts of the other system. It is generally somewhat delicate to pin down an exact time for the merging of two collisionless systems, and we prefer
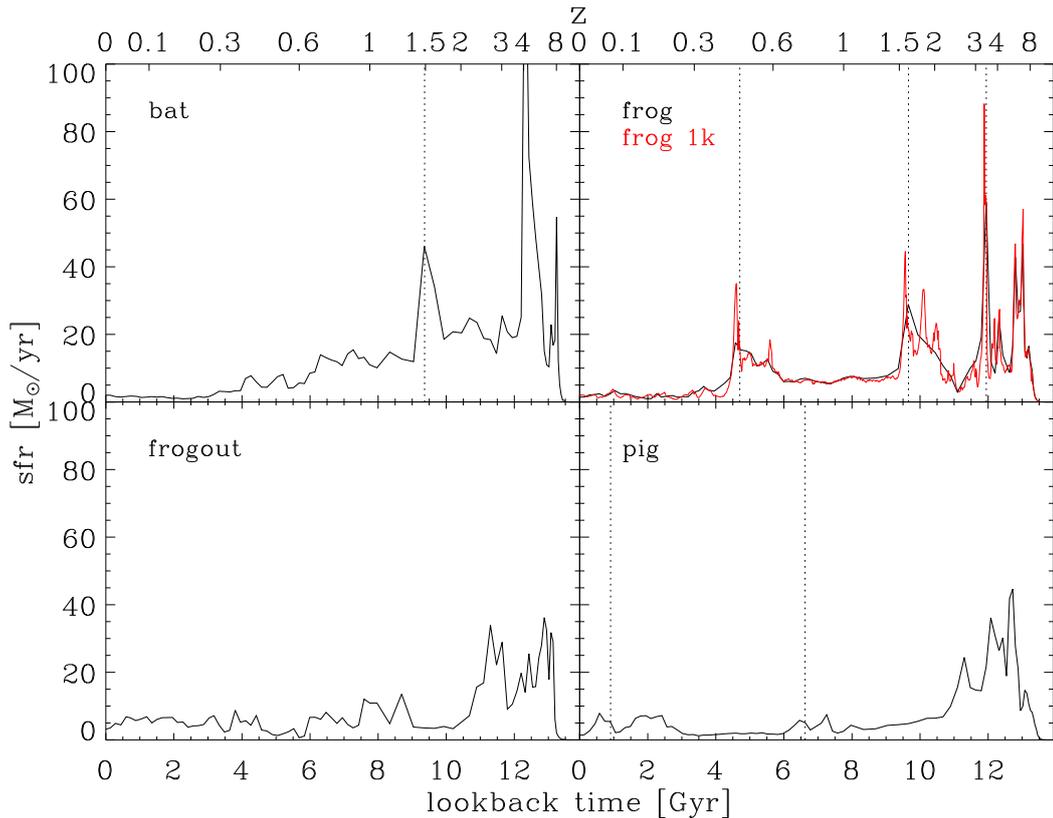
Figure 3.7.: Star formation rates versus time, calculated from the sub-grid SFR of gas particles inside $0.1\,r_{vir}$. The dotted vertical lines mark the same merger events as in figure 3.6. In the upper right panel the high time resolution run of Frog is overlaid as red line.

a method that is focused to the most central part of a galaxy. Another possible definition for the time of a merger could be at the time of the unification of the dark matter halos of two systems. However, this is not so strongly correlated to the fate of the stellar component as a dark halo is much more extended and the galaxies first have to cross the remaining distance.

Bat

The upper left panel of figure 3.6 shows the mass evolution of Bat. It accumulated most of its final mass quite early and had the last significant merger at $z \approx 1.5$. There is only little and relatively smooth increase in mass afterwards. This indicates a very isolated evolution, similar to a fossil group. This mass history is also in agreement with the results from van de Sande et al. (2013) who observed compact massive ellipticals at high redshifts. In order to explain the size growth of these compact objects that is needed to reach the properties of todays ellipticals, they propose that these galaxies could only have relatively smooth accretion. Any further violent
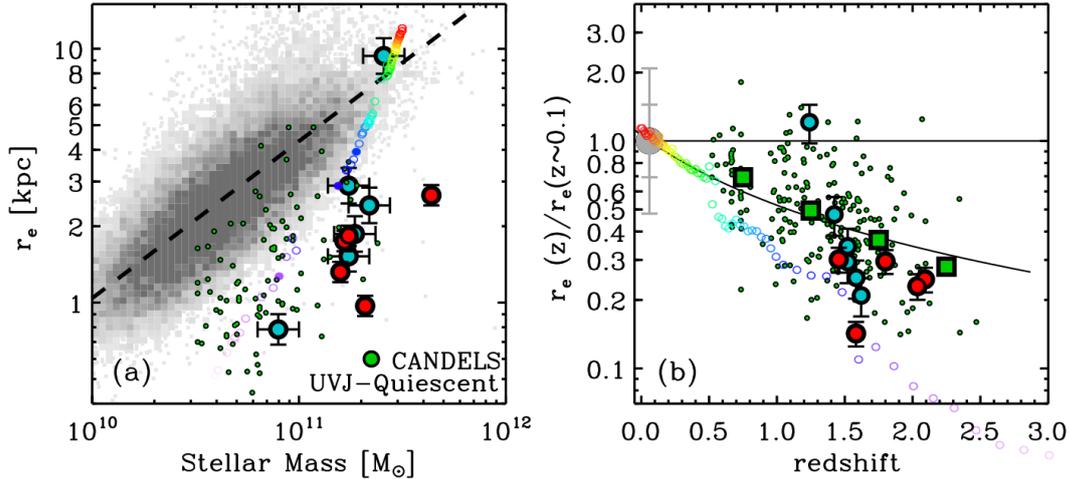
Figure 3.8.: Figure 8 taken from van de Sande et al. (2013). *Left:* Effective radius of the galaxies versus their stellar mass, for spheroidals at $z = 0$ from the SDSS as grey squares and for the spheroidals at higher redshifts as colorful filled symbols. Overplotted in rainbow colors, marking the different redshifts from $z \approx 1$ in blue to $z = 0$ in red, is the evolution of mass and size for our galaxy Bat. *Right:* $r_e(z)/r_e(z = 0.1)$ against redshift for the same objects as in the left panel. The solid line is the best-fit $r_e \propto (1 + z)^{-1.02}$ to the observational data shown in green.

events like a major mergers would increase the masses too much without an adequate increase in size. The authors fit a likely evolution of the effective radius r_e to their observations. The stellar half mass radius $r_{1/2}$, roughly equivalent to the observed r_e, of our simulated galaxy Bat is consistent with their observations, as shown in the right panel of figure 3.8, and even lands almost exactly on the relation after $z \approx 0.5$, probably due to a minor merger event. This indicates that our cosmological simulation produced a realistic result and a good example for the proposed evolution scenario of van de Sande et al. (2013) for quiescent massive ellipticals.

The mass accretion histories in also show the total gas mass (dark blue lines) and the cold gas mass (light blue lines) inside $0.1 \, r_{vir}$. Bat shows a smooth increase of total gas mass by a factor of ~ 3 after a relatively high redshift of $z \approx 2$ that is similar to the M_{DM}, but slightly steeper than the increase in $M_{\star}$ and M_{vir}. This behavior is relatively similar in all four objects, indicating that there is a steady infall of gas from the environment that could contribute to the formation of a hot halo.

The fraction of cold gas mass at $z = 0$ is low in all our galaxies, but the histories are different and connected to the star formation rates. Bat has a relatively large amount of cold gas in the initial phase of its formation before $z \approx 2$ that has strong variations correlated with peaks in the SFR (see upper left panel in figure 3.7). Mergers are difficult to distinguish from a strong accumulation of gas at the highest redshifts, but the high SFR also suggests a large fraction of in-situ starformation in this early phase. Even though there is a massive merger at $z = 1.5$ followed by

the expected starburst, this event is not able to deplete much of the cold gas in a short time. The SFR and the cold gas mass stay relatively high and only decrease gradually over roughly 5 Gyrs until both quantities level out at $z \approx 0.3$ to their present day values of $M_{cold} = 1.2 \times 10^9 M_\odot$ and $sfr = 2 M_\odot/\text{yr}$. This is further evidence for a mainly secular evolution of this isolated galaxy.

Frog

Looking at the mass accretion history of Frog, we see a completely different formation history. After the initial formation phase, there is a wet early merger at $z \approx 1.6$ that brings the masses $M_{vir} = 3 \times 10^{12} M_\odot$, $M_\star = 10^{11} M_\odot$, and $M_{\text{Gas}} = 10^9 M_\odot$, to values remarkably close to those of today's Milky Way where they stay for 4.5 Gyrs. Then a major merger with another galaxy of almost equal mass (mass ratio $1.3 : 1$) occurs at $z \approx 0.46$, which increases the masses to their present day value. We calculated the mass ratio by summing the stellar masses inside $r_{1/2}$ of both galaxies at $z = 0.7$ when they are still clearly distinguishable shortly before they merge.

This already suggests that the galaxy had a fate similar to that projected for the Milky Way and its neighbor spiral galaxy M31 of a rapid transition from spiral to elliptical structure via a major merger. As discussed in the introduction this is a well studied formation process for elliptical galaxies. Figure 3.9 shows the distribution of young stars shortly before their host galaxies merge. These stars are younger than 2 Gyrs and should therefore be the brightest. Their clearly visible structure supports this picture of merging spirals, as does the time series in Appendix B.

The evolution of the gas mass is also consistent with this. The gas in Frog is predominantly cold for most of the time. Its mass drops slightly after the first wet merger, due to the triggered burst of starformation that is also visible in the upper right panel of figure 3.7. However, most of the cold gas is retained until $z = 0.5$ and turned to stars at a roughly constant rate of $\sim 10 M_\odot/\text{yr}$. The final major merger then triggers another starburst and removes a large fraction of the cold gas reservoir by conversion to stars and heating.

There are small peaks in the time-line of $M_\star$ around $z \approx 0.6$ shortly before the merger. These are due to the typical behavior of multiple encounters before the final merging as described above. The high time resolution run of Frog also reveals this in the SFR history as $1-2$ peaks shortly before the mergers (red line in figure 3.7).

Frogout

Frogout (lower left panels in figures 3.6 and 3.7) indicates yet another possibility to form an elliptical. It reaches its final mass at a relatively low redshift of $z \approx 0.4$ after a long and relatively smooth growth with less sudden increases in M_{vir} than we saw in the major merger case before. There are several, but less dramatic jumps in $M_\star$ distributed over the whole history. This suggests that this elliptical could have formed via the multiple (minor) merger scenario.

The evolution of the cold gas mass is also different than in the previous two cases.

Figure 3.9.: A ray-traced image of the distribution of stars younger than 2 Gyrs at $z = 0.6$. Color-coded is the age of the stars from older (red) to younger (blue). The large central object is Frog shortly before its major merger with the lower object. The width is 96.8 kpc. Note the central bar and the spiral-like features.

It is relatively low around $5 \times 10^9 M_\odot$ but varies significantly. This is often related to the stellar mass history, such as close to the marked merger events when cold gas gets removed, usually also related to a slight increase in starformation activity. Still, the fraction of hot gas is lower and the cold gas reservoir gets refilled much more effectively after these events than was the case after the major merger in Frog. This is in agreement with an assembly of Frogout through multiple minor mergers.

Pig

The formation history of Pig (lower right panels in figures 3.6 and 3.7)) is similar to the major merger scenario in Frog (upper right panels), but shifted to later times. There is no early wet merger, and the galaxy mass stays relatively small until a major merger at $z = 0.76$ that brings it to $M_\star = 10^{11} M_\odot$. The final mass increase that brought the object above our mass selection criterion happens only around 1 Gyr before present day in a late major merger.

The consequence of this late mass assembly is that the gas mass stays relatively low most of the time. This is also reflected in the SFR that stays well below $10 M_\odot/\mathrm{yr}$ after the initial phase of starformation in the first 3 Gyrs. None of the major mergers can boost the SFR to similarly high values as the one seen for Frog. This indicates that the mergers are gas poor, and the late merger even removes most of the cold gas that was left. As discussed in the introduction, these late dry mergers are expected to leave shell structures that are observable today, and Pig also shows clear indications for shells after this merger at $z = 0.07$, as can be seen at the end

of Appendix D.

3.2.2. Circularity evolution

We quantify the shape evolution between disk and spheroidal for our four objects, that was indicate in the previous section, with the distribution of the *circularity parameter* ϵ. This parameter ϵ measures the ratio between the z-component of the specific angular momentum $j_z = (\mathbf{r} \times \mathbf{v})|_z$ of a particle and the specific angular momentum that this particle would have if it was on a circular orbit at the same radius r:

$$\epsilon = \frac{j_z}{j_c(r)} = \frac{(\mathbf{r} \times \mathbf{v})|_z}{r \times v_c(r)} \tag{3.3}$$

where $v_c(r) = \sqrt{G\,M(<r)/r}$ is the circular velocity (e.g. Scannapieco et al. (2012)). Spherical systems have dominantly unordered orbits and thus an ϵ-distribution around 0, whereas particles in a disk have mainly circular orbits and $\epsilon \sim 1$. We calculate ϵ for the stellar and gas component inside $0.1\,r_{vir}$ (see figure 3.10) and define the z-axis in the principal axis system of the stellar component inside the central $0.05\,r_{vir}$ to avoid a strong influence of substructures on the orientation. The direction of the z-axis is chosen such that the peak of the ϵ-distribution has a positive value, i.e. most stars have a positive j_z and are co-rotating. We then keep the same orientation also for the gas component. Thus, if the gas is counter-rotating with respect to the stars, ϵ becomes negative. We normalize the ϵ-distributions to have an integral of unity, equivalent to a normalization by mass. This results in histograms that are comparable over the large changes in mass with time.

Bat

Figure 3.10a shows the evolution of the ϵ-distribution of the stars in the four objects. The ϵ-distribution in Bat (upper left panel) is always around 0, indicating that it is dominantly spheroidal at all times. There are minor contributions from a disk component at $z = 3.6$, but the rapid mass accumulation and mergers until $z = 1.5$ seem to perturb the system strongly and make it spherical. This is in agreement with the mass accretion history and the consistency with observations described in the previous section that suggested that the galaxy is a compact massive elliptical already at high redshifts.

The negative ϵ values of the gas in Bat (figure 3.10b) seem to indicate that the gas is slightly counter-rotating since high redshifts of $z \approx 3.6$. This could be due to an early infall of a large amount of gas with a different angular momentum that survived for a long time. The peak ϵ values get closer to 0 over time while a fraction of the gas is turned to stars and the rest gets heated up to form a hot halo that is expected to have a spherical distribution. The negative ϵ values could also be an issue encountered with the rotation algorithm for this object: if the central stars have a very spherical distribution,they do not define the main principal axis very well and thus the main axis could have simply been chosen in the wrong direction. To identify
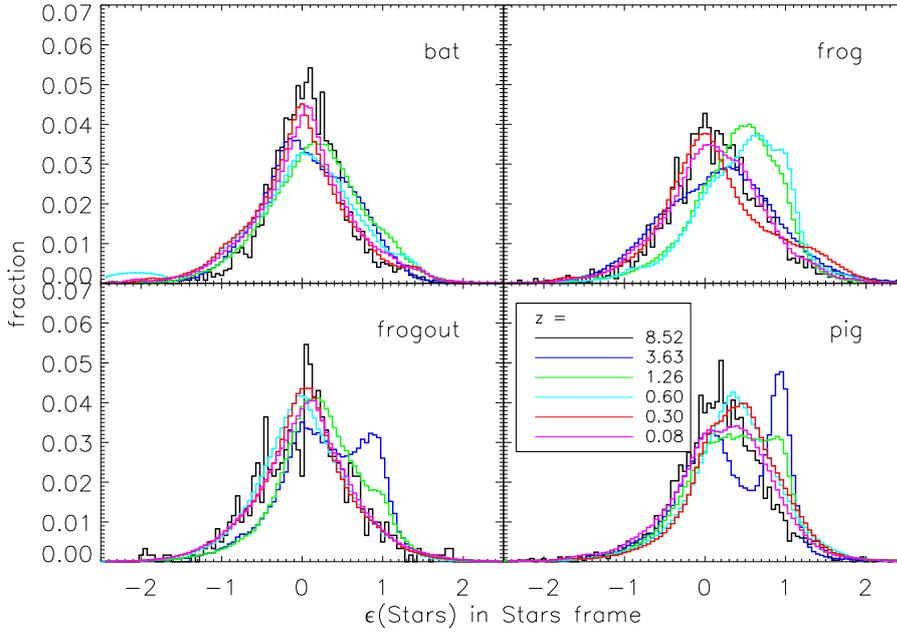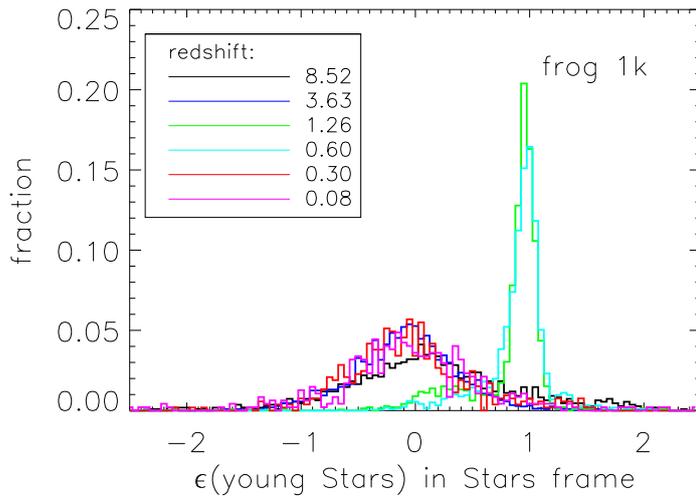
(a) Circularity evolution of the stars.
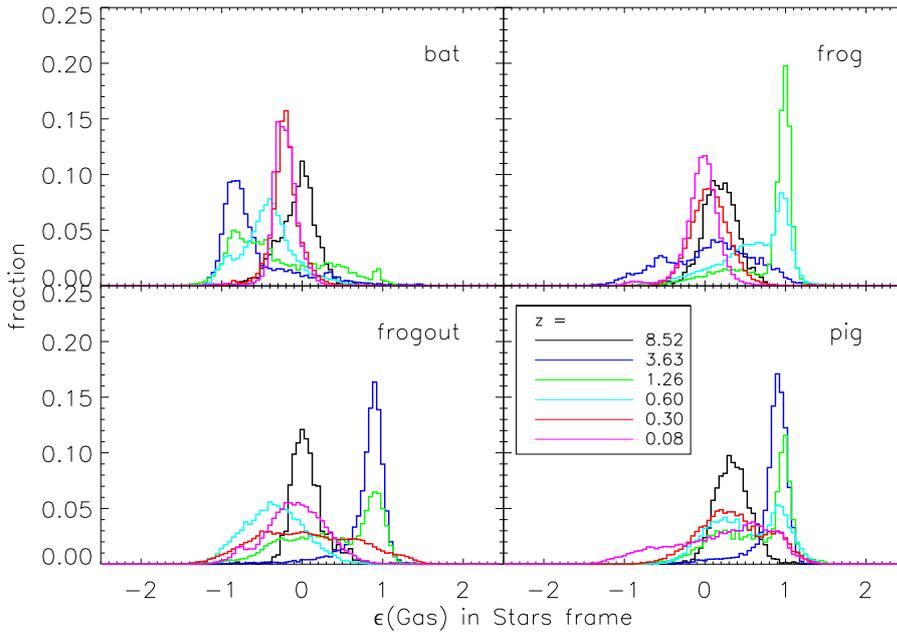
(b) Circularity of the gas component in the stellar coordinate system.

Figure 3.10.: Evolution of the circularity parameter ϵ for the stellar component inside $0.1\,r_{vir}$. At each redshift the object is rotated to the principal coordinate system of the stars within the central $5\%\,r_{vir}$. The distributions are normalized such that the integral is unity, equivalent to a normalization by total mass. Peaks around 1 and -1 indicate co- and counter-rotating disks, respectively, while $\epsilon \sim 0$ for spherical distributions. Different colors indicate different redshifts, as shown in the legend.

Figure 3.11.: Evolution of the circularity for Frog as in the upper right panel of figure 3.10a, but only for stars that formed less than 10^8 yrs before the given redshift. Stellar ages where only available for the high time resolution run for this object.

the origin of this counter-rotating gas would require further testing regarding the angular momentum evolution and rotation maps that is beyond the scope of this thesis.

Frog

The stellar circularities of the other three objects in figure 3.10a show clear deviations from a dominantly spherical distribution at some redshifts. Frog (upper right panel) starts like all other systems as a small spherical clump at $z = 8.5$ (black lines), as expected from the initial collapse of cosmological structures. It then shows a partial peak at $\epsilon = 1$, indicating contributions from a disk at $z = 1.26 - 0.6$ (green and light blue lines, respectively). At the same time there is an additional rotationally supported component around $\epsilon \approx 0.5$ that could be produced by a stellar bar feature. The gas component in figure 3.10b shows a clear disk feature with a strong peak at $\epsilon = 1$ at these times, indicating that in-situ starformation in a disk could contribute to the shift in the stellar circularity. If we select only newly formed stars younger than 10^8 yrs, we find indeed a clear peak at $\epsilon = 1$, as shown in figure 3.11. This supports the visual impression of a starforming spiral structure from figure 3.9. Stellar ages where only available for the high time resolution version for this object, but this should not affect the result.

The major merger at $z = 0.5$ then destroys the disk component, quenches starformation, and produces a hot spherical halo with all ϵ distributed around 0. The evidence for a disk structure until $z = 0.6$ and a spherically dominated shape afterwards is in good agreement with the results from the MAH. Both indicate that Frog

was a spiral galaxy that turned into an elliptical through a major merger.

Frogout

Frogout (lower left panels of figure 3.10a) initially has a pronounced stellar disk in addition to a spheroidal component at a high redshift of $z = 3.6$ (dark blue line). After that the peak at $\epsilon = 1$ gets much smaller ($z = 1.3$, green) and the spheroid is dominant after $z = 0.6$ (light blue). The gas circularity shows a similar behavior. In addition to the initial gas disk there is soon, at $z = 1.3$, a significant component with $\epsilon \sim 0$ that indicates the formation of a hot halo through feedback or dynamical heating. According to the MAH there is an encounter with another galaxy at $z \approx 0.6$ which can explain that the ϵ-distribution is already a single broad peak, indicating a spheroidal halo. The shift to negative values is likely due to the unrelaxed stellar system after the merger. At $z = 0.3$ (red) the ϵ values of the gas are even broader distributed over the whole range from -1 to 1 due to significant infall of gas through another merger. Eventually the system relaxes and the gas forms a hot halo with $\epsilon \approx 0$ at $z = 0$. In connection with the MAH, this evolution of ϵ can be interpreted as due to the formation of an elliptical galaxy via continuing dynamical heating of the system through the multiple mergers.

Pig

The ϵ evolution of Pig (lower right panels of figure 3.10a) also reflects the results from the MAH. The relatively unperturbed evolution until $z = 0.7$ allows continuing in-situ starformation in the gas disk. This results in a significant amount of stars with $\epsilon \sim 1$ until $z = 1.3$ (green). The major merger at $z = 0.7$ is already relatively dry due to the internal depletion of the gas reservoir. It perturbs the remaining circular orbits responsible for the $\epsilon = 1$ peak, but does not cancel all of the angular momentum as the ϵ distribution is still shifted towards 0.5 at $z = 0.6 - 0.08$, as can be seen from the light blue, red, and magenta lines, respectively. After the merger, the gas disk that was visible at $z = 3.6 - 1.3$, is reduced and shifted to a more spherical distribution with a dominant fraction at $\epsilon \approx 0$. However, the dry merger cannot completely deplete the gas disk and there is still a small peak around $\epsilon = 1$ at $z = 0.6 - 0.3$ (light blue, red). This small disk is also visible in the time series in Appendix D. This indicates that this galaxy could be similar to observations of dominantly spheroidal galaxies with a gas disk like the *Sombrero* galaxy NGC 4594. The final late merger in Pig occurs at $z \approx 0.07$ and creates a broad distribution of ϵ at $z = 0.08$ (magenta) in the gas due to the infall.

3.3. The origin of the cold gas

The main motivation of this thesis was to study the origin of the cold gas in the centers of early type galaxies (ETG) that was recently discovered by observations of the ATLAS$^{\text{3D}}$ project. In this section we analyse the cold gas content of our four

Table 3.2.: Properties of the four objects at redshift z=0.

| Name	M_{vir}	$r_{1/2}$	$M_\star$ $(< r_{1/2})$	$M(\mathrm{cold})$ $(< r_{1/2})$	$M(\mathrm{cold})/M_\star$ $(< r_{1/2})$
	$[10^{13} M_\odot]$	[kpc]	$[10^{11} M_\odot]$	$[10^9 M_\odot]$	$[10^{-3}]$
Bat	1.81	15.0	3.50	1.21	3.46
Frog	1.63	11.4	2.92	0.43	1.47
Frogout	1.81	14.8	3.23	1.19	3.68
Pig	1.26	9.6	2.23	0.58	2.60

Table containing the gas properties of the four Galaxies studied in this work.

ETGs at $z = 0$ and trace the origin of this gas particles in order to answer this question.

3.3.1. Cold gas at z=0

We define gas to be cold in our simulations if it has a temperature below $5 \times 10^5 K$ or has a subgrid star formation rate > 0, i.e. it is dense and cold enough to currently form stars. We found cold gas in the centers of all four of our high resolution massive ellipticals. The amount varies between $0.43 \times 10^9 M_\odot$ to $1.21 \times 10^9 M_\odot$, as listed in table 3.2. This corresponds to $M(\mathrm{cold\ gas})/M_\star = 1.47 \times 10^{-3}$ to 3.68×10^{-3} inside $r_{1/2}$, in agreement with data from the ATLAS[3D] observations who find molecular/stellar mass ratios $M(H_2)/M_\star = 3.4 \times 10^{-4}$ to 0.076 and, similarly for atomic gas in the centers of the galaxies, $M(\mathrm{HI})/M_\star = 10^{-4}$ to 10^{-1} (Young et al., 2013). We cannot distinguish between molecular and atomic cold gas in our simulations, but the kinematic analysis by Davis et al. (2011) of the ATLAS[3D] sample shows clear evidence that both types share a common origin, so this is of little importance for our study.

Our cold gas mass is at the upper end of the range of detected cold gas in ATLAS[3D], but our galaxies also have slightly higher stellar masses $M_\star$, as shown in figure 3.12. Young et al. (2011) found that the most cold gas rich ETGs are in a low density environment where gas accretion should be more effective. Our objects where selected to be the most massive galaxies in a low density region, so a relatively high gas mass is expected from the observations. Figure 3.12 also shows the results from Wei et al. (2010) who used the Nearby Field Galaxy Survey (NFGS; Jansen et al. (2000)) to study the atomic gas masses of field galaxies in our mass range. Their massive red-sequence ellipticals lie in the same region as our galaxies which suggests that the cold gas content in our objects is reasonable. The difference between the two surveys is that the bulk of the ATLAS[3D] galaxies has significantly lower cold gas masses, likely due to better resolution limits and less bias in the selection criteria towards higher cold gas masses. Their results have similar trends for massive field galaxies which is the relevant region in our case. Note also that following the gas and stellar physics in greater detail in the simulations tends to de-
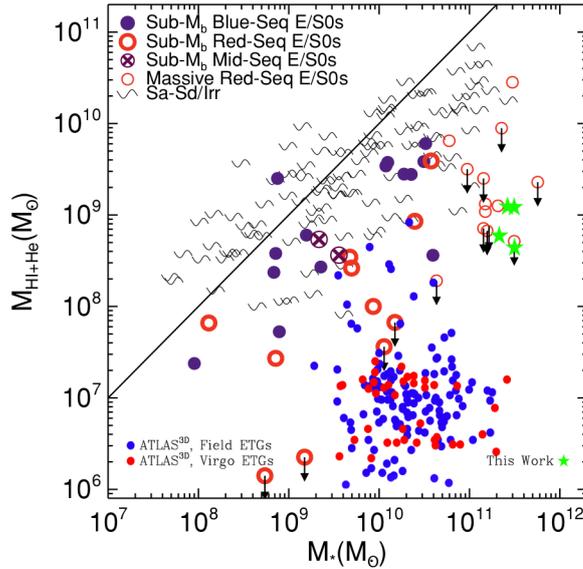
Figure 3.12.: Figure 5 of Wei et al. (2010) shows the distribution of atomic gas mass for different kinds of galaxies from the NFGS sample versus stellar mass. The solid line marks the 1 : 1 ratio, downward arrows are upper limits. We overlaid the data from the ATLAS[3D] galaxies (Young et al., 2013; Cappellari et al., 2013, 2011a) as filled small blue and red circles for Field ETGs and Virgo ETGs, respectively. The galaxies from this work are marked as green stars.

crease the stellar mass and including AGN feedback might reduce the cold gas mass slightly, and could thus move our galaxies closer to the bulk of ATLAS[3D] galaxies.

In the introduction 1.3 we discussed two different possible origins of the cold gas: internal processes like cooling from the dense central part of the halo and stellar mass loss, and external accretion via mergers or (cold) streams. They can be distinguished observationally by the resulting kinematic structure of the gas. Gas that cools via the internal processes should be aligned with the major axis of the stars, while accreted material usually does not have a prefered orientation of its angular momentum.

We analyze the distribution and morphology of the cold gas in our galaxies at $z = 0$ using the projections shown in figure 3.13. All cold gas particles inside the stellar halfmass radius $r_{1/2}$ are plotted over the stellar distribution inside this radius. All objects are rotated to the principal coordinate systems of the stars. The cold gas is mainly located in a clumpy structure at the center of each galaxy. This is expected as it can cool efficiently through radiation and thus loose energy and migrate towards the center of the potential. All of our objects also have at least one additional cold gas clump inside $r_{1/2}$, which indicates recent infall into the center of the galaxy as the clump did not have time to reach the center. In the case of Frogout this off-centered clump has similar extension and mass as the central clump, whereas Bat and Pig have several smaller cold gas clumps close to the center that

currently get tidally disrupted. Bat is the only case where the central clump has a disk-like structure that is relatively aligned with the principal axes of the stellar distribution. The three other objects have misaligned central cold gas.

Davis et al. (2011) study the kinematic alignment of cold gas in the ATLAS³D sample and find that a significant fraction of the local early-type galaxies show evidence for misaligned gas, indicating an external source. This is especially the case for field ETGs where at least 42% have misaligned gas. This means that the misalignments we see in our isolated galaxies is also expected from the observations and indicates that an external origin is more likely than cooling from the halo.

3.3.2. The origin of the cold gas in isolated elliptical galaxies

As there are indications that the origin of the cold gas might be external accretion, we study the evolution of the gas in the cosmological environment in order to understand how a galaxy gets fuelled with gas. We use Frog as an example and show four stages of its gas history between $z = 2$ and $z = 0$ in figure 3.14. The full time series begins at $z = 7.5$ and can be found in Appendix E. At $z = 2$ (upper left panel) the galaxy is heavily accreting cold gas via filaments that reach to its central part (blue particles). A relatively small hot gas halo is visible (yellow and green particles) that formed through heating and supernova feedback from the first starformation. The hot halo is already more massive at $z = 1$ (upper right panel) and thus able to heat most of the filaments that break up into fragments but a significant fraction of cold gas can still reach the center of the galaxy without being shocked. Parts of the hot halo of the infalling galaxy that will have the major merger with Frog can be seen in the upper right corner. The merger at $z = 0.5$ causes a starburst and a shock that heats a large fraction of the gas and produced a large hot halo. Parts of the halo can be seen to extend well outside the virial radius at $z = 0.27$ (lower left panel). The halo is now hot enough to shock-heat most of the infalling cold filaments. The relatively small gas-rich objects that fall in from the lower right get partially stripped but the densest and coolest parts of the gas are still able to penetrate to the center of the galaxy, but nevertheless refill the cold gas reservoir only slightly and do not trigger significantly enhanced starformation (see section 3.2.1). Even at $z = 0$ (lower right panel) there is a supply of cold gas in nearby filaments that are still accreted. Even though the halo is expected to shock-heat most of this gas close to the virial radius, some dense structures might reach the stellar component and provide the misaligned cold gas that is observed in field ellipticals.

We now focus on gas that is cold or starforming and located in the center of the galaxy inside the stellar $r_{1/2}$ at $z = 0$. In order to get a more quantitative understanding of its origin, we trace all of theses particles, that were also marked in figure 3.13 as blue dots, back in time and calculate for each of them the redshift z_{in} at which they fall into the virial radius of the galaxy. This is done by finding the redshift when a particle is inside r_{vir} for the first time and then take z_{in} from the previous simulation snapshot, when it is just outside, so that the particle crosses r_{vir} in between the snapshots. A small fraction of the gas particles where already
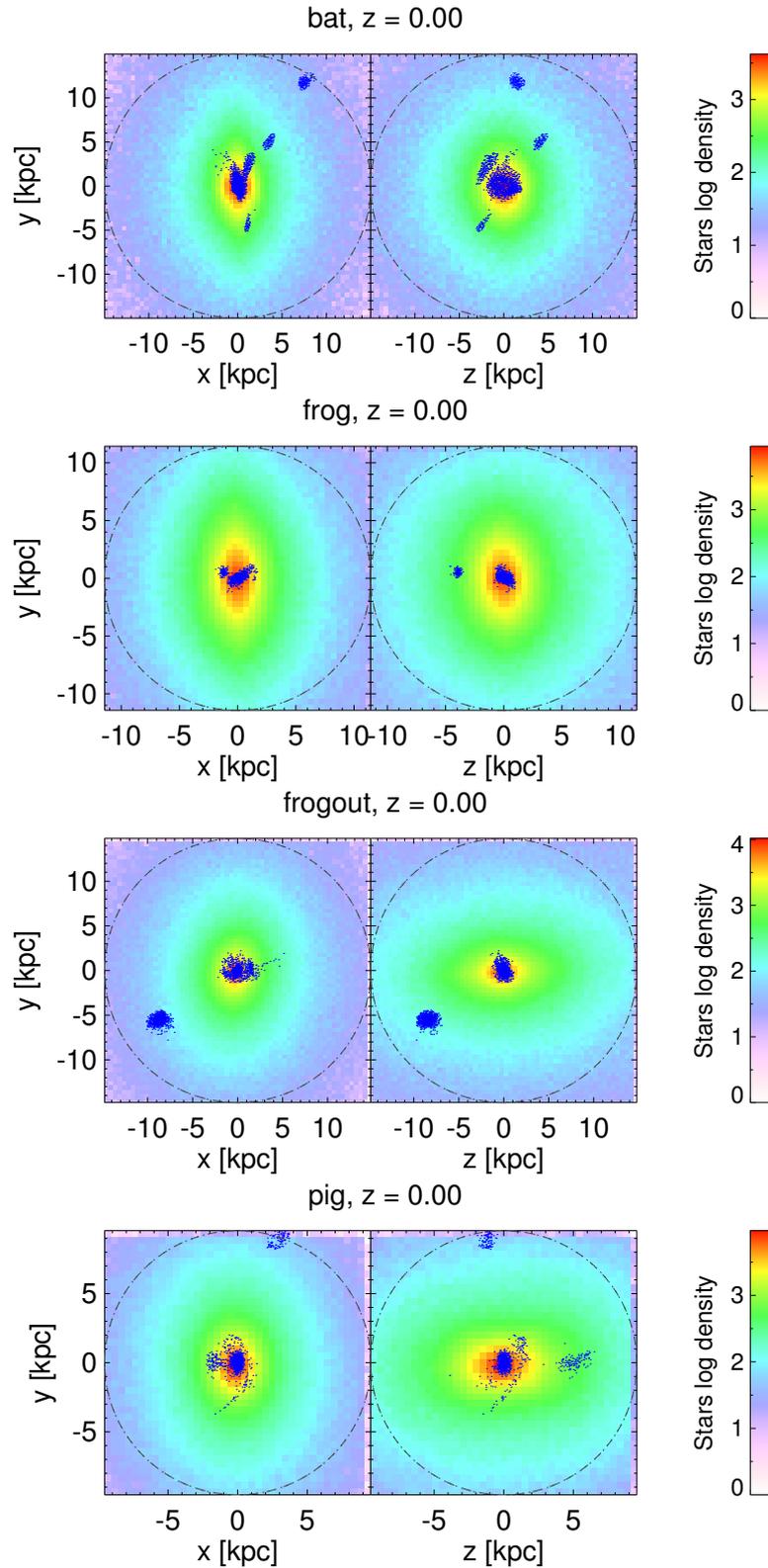
Figure 3.13.: Projections of the stellar mass weighted density along the principal axes. The dash-dotted circle marks the stellar $r_{1/2}$. Overplotted in dark blue are the positions of cold and starforming gas particles inside this radius. Similar to figure 3.2 but inside $r_{1/2}$.
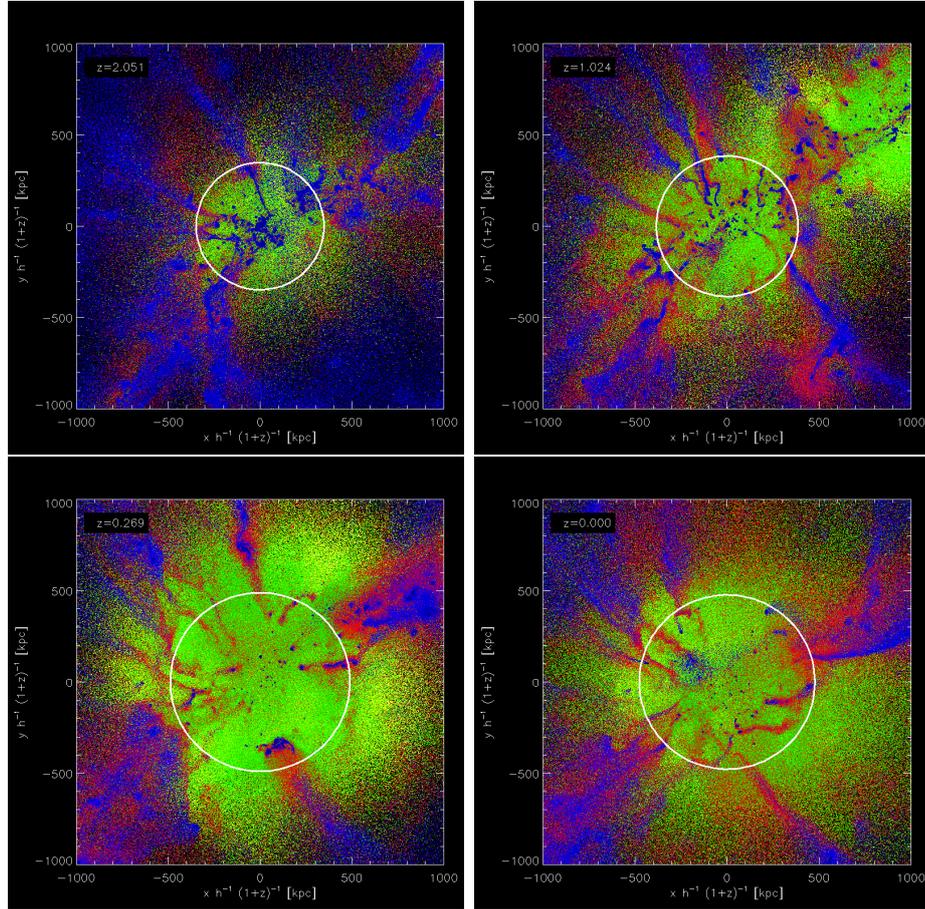
Figure 3.14.: The evolution of the gas distribution in the cosmological environment of Frog at $z = 2, 1, 0.27, 0$ (left to right, top to bottom). Plotted is the projection of all gas particles in a cubic volume L^3 around the object with $L = 2\,h^{-1}\,\mathrm{Mpc}$ in comoving coordinates. Particles are color-coded by their temperature from cold to hot as blue, red, green, yellow. Colder particles overlay warmer ones. The white circle marks the virial radius. See Appendix E for the full time series.

members of the galaxy a that point as identified by the 'subfind' algorithm, i.e. assumed to be bound to the main halo. This is possible as the central structure is not perfectly spherical and can extend slightly beyond r_{vir}. We trace these particles further back in time and take z_{in} when they were not bound to the main halo for the last time. This is usually the case only 1 to 3 snapshots further back and thus has no strong impact on the result. It is however required for our analysis algorithm that distinguishes between smooth and clumpy accretion modes by checking if a given particle is bound to a substructure other than the main halo at z_{in} or not. We also calculate the temperatures of the gas particles at z_{in} to distinguish between hot and cold mode accretion.

The resulting distributions of infall times of the gas that will be cold and in the center of the galaxies at $z = 0$ are shown in figure 3.15. The panels contain the data of our four objects respectively and are organized as described in the following. The two lower parts both contain the same histogram of the infall times, but are color-coded differently. In the middle part the fractions of cold (blue) and hot (red) infalling gas is shown. The lower part distinguishes between the fractions of gas falling in while bound to a stellar substructure (orange) or via smooth accretion (green). The upper part of the panel shows the mass accretion history (MAH) of the total mass of cold gas inside the three radii r_{vir}, $0.1\,r_{vir}$, and $r_{1/2}$ (black, light blue, and red line, respectively).

The upper left panel of figure 3.15 shows the properties for Bat. The distribution of infall times shows that the gas that is eventually cold and in the center of the galaxy at $z = 0$ fell in mainly roughly between $2 - 3.5$ Gyrs ago. Most of it was smoothly accreted and only a small fraction came in bound to a structure. There are two more short accretion events of substructures around 6, and 8 Gyrs ago. None of the accretion is correlated with an obvious event in the mass accretion history of all of the cold gas in the galaxy. The MAH is consistent with a slow depletion of the cold gas reservoir by starformation as was indicated before. The gas is exclusively cold at the time of infall, like in all other objects.

In Frog (upper right panel) the selected gas falls into r_{vir} between 2 and 3.5 Gyrs ago as well, apparently in at least three distinct events. The earlier part of this infall before 3 Gyrs ago is in structures while the later part is mainly smooth. The main gas accretion events happen well after the major merger and therefore can not be related to it, but there might be a correlation to the slowly increasing mass of cold gas inside r_{vir} (black line) after $z = 0.3$ that is probably caused by infall along cold filaments. Visible are also two small early accretion events like in Bat around 6, and 8 Gyrs ago where the gas was transported in by a substructure.

Frogout (lower left panel) shows the broadest continuous distribution of infall times, between 2 and 5 Gyrs ago. It is a mix of smooth and structure accretion from multiple events. The total cold gas mass evolution shows a slight increase inside r_{vir} during this extended period of infall. The increase is also visible with a slight delay of ~ 2 Gyrs in the center of the galaxy. Due to the length of the increase that is not disrupted by a violent event until after 1 Gyr ago, this indicates that the galaxy was resupplied with cold gas through relatively smooth accretion and small

merger events. There is an additional late peak of infall of the selected gas around 1.5 Gyrs ago. The fraction of this gas that crossed r_{vir} in a stellar structure is most likely linked to the merger event at $\approx$ 0.5 Gyrs ago that was also visible in the stellar MAH. The additional large amount of gas that falls in during the short time interval is apparently dense but not bound to any substructure. This indicates that this is due to an unbound cold blob of gas that might be an known artifact of SPH hydrodynamics (Kaufmann et al., 2009). It would be useful to run this simulation again with a more detailed physical description of the hydrodynamics like e.g. metal line cooling and AGNs to test if this cold blob is really a physically stable feature.

The lower right panel of the figure shows the infall times of the selected gas in Pig. Most of it is accreted into the halo in a short period roughly 3 Gyrs ago while being bound to an object. The correlation with the sudden increase of cold gas mass inside r_{vir} and also the total mass M_{vir} (see figure 3.6) at the same time indicate that the major merger that happens to the central galaxy $\sim$ 2 Gyrs later brought the cold gas into the galaxy. Some of the gas that met our selection criteria was accreted at a lookback time of roughly 1.5, 5.5, and 8 Gyrs and predominantly fell in in structures. Like in all of the other four galaxies, the selected gas is cold at the time of accretion, except for an insignificant amount of hot gas that fell in with the substructure 5.5 Gyrs ago.

The latest infall of the selected gas into the virial radius r_{vir} was roughly 1.5 to 2 Gyrs ago for all four galaxies. This can be explain by the spatial distance the gas has to travel from r_{vir} before it reaches the center of the galaxy and fulfills the selection criteria. An approximation of the required time is the free-fall time t_{ff} that is defined as

$$t_{ff} = \sqrt{\frac{3\pi}{32G\bar{\rho}}} \tag{3.4}$$

for a test particle in the gravitational potential of a homogeneous sphere (e.g. (Binney and Tremaine, 1987, p. 38). Here G is the gravitational constant, and $\bar{\rho}$ the mean density of the sphere. As a first approximation we make the assumption that the mass inside the virial radius is homogeneously distributed so that

$$\bar{\rho} = \frac{M_{vir}}{\frac{4}{3}\pi r_{vir}^3} \tag{3.5}$$

and we get $t_{ff} \approx$ 2.6 to 2.7 Gyrs for our galaxies. Given the crudeness of the assumption, this is in quite good agreement with the 2 Gyr gap, so this provides a reasonable explanation for the observed time delay.

We also find that most of the gas that is cold and in the center of the galaxy at $z = 0$ was accreted generally quite late, i.e. around the free-fall time, and exclusively cold. This indicates that the gas must have fallen directly to the center without getting shock heated as it does not have time to cool out of the halo again. Interestingly, although not surprisingly, the object with the most quiet mass accretion history, Bat, has the largest fraction of late smooth accretion of all our four galaxies. Generally, the fraction of cold gas accreted smoothly is between 30%

and 50%, only slightly correlated with the amount of mergers the galaxy suffers throughout its lifetime.

In all galaxies there is only a very small amount of cold gas that was accreted long time ago, i.e. more than 3Gyrs ago. That gas is always accreted bound to a substructure and never smoothly, which suggests that the survival time of cold gas inside the deeper potential well of a substructure is enhanced compared to the timescale on which smoothly accreted cold gas either gets shock heated or forms stars.

Tracing the temperature of these early accreted particles back through all timesteps since their infall into r_{vir} shows that they never got heated to high temperatures, which indicates that clearly that the hot mode accretion via shock heating and the subsequent cooling of the gas out of the halo as observed for some BCGs in a cluster environment, see McDonald et al. (2014), is not important for isolated elliptical galaxies, and that the origin of the origin of the cold gas in those galaxies actually is the accretion of cold gas smoothly through streams and small substructures.

3. Results
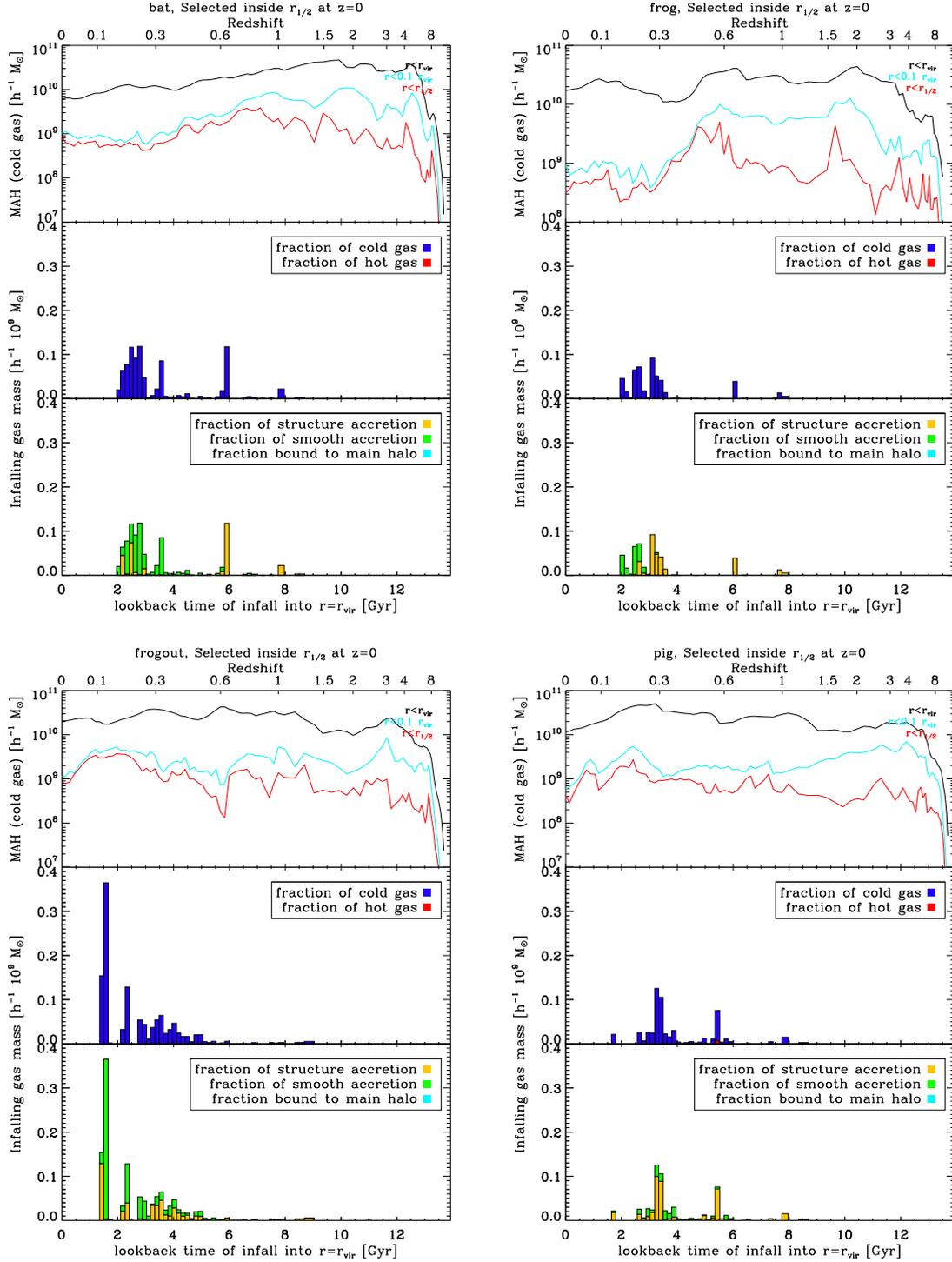
Figure 3.15.: *Upper panels*: Mass accretion histories for the cold gas within r_{vir} (black line), $0.1r_{vir}$ (light blue line) and $r_{1/2}$ (red line). *Middle panels:* Time of infall into r_{vir} of the cold gas which is at $z = 0$ at the center of the galaxies. The histogram bars are not equally wide due to slightly unequally spaced output times of the simulations. Colors according to the legend. *Lower panels:* Same as the middle panels but with colors now coding the fraction of smooth and structured accretion of the gas into r_{vir} (green and yellow respectively). Histograms are cumulative.

60

4. Summary and Conclusions

Recent observations have shown that there exists cold gas in a significant number of elliptical galaxies as present day. This result is puzzling because until recently elliptical were assumed to be red and dead. To understand the origin of this cold gas, we performed a set of high resolution re-simulations of four isolated massive elliptical galaxies chosen from a large DM-only cosmological box with a boxsize of $1 Gpch^{-1}$, using the TreeSPH Code GADGET-3.

In order to ensure that we selected ellipticals, we chose halos in a mass range of $1 \times 10^{13}h^{-1}M_{\odot} < M_{halo} < 1.5 \times 10^{13}h^{-1}M_{\odot}$, which is much larger than any masses observed for spiral galaxies at present day. Additionally, in order to increase the likelihood of finding cold gas in our galaxies, we chose the halos to be as isolated as possible with the constrain that they also dominate the local potential. Thus, the large size of the parent simulation had the advantage that in a larger volume the chances for more extreme environments are enhanced and we therefore had a large number of objects to choose from.

Since re-simulations at the required resolution level are computationally very costly, the first part of this thesis mostly dealt with optimizing the technical and numerical aspects of the re-simulations. The first step in re-simulating any given halo chosen from a parent DM-only simulation is to trace all particles, which are within the volume that should be re-simulated with higher resolution, back to their initial conditions. The resolution of the parent simulation sets a lower limit to the volume that can be re-simulated, because the box size of the high resolution region has to be larger than the smallest scale that is resolved in the power spectrum of the parent simulation. This effectively limits the spatial resolution that can be achieved in the re-simulation at reasonable computational costs.

In our case, the original power spectrum used to create the initial conditions of the parent simulation did not contain the smallest wavelengths required for the initial density perturbations of our highest resolution runs. We therefore had to reconstruct the power spectrum and extend it to include the necessary wavelengths. Once the initial conditions are available, other numerical parameters become important to take into account: If the spatial resolution of the re-simulations reaches a order of magnitude of the numerical round-of errors, single precision in the memory allocation is not suitable anymore, and double precision needs to be used, as otherwise artificial numerical cores are building up in the density distributions of the centers of the simulated ellipticals.

Another, even less well understood issue is the choice of the softening length. We found that the choice of a softening which is too small for a given resolution leads to significant artificial heating which changes the gas physics dramatically even on

4. Summary and Conclusions

large scales. Since this work aims at understanding the origin of gas in galaxies, the choice of a proper softening was highly important.

We conclude from our work, that it is necessary to carefully balance the scientific needs of resolution with the risk of numerical artifacts for each (cosmological) SPH-simulation, as artificial numerical effects, like for example numerical heating, might otherwise inadvertently be misinterpreted as scientific results.

The analysis of the galaxies at $z = 0$ showed that they have physical properties that are in agreement with properties found in observed massive ellipticals. They have, by selection, similar masses but also have the expected sizes as they lie on the observed mass-size relation. Their total radial density profiles are very well fitted by a power law with slopes that are similar to those of other elliptical galaxies from observational and theoretical studies.

Our selection criteria for the targeted galaxies were only biased towards isolated and massive galaxies, but we found examples of very different formation mechanisms for elliptical galaxies. One of the galaxies was a compact massive elliptical at a high redshift that had a quiet accretion history and developed in mass and size along the path predicted from the results of observations of comparable objects. The sample also includes a self-consistently formed spiral galaxy that transformed into an elliptical by in major merger event that is similar to those often studied in idealized simulations of binary mergers. The third object shows yet another evolutionary path by which an elliptical can form, namely via the multiple merger scenario of continuous growths through dynamically violent events. The forth galaxy in the sample accumulated its final mass very late in its history, in a late, dry major merger that left shell structures in the stellar distribution that are still clearly observable today.

When we study the distribution of cold gas in the centers of the simulated ellipticals, we find that the cold gas is mostly not aligned with the stellar distribution and shows signs of recent infall, a clear indication that the main source of this gas is external. The time of its infall into the galaxies virial radius is remarkably close to the estimated free-fall time for a large fraction of the gas, and it falls in exclusively cold. This also shows that cooling out of the hot halo is not significant for the massive ellipticals in our sample. There is only a weak correlation between smooth or structured accretion and the evolution history where the galaxy with the most quiet history has the largest fraction of smooth accretion and a massive merger can only contribute to the final cold gas reservoir if it happens very late. The otherwise lack of correlation with the dynamical state of the galaxy strongly suggests that the environment is the main driver for the acquisition of the gas that is cool and in the center of the galaxy at $z = 0$ and that cold mode accretion along of filaments or in small structures is the main origin of the gas.

A. Bat
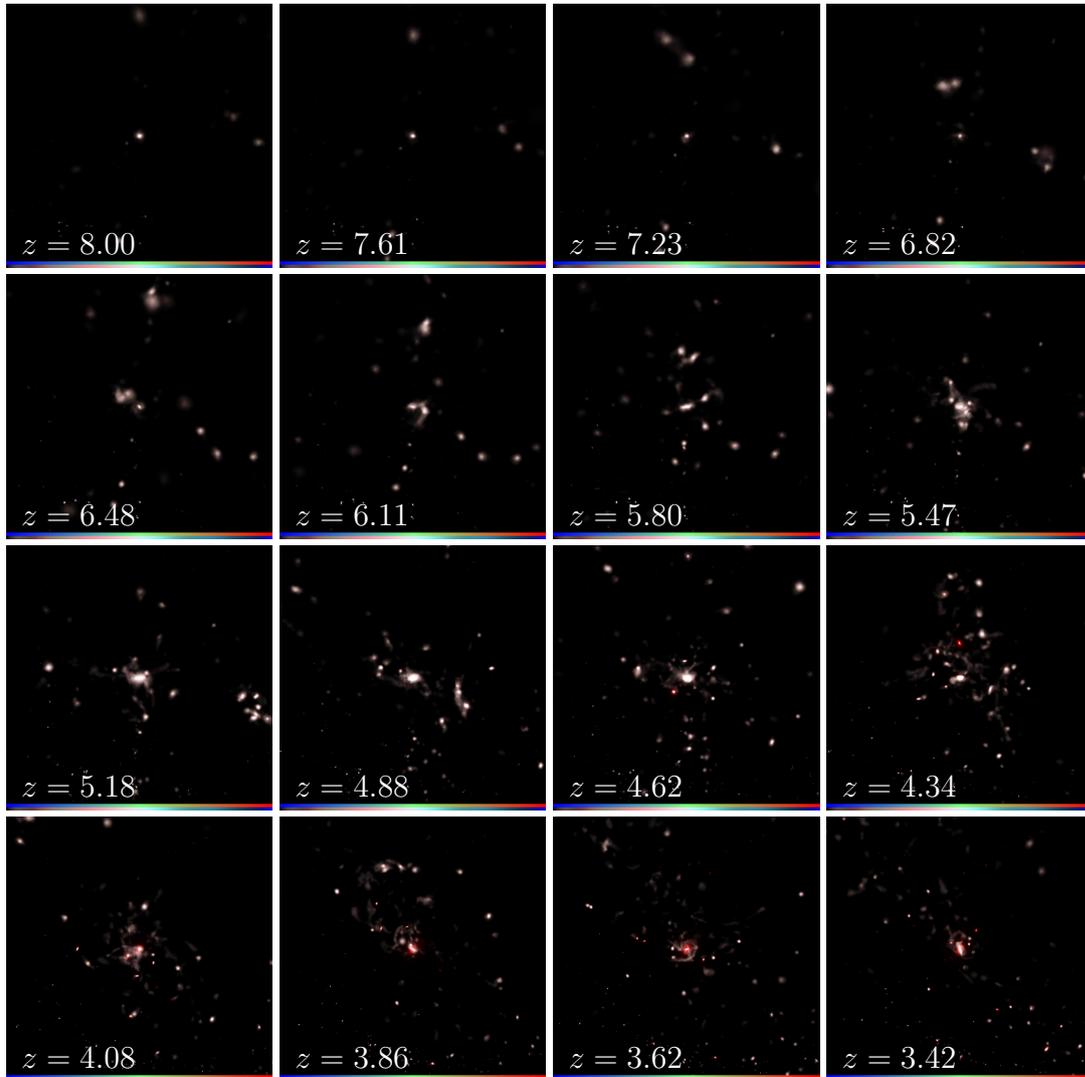
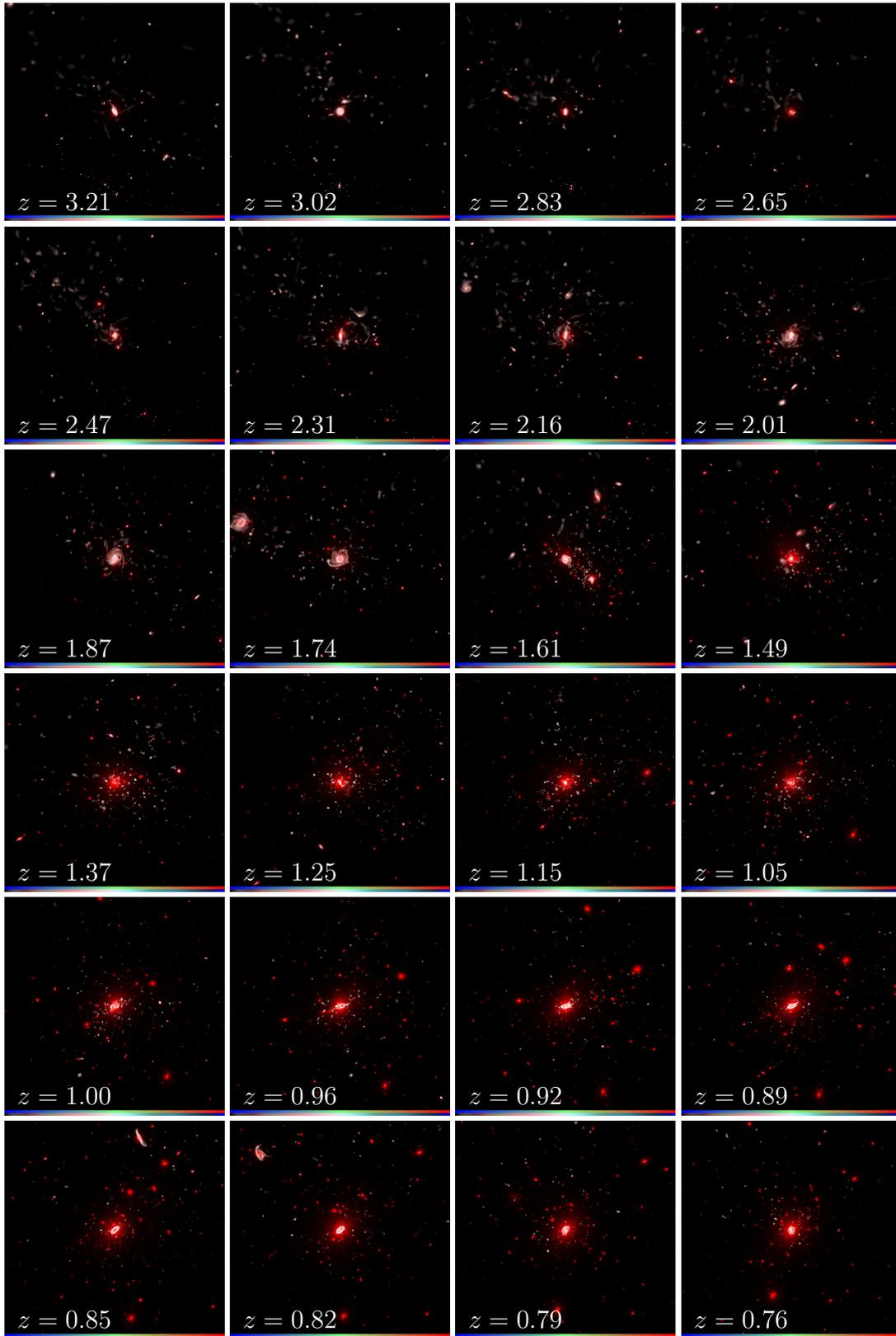**Figure A.1.:** Time evolution of the galaxy Bat from redshift $z = 8$ to $z = 0$
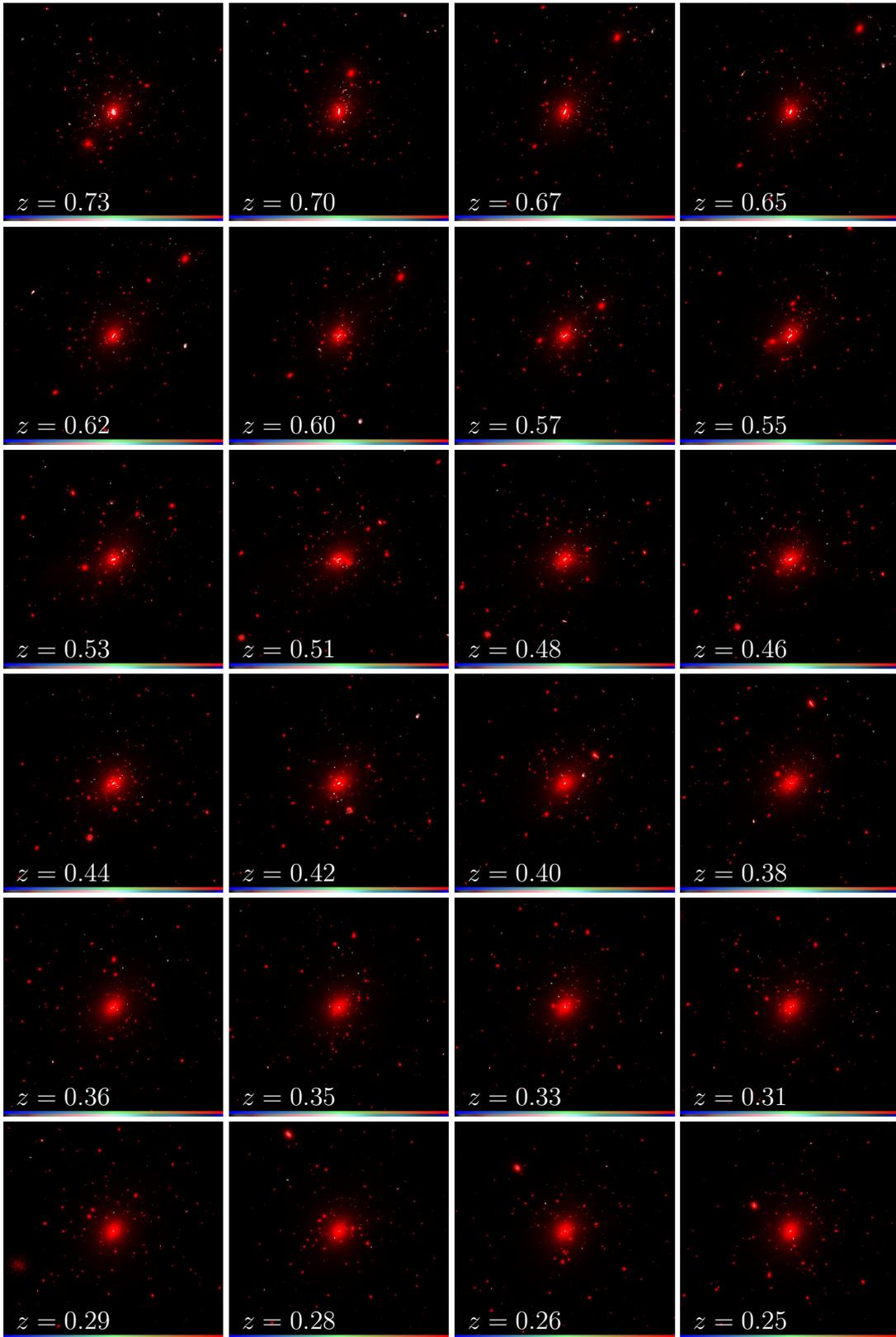
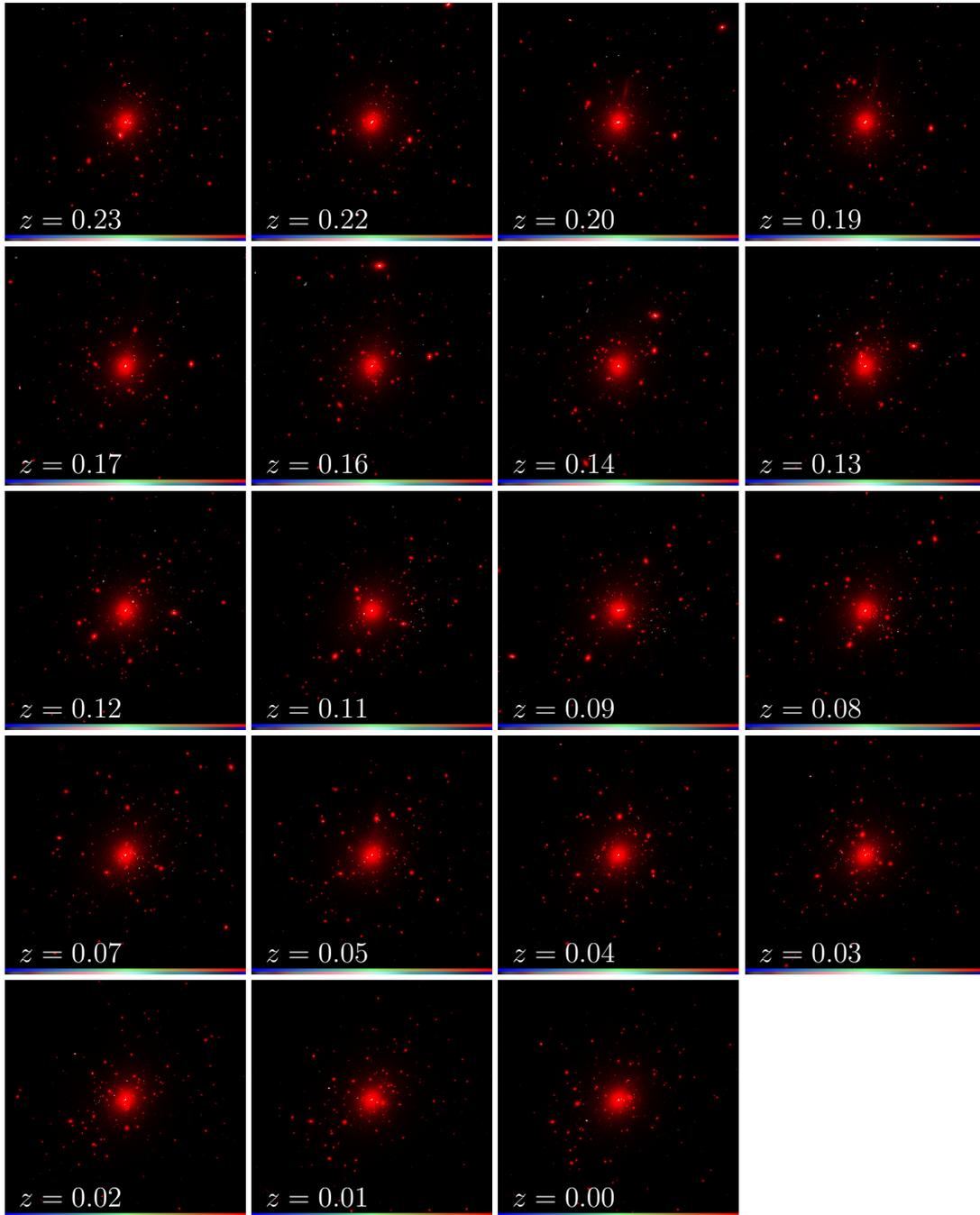**Figure A.2.:** continuing
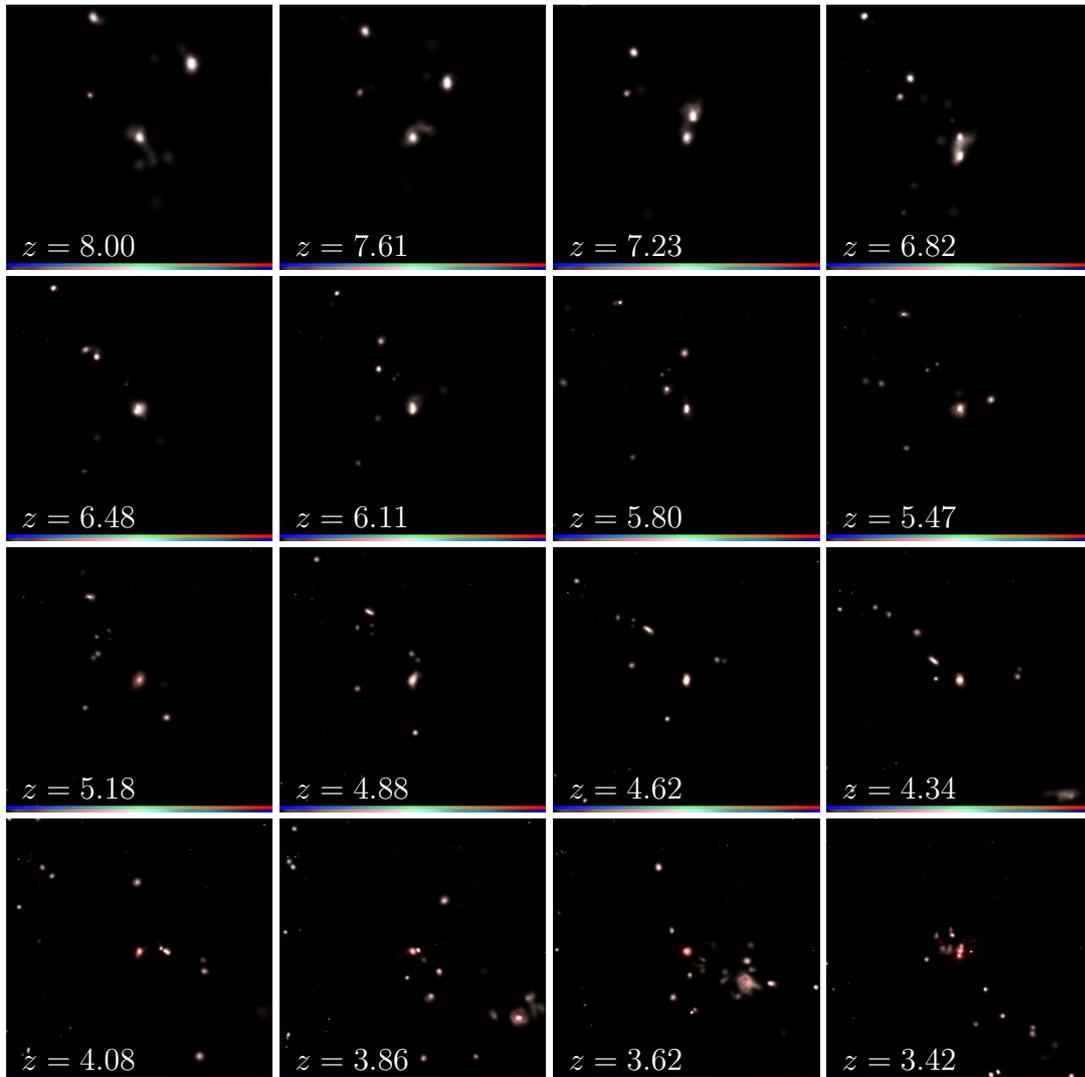
Figure A.3.: continuing

Figure A.4.: continuing

B. Frog

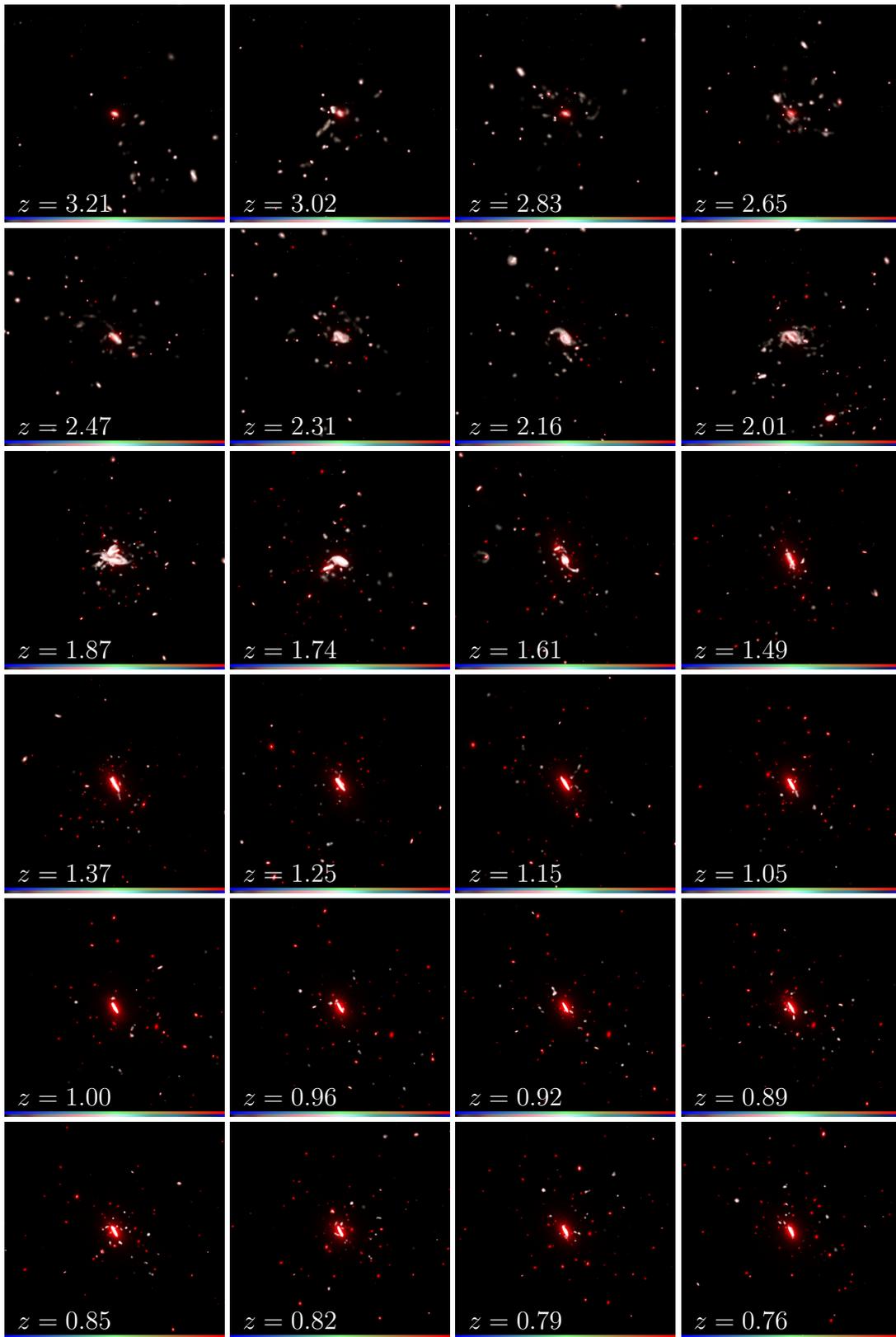**Figure B.1.:** Time evolution of the galaxy Frog from redshift $z = 8$ to $z = 0$
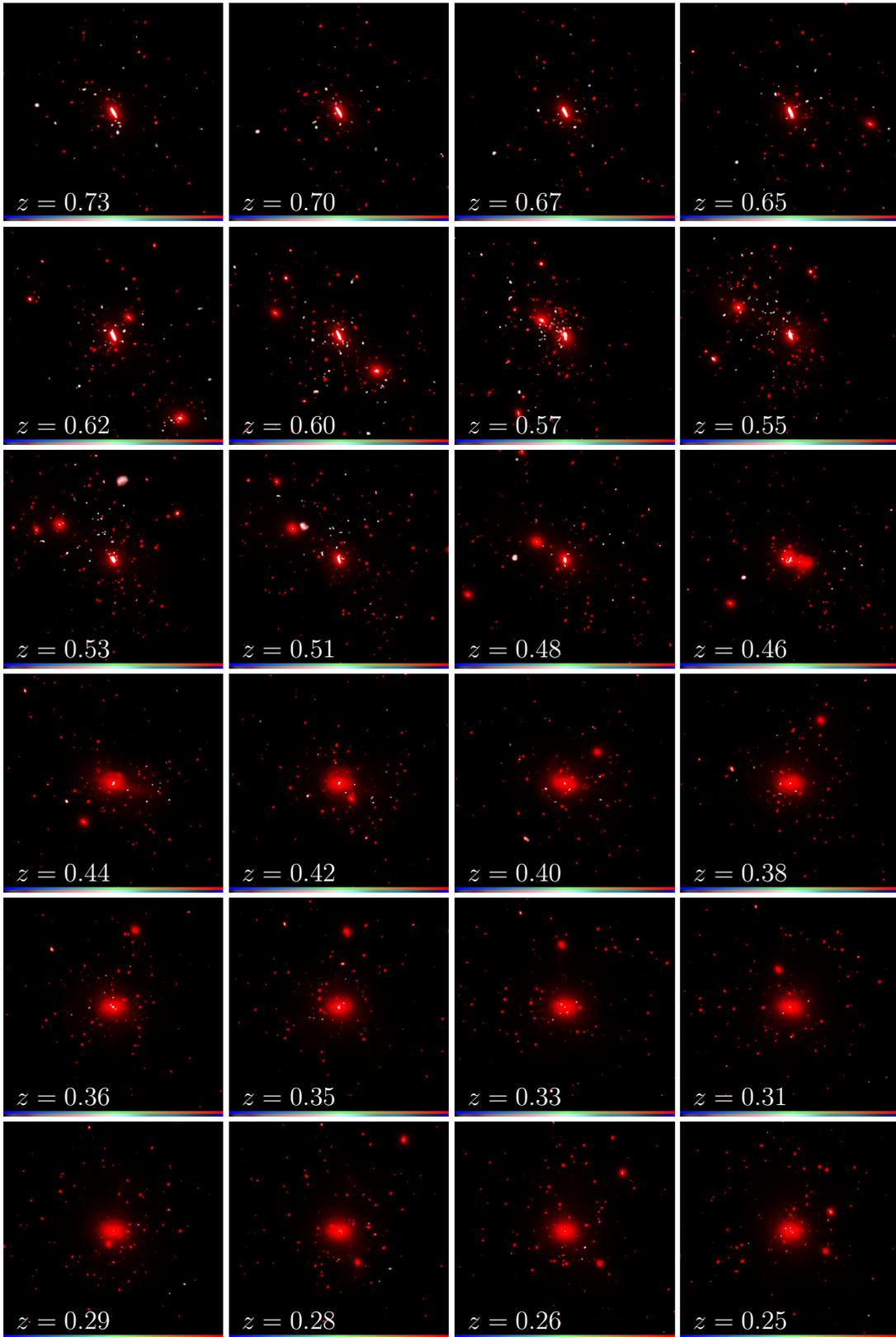
Figure B.2.: continuing

$z = 0.73$

$z = 0.70$

$z = 0.67$

$z = 0.65$

$z = 0.62$

$z = 0.60$

$z = 0.57$

$z = 0.55$

$z = 0.53$

$z = 0.51$

$z = 0.48$

$z = 0.46$

$z = 0.44$

$z = 0.42$

$z = 0.40$

$z = 0.38$

$z = 0.36$

$z = 0.35$

$z = 0.33$

$z = 0.31$

$z = 0.29$

$z = 0.28$

$z = 0.26$

$z = 0.25$

Figure B.3.: continuing

$z = 0.23$ $z = 0.22$ $z = 0.20$ $z = 0.19$

$z = 0.17$ $z = 0.16$ $z = 0.14$ $z = 0.13$

$z = 0.12$ $z = 0.11$ $z = 0.09$ $z = 0.08$

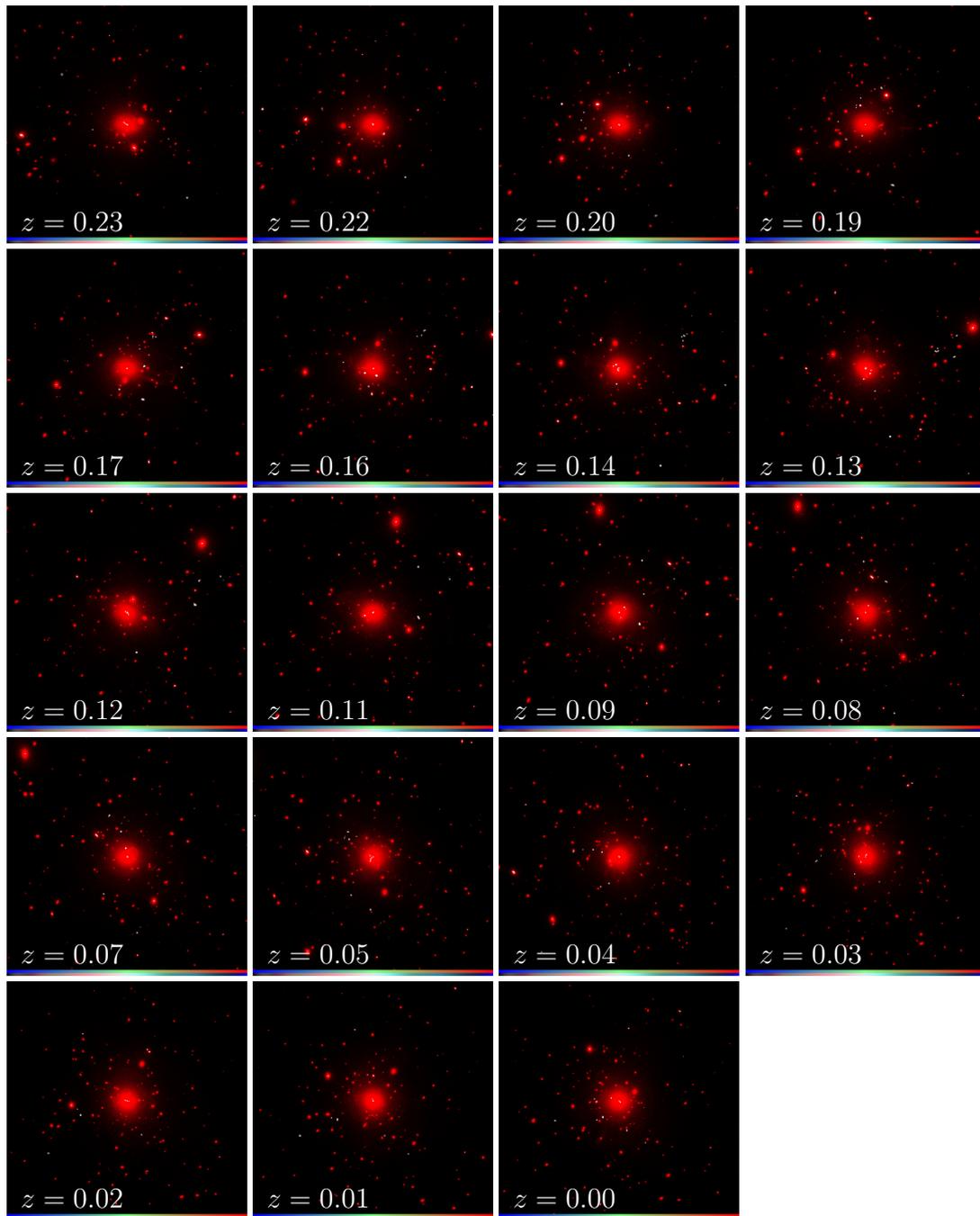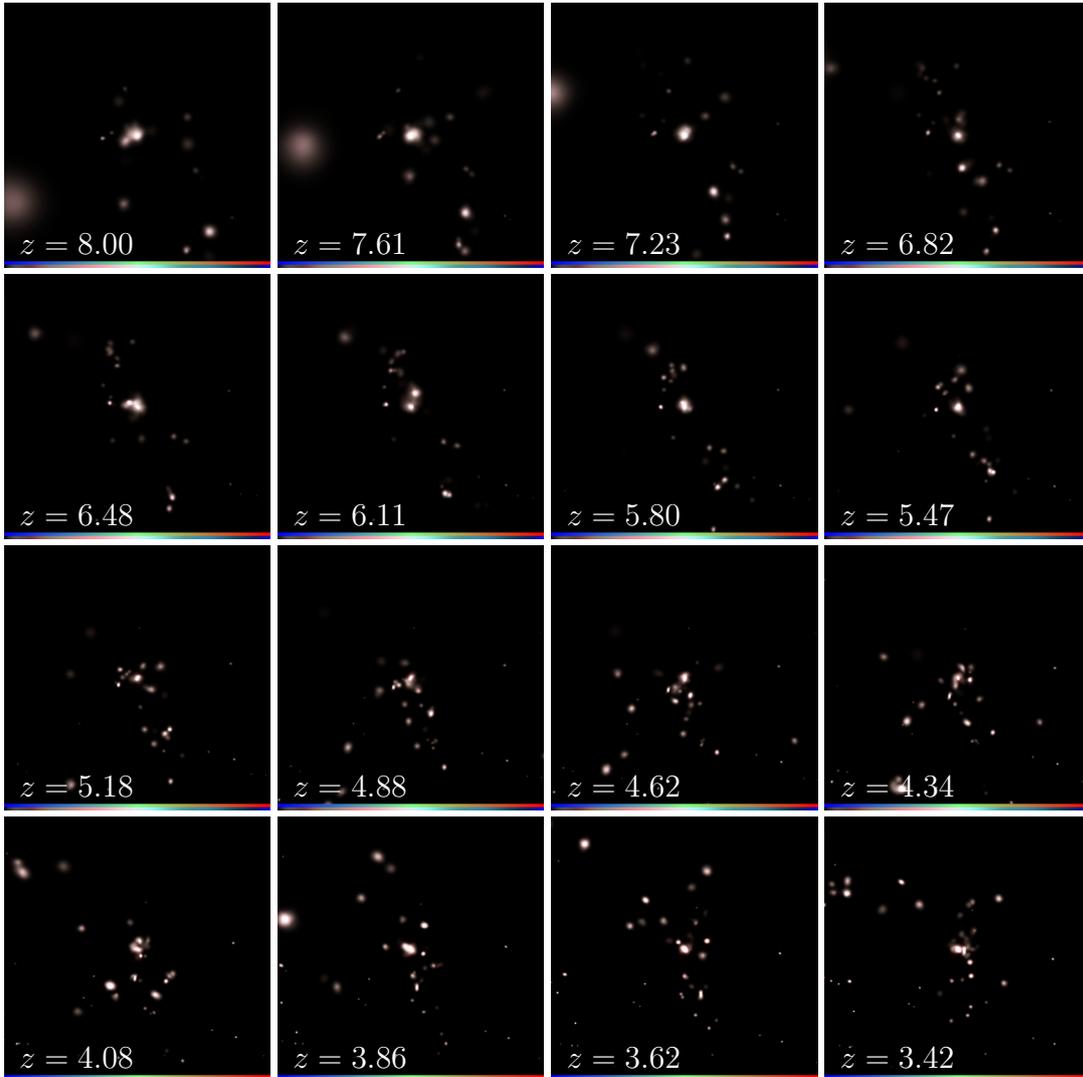$z = 0.07$ $z = 0.05$ $z = 0.04$ $z = 0.03$

$z = 0.02$ $z = 0.01$ $z = 0.00$

Figure B.4.: continuing

C. FrogOut

Figure C.1.: Time evolution of the galaxy Frogout from redshift $z = 8$ to $z = 0$

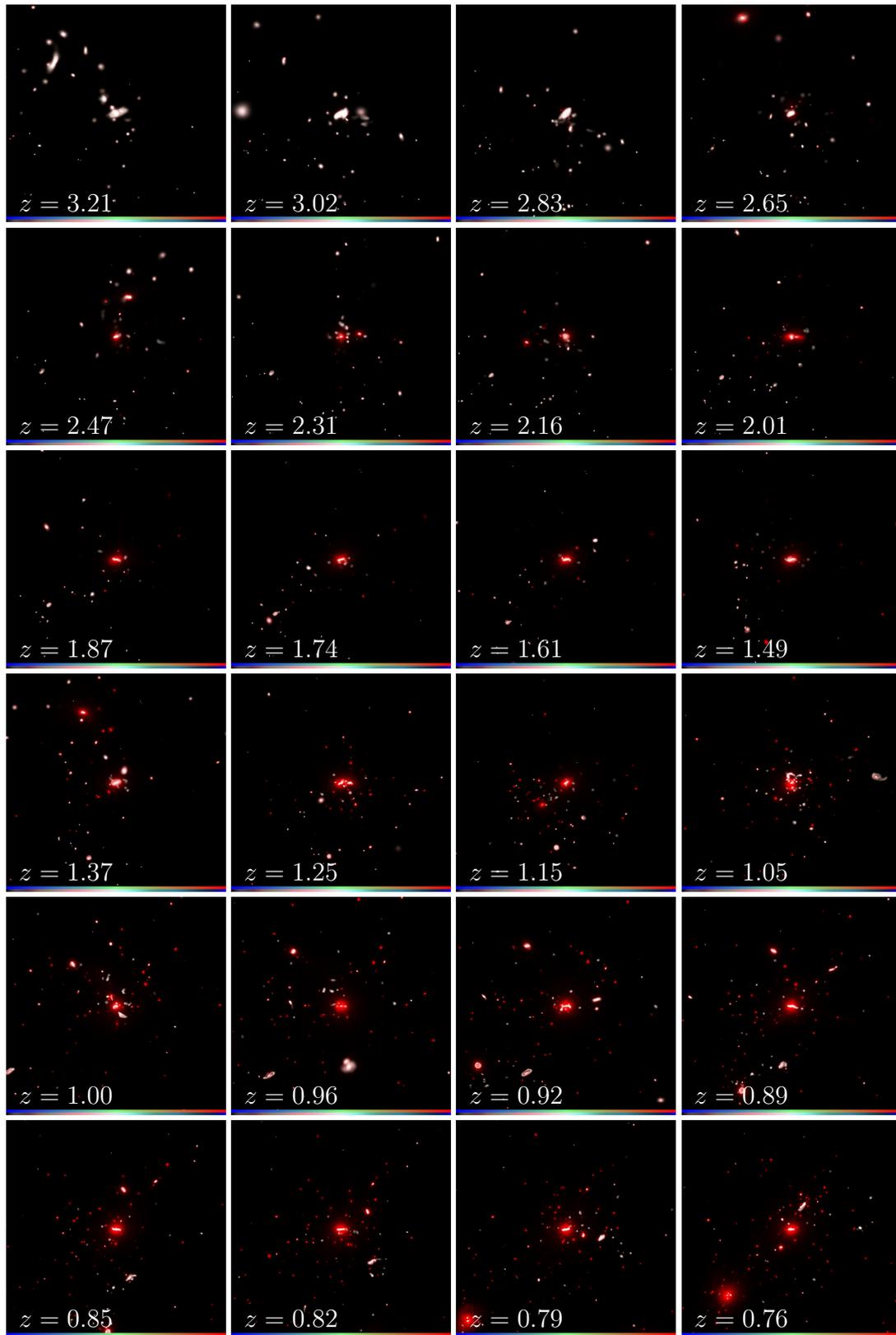$z = 3.21$ $z = 3.02$ $z = 2.83$ $z = 2.65$

$z = 2.47$ $z = 2.31$ $z = 2.16$ $z = 2.01$

$z = 1.87$ $z = 1.74$ $z = 1.61$ $z = 1.49$

$z = 1.37$ $z = 1.25$ $z = 1.15$ $z = 1.05$

$z = 1.00$ $z = 0.96$ $z = 0.92$ $z = 0.89$

$z = 0.85$ $z = 0.82$ $z = 0.79$ $z = 0.76$

Figure C.2.: continuing

Figure C.3.: continuing

$z = 0.23$ $z = 0.22$ $z = 0.20$ $z = 0.19$

$z = 0.17$ $z = 0.16$ $z = 0.14$ $z = 0.13$

$z = 0.12$ $z = 0.11$ $z = 0.09$ $z = 0.08$

$z = 0.07$ $z = 0.05$ $z = 0.04$ $z = 0.03$

$z = 0.02$ $z = 0.01$ $z = 0.00$

Figure C.4.: continuing

D. Pig

Figure D.1.: Time evolution of the galaxy Pig from redshift $z = 8$ to $z = 0$
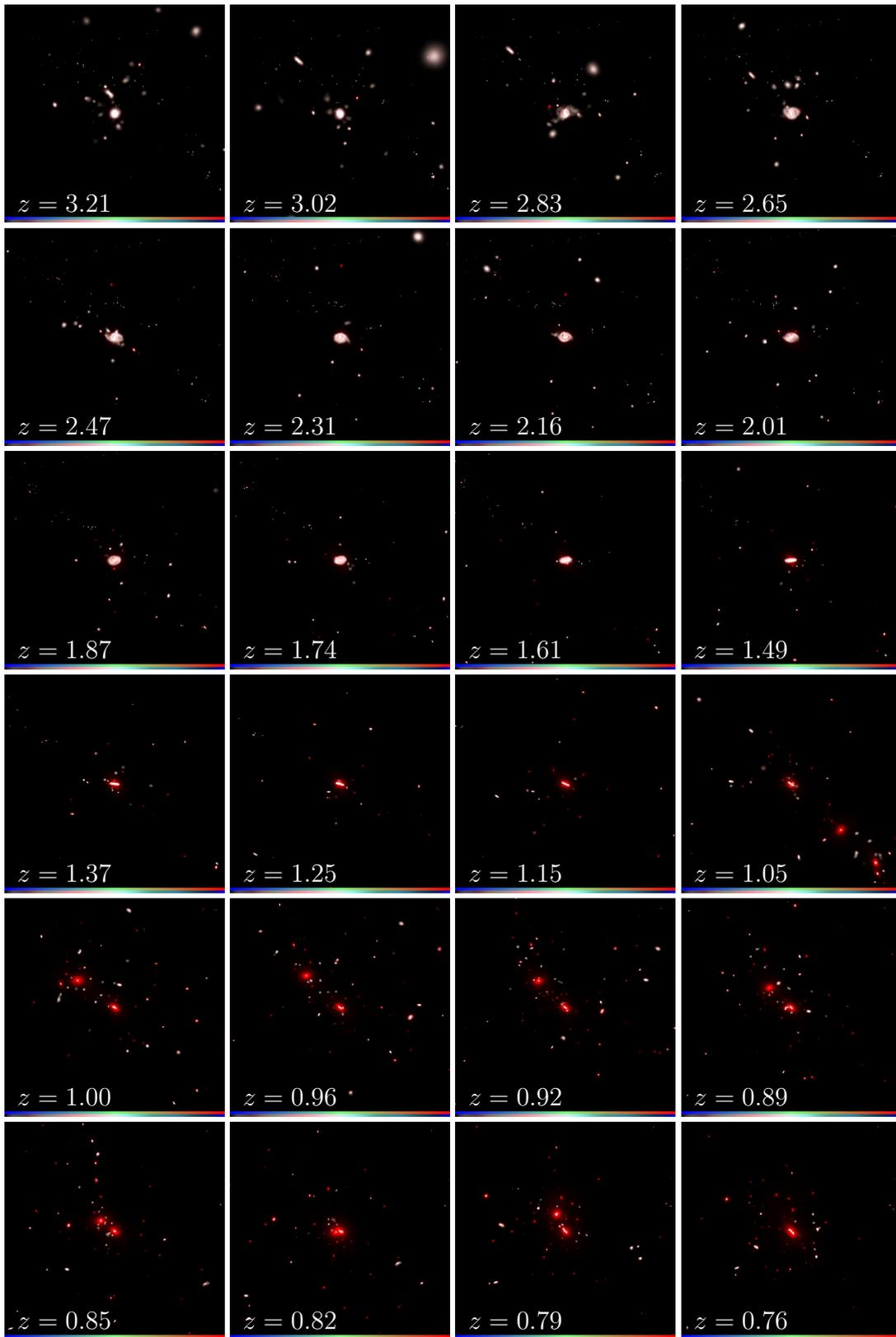
Figure D.2.: continuing

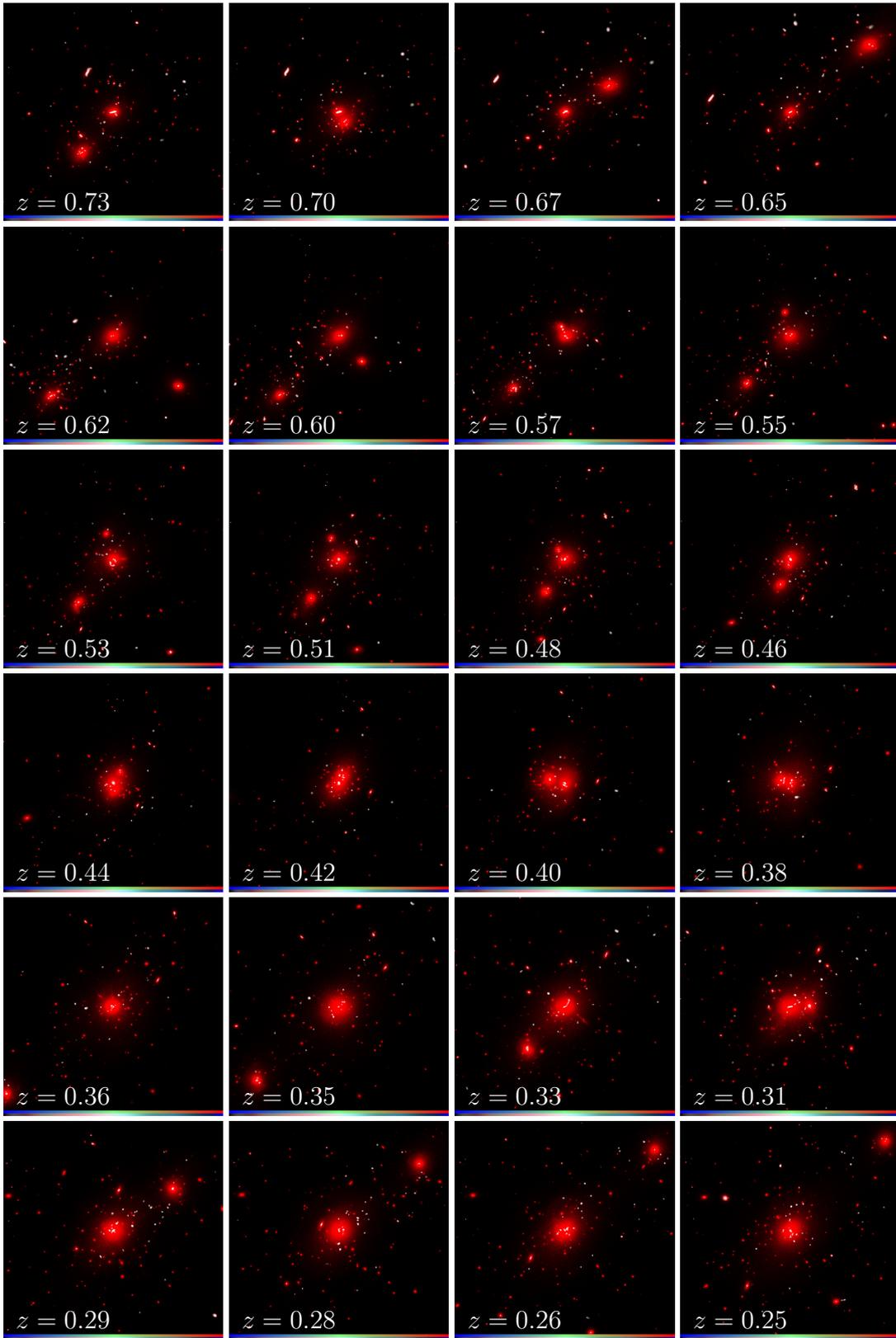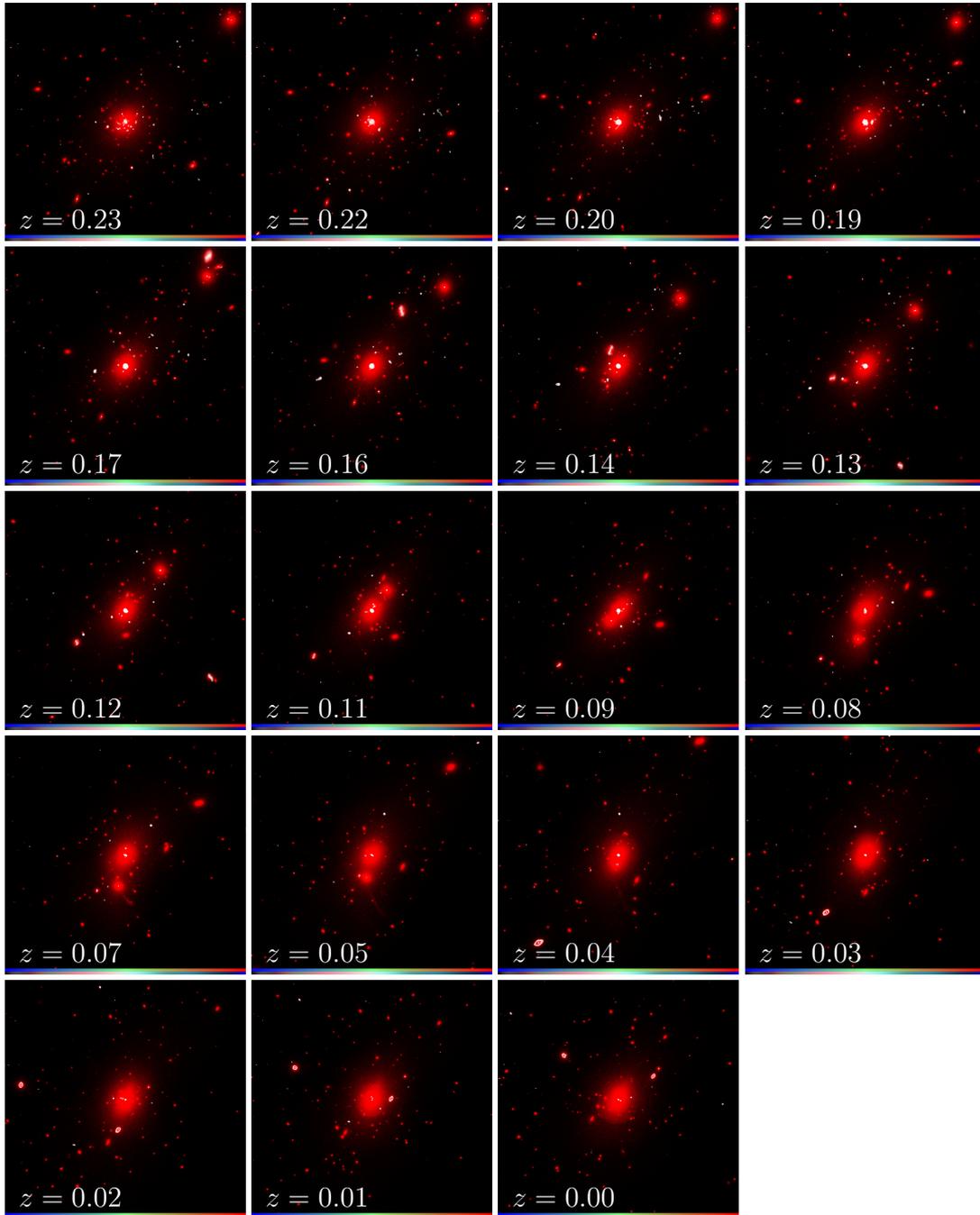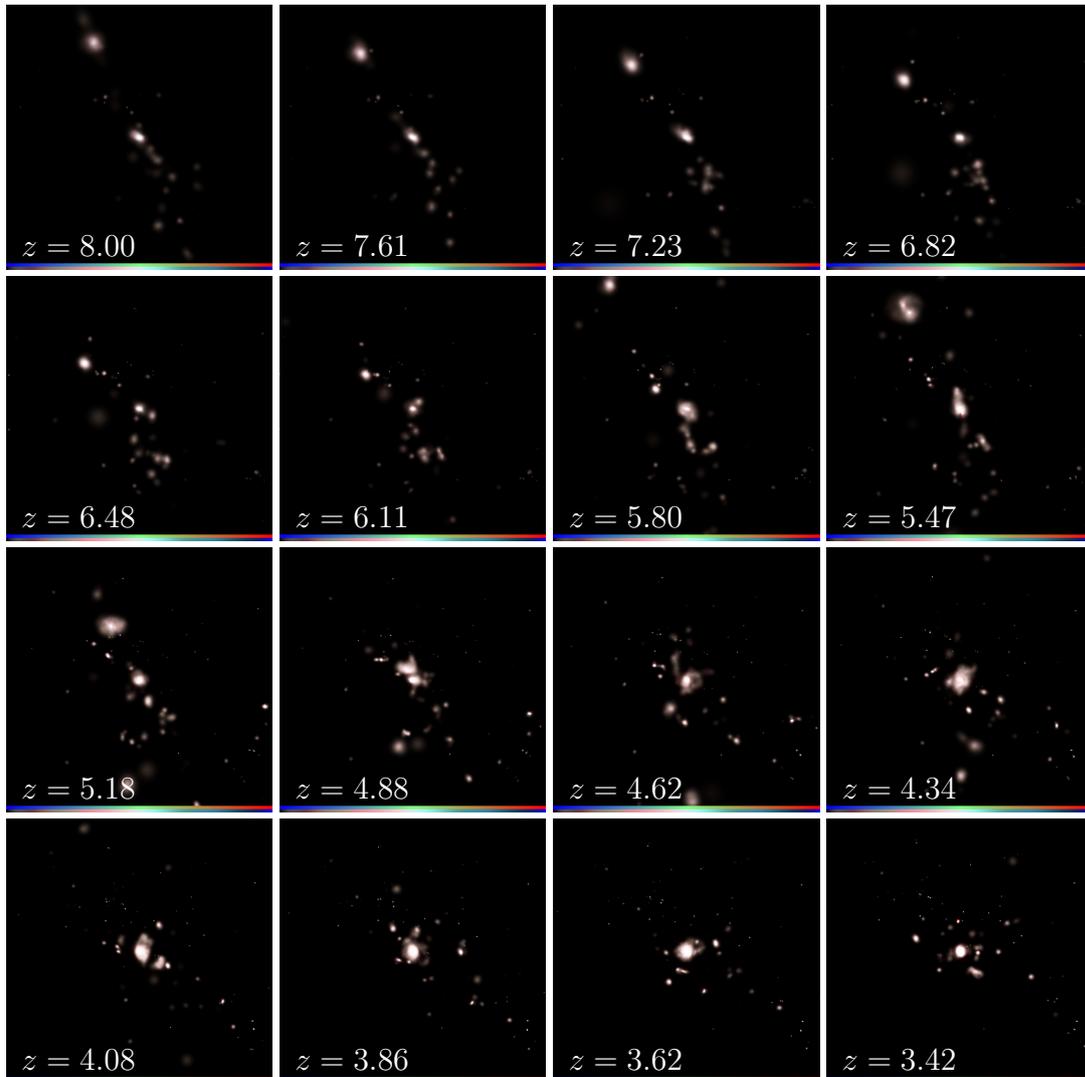**Figure D.3.:** continuing

$z = 0.23$ $z = 0.22$ $z = 0.20$ $z = 0.19$

$z = 0.17$ $z = 0.16$ $z = 0.14$ $z = 0.13$

$z = 0.12$ $z = 0.11$ $z = 0.09$ $z = 0.08$

$z = 0.07$ $z = 0.05$ $z = 0.04$ $z = 0.03$

$z = 0.02$ $z = 0.01$ $z = 0.00$

Figure D.4.: continuing

E. Frog long

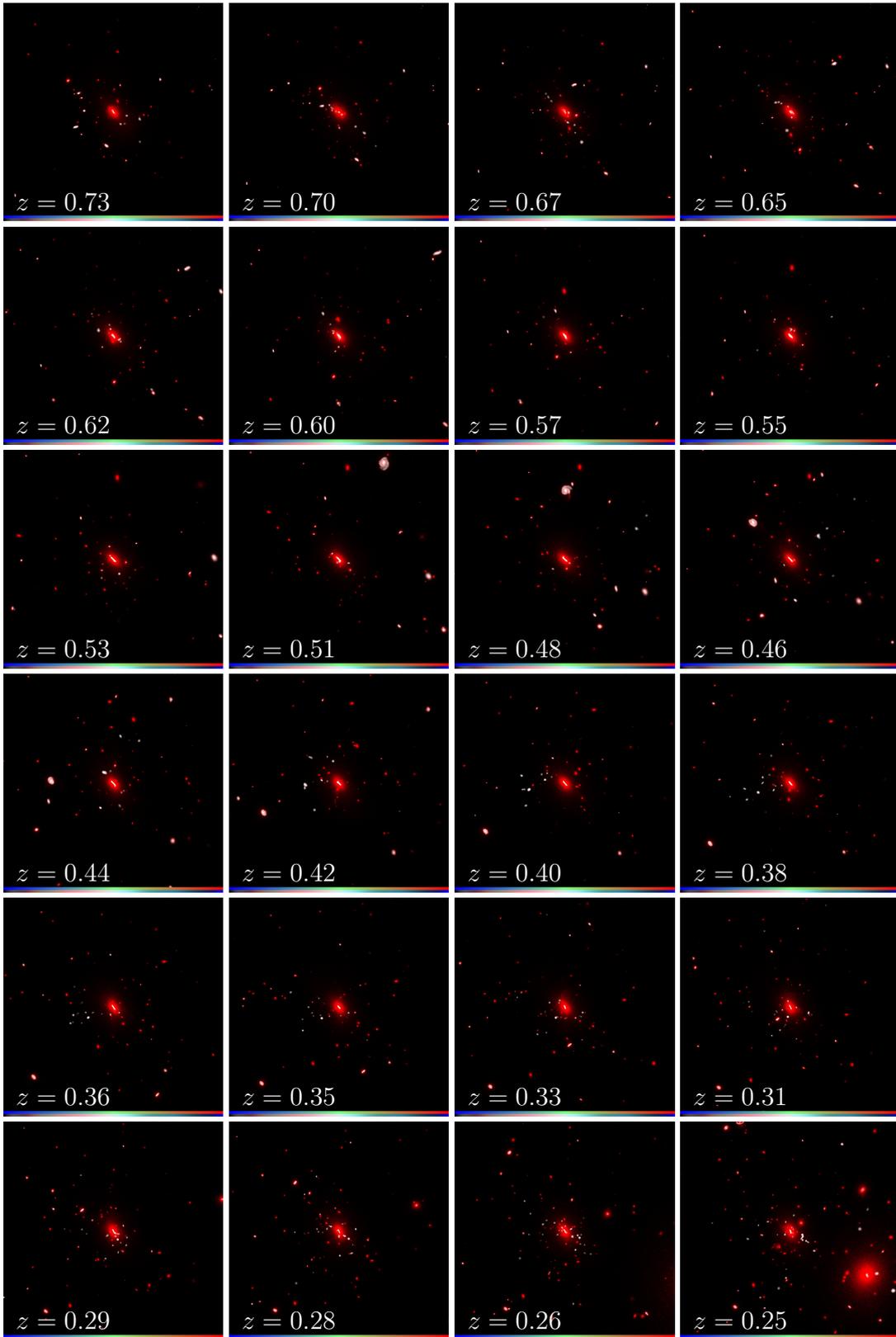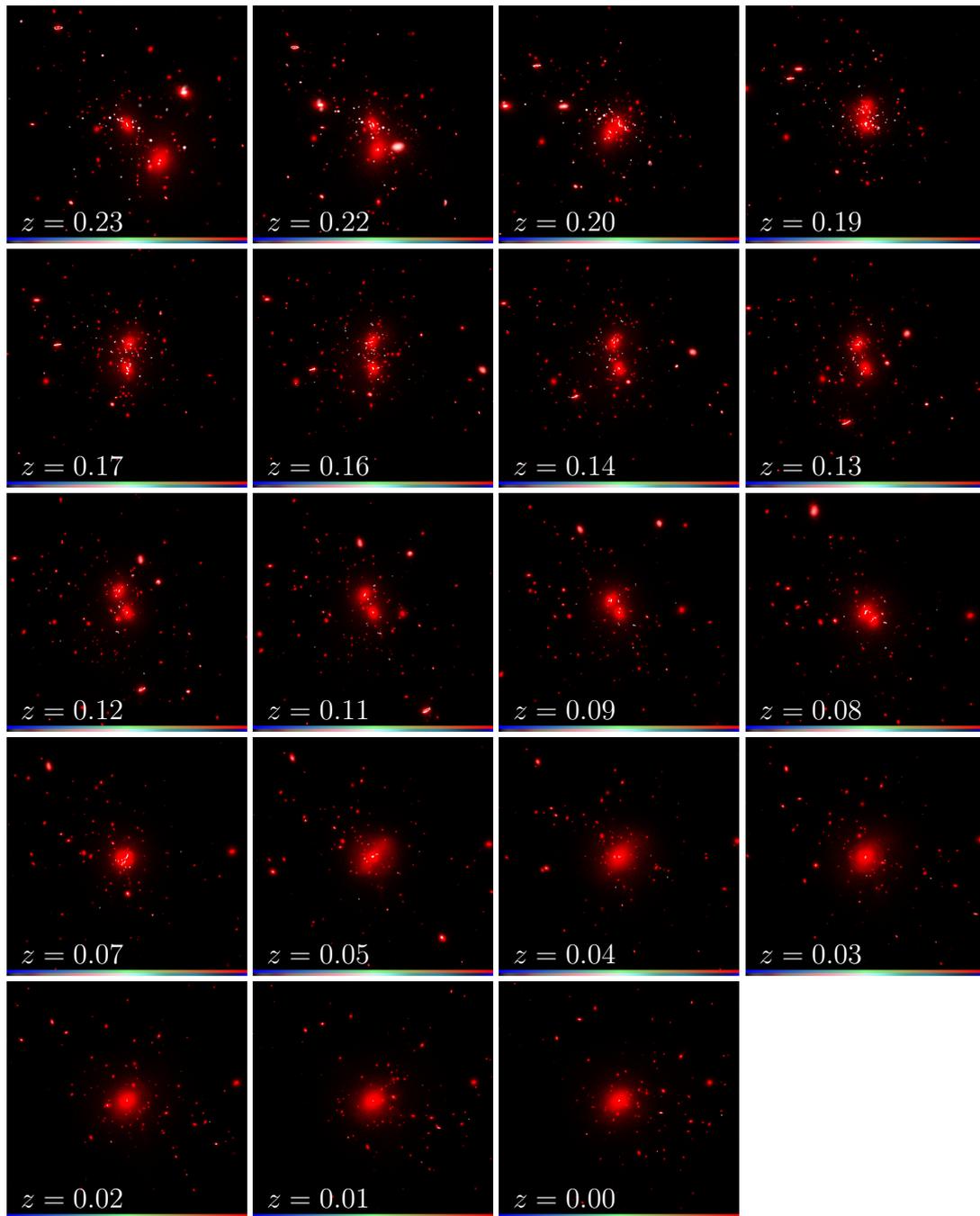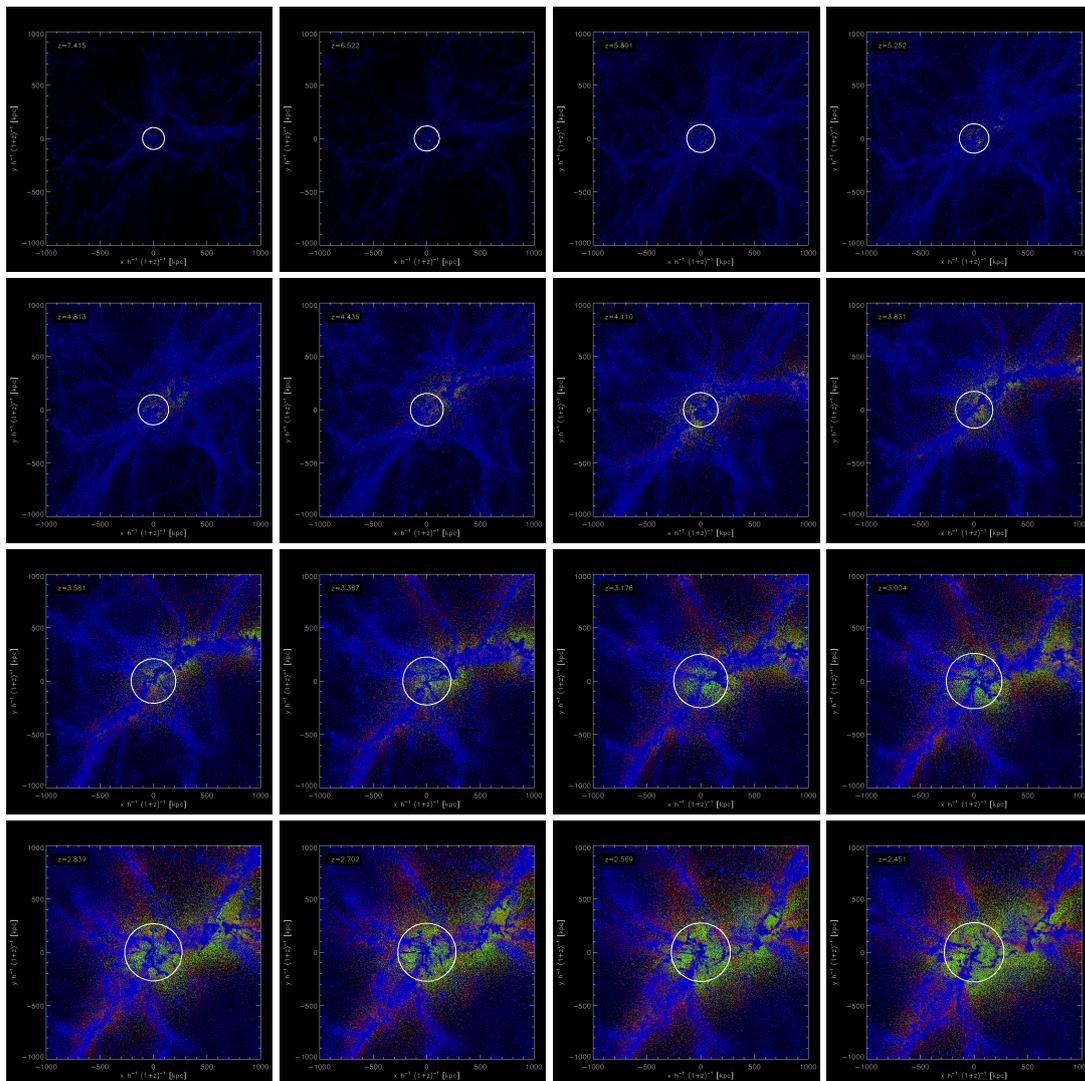**Figure E.1.:** Time evolution of the gas in the cosmological environment in Frog.
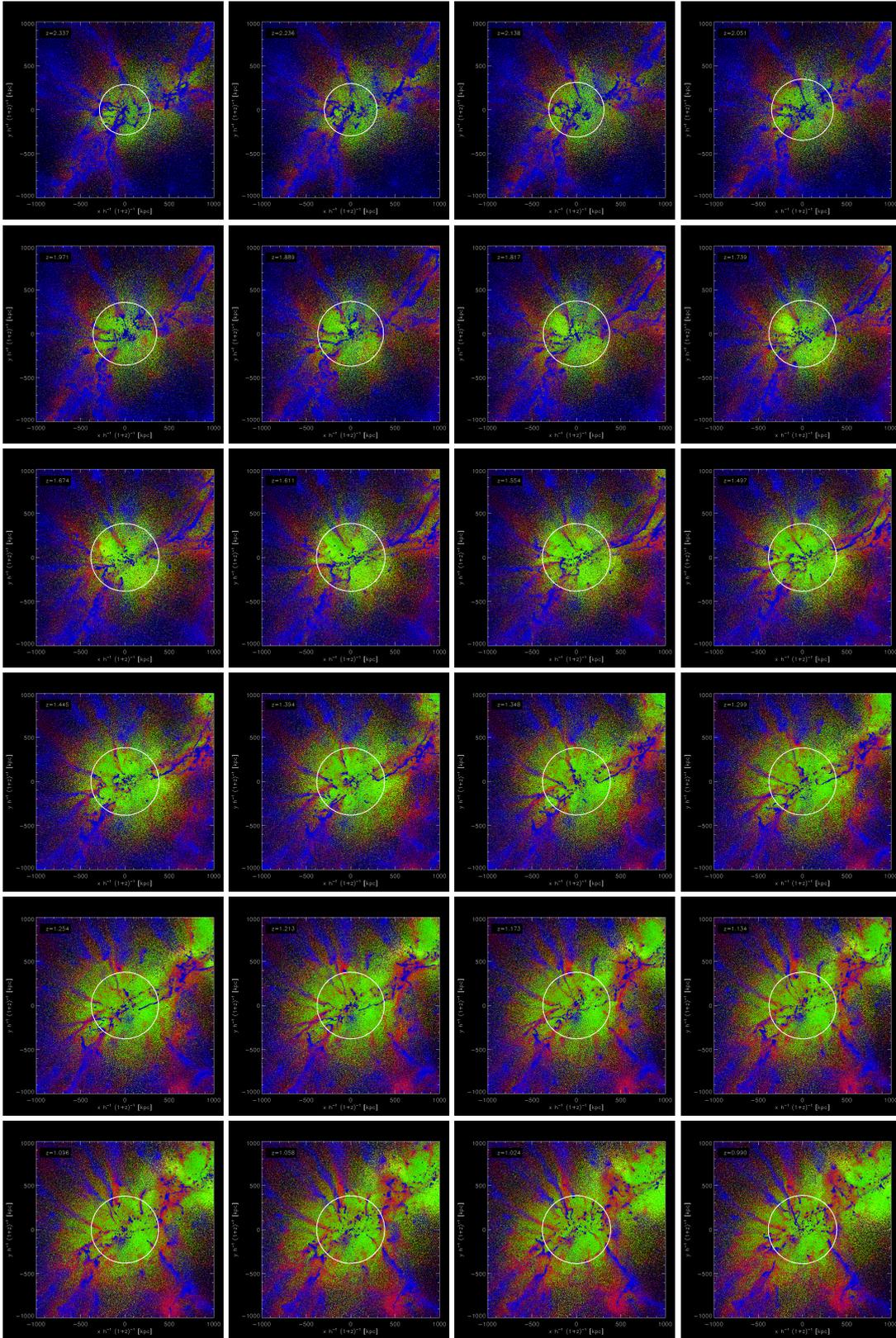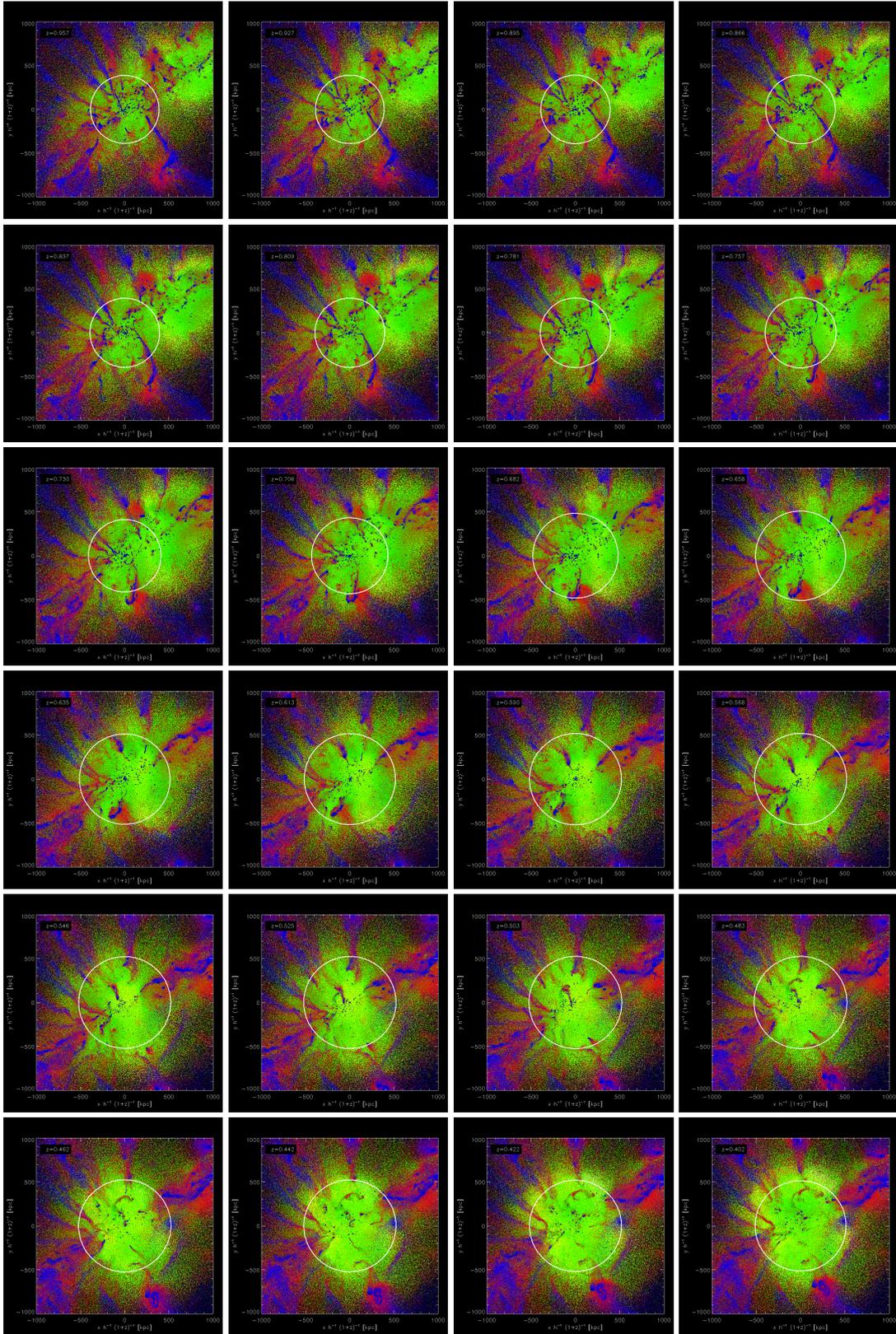
Figure E.2.: continuing
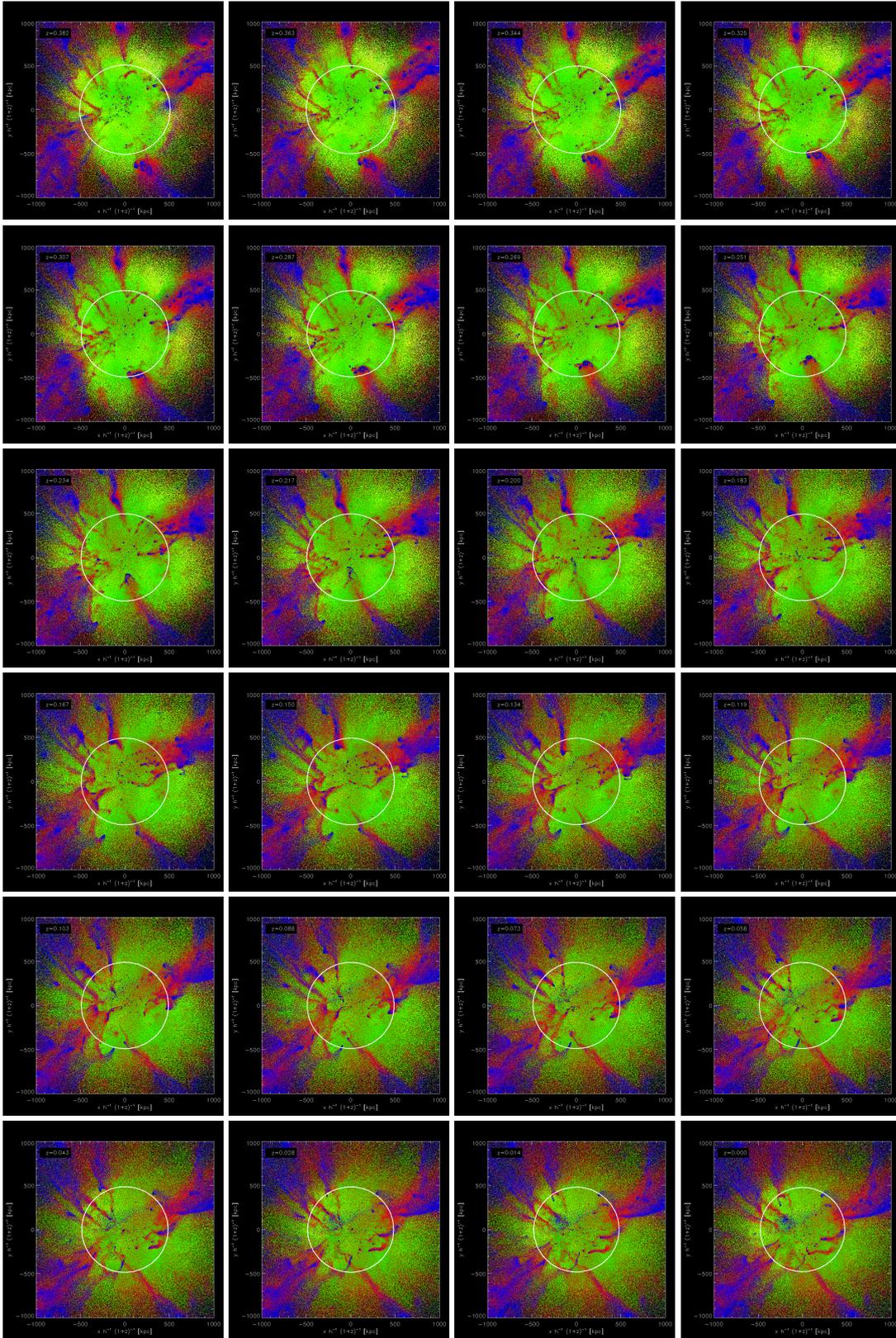
Figure E.3.: continuing

Figure E.4.: continuing

Bibliography

Anderson, M. E. and Bregman, J. N. (2011). Detection of a Hot Gaseous Halo around the Giant Spiral Galaxy NGC 1961. *The Astrophysical Journal*, 737:22.

Auger, M. W., Treu, T., Bolton, A. S., Gavazzi, R., Koopmans, L. V. E., Marshall, P. J., Moustakas, L. A., and Burles, S. (2010). The Sloan Lens ACS Survey. X. Stellar, Dynamical, and Total Mass Correlations of Massive Early-type Galaxies. *The Astrophysical Journal*, 724:511–525.

Barnabè, M., Czoske, O., Koopmans, L. V. E., Treu, T., and Bolton, A. S. (2011). Two-dimensional kinematics of SLACS lenses - III. Mass structure and dynamics of early-type lens galaxies beyond z 0.1. *Monthly Notices of the Royal Astronomical Society*, 415:2215–2232.

Bennett, C. L., Larson, D., Weiland, J. L., Jarosik, N., Hinshaw, G., Odegard, N., Smith, K. M., Hill, R. S., Gold, B., Halpern, M., Komatsu, E., Nolta, M. R., Page, L., Spergel, D. N., Wollack, E., Dunkley, J., Kogut, A., Limon, M., Meyer, S. S., Tucker, G. S., and Wright, E. L. (2013). Nine-year Wilkinson Microwave Anisotropy Probe (WMAP) Observations: Final Maps and Results. *Astrophysical Journal Supplement Series*, 208:20.

Binney, J. and Tremaine, S. (1987). *Galactic dynamics*.

Bonafede, A., Dolag, K., Stasyszyn, F., Murante, G., and Borgani, S. (2011). A non-ideal magnetohydrodynamic GADGET: simulating massive galaxy clusters. *Monthly Notices of the Royal Astronomical Society*, 418:2234–2250.

Borgani, S. and Viel, M. (2009). The evolution of a pre-heated intergalactic medium. *Monthly Notices of the Royal Astronomical Society*, 392:L26–L30.

Cappellari, M., Emsellem, E., Krajnović, D., McDermid, R. M., Scott, N., Verdoes Kleijn, G. A., Young, L. M., Alatalo, K., Bacon, R., Blitz, L., Bois, M., Bournaud, F., Bureau, M., Davies, R. L., Davis, T. A., de Zeeuw, P. T., Duc, P.-A., Khochfar, S., Kuntschner, H., Lablanche, P.-Y., Morganti, R., Naab, T., Oosterloo, T., Sarzi, M., Serra, P., and Weijmans, A.-M. (2011a). The ATLAS^{3D} project - I. A volume-limited sample of 260 nearby early-type galaxies: science goals and selection criteria. *Monthly Notices of the Royal Astronomical Society*, 413:813–836.

Bibliography

Cappellari, M., Emsellem, E., Krajnović, D., McDermid, R. M., Serra, P., Alatalo, K., Blitz, L., Bois, M., Bournaud, F., Bureau, M., Davies, R. L., Davis, T. A., de Zeeuw, P. T., Khochfar, S., Kuntschner, H., Lablanche, P.-Y., Morganti, R., Naab, T., Oosterloo, T., Sarzi, M., Scott, N., Weijmans, A.-M., and Young, L. M. (2011b). The ATLAS^{3D} project - VII. A new look at the morphology of nearby galaxies: the kinematic morphology-density relation. *Monthly Notices of the Royal Astronomical Society*, 416:1680–1696.

Cappellari, M., Scott, N., Alatalo, K., Blitz, L., Bois, M., Bournaud, F., Bureau, M., Crocker, A. F., Davies, R. L., Davis, T. A., de Zeeuw, P. T., Duc, P.-A., Emsellem, E., Khochfar, S., Krajnović, D., Kuntschner, H., McDermid, R. M., Morganti, R., Naab, T., Oosterloo, T., Sarzi, M., Serra, P., Weijmans, A.-M., and Young, L. M. (2013). The ATLAS^{3D} project - XV. Benchmark for early-type galaxies scaling relations from 260 dynamical models: mass-to-light ratio, dark matter, Fundamental Plane and Mass Plane. *Monthly Notices of the Royal Astronomical Society*, 432:1709–1741.

Clemens, D. P. (1985). Massachusetts-Stony Brook Galactic plane CO survey - The Galactic disk rotation curve. *The Astrophysical Journal*, 295:422–428.

Colless, M., Dalton, G., Maddox, S., Sutherland, W., Norberg, P., Cole, S., Bland-Hawthorn, J., Bridges, T., Cannon, R., Collins, C., Couch, W., Cross, N., Deeley, K., De Propris, R., Driver, S. P., Efstathiou, G., Ellis, R. S., Frenk, C. S., Glazebrook, K., Jackson, C., Lahav, O., Lewis, I., Lumsden, S., Madgwick, D., Peacock, J. A., Peterson, B. A., Price, I., Seaborne, M., and Taylor, K. (2001). The 2dF Galaxy Redshift Survey: spectra and redshifts. *Monthly Notices of the Royal Astronomical Society*, 328:1039–1063.

Daddi, E., Bournaud, F., Walter, F., Dannerbauer, H., Carilli, C. L., Dickinson, M., Elbaz, D., Morrison, G. E., Riechers, D., Onodera, M., Salmi, F., Krips, M., and Stern, D. (2010). Very High Gas Fractions and Extended Gas Reservoirs in z = 1.5 Disk Galaxies. *The Astrophysical Journal*, 713:686–707.

Davis, T. A., Bureau, M., Young, L. M., Alatalo, K., Blitz, L., Cappellari, M., Scott, N., Bois, M., Bournaud, F., Davies, R. L., de Zeeuw, P. T., Emsellem, E., Khochfar, S., Krajnović, D., Kuntschner, H., Lablanche, P.-Y., McDermid, R. M., Morganti, R., Naab, T., Oosterloo, T., Sarzi, M., Serra, P., and Weijmans, A.-M. (2011). The ATLAS^{3D} project - V. The CO Tully-Fisher relation of early-type galaxies. *Monthly Notices of the Royal Astronomical Society*, 414:968–984.

Dehnen, W. (2001). Towards optimal softening in three-dimensional N-body codes - I. Minimizing the force error. *Monthly Notices of the Royal Astronomical Society*, 324:273–291.

Dekel, A., Birnboim, Y., Engel, G., Freundlich, J., Goerdt, T., Mumcuoglu, M., Neistein, E., Pichon, C., Teyssier, R., and Zinger, E. (2009). Cold streams in

early massive hot haloes as the main mode of galaxy formation. *Nature*, 457:451–454.

Emsellem, E., Cappellari, M., Krajnović, D., Alatalo, K., Blitz, L., Bois, M., Bournaud, F., Bureau, M., Davies, R. L., Davis, T. A., de Zeeuw, P. T., Khochfar, S., Kuntschner, H., Lablanche, P.-Y., McDermid, R. M., Morganti, R., Naab, T., Oosterloo, T., Sarzi, M., Scott, N., Serra, P., van de Ven, G., Weijmans, A.-M., and Young, L. M. (2011). The ATLAS^{3D} project - III. A census of the stellar angular momentum within the effective radius of early-type galaxies: unveiling the distribution of fast and slow rotators. *Monthly Notices of the Royal Astronomical Society*, 414:888–912.

Fabian, A. C. and Nulsen, P. E. J. (1977). Subsonic accretion of cooling gas in clusters of galaxies. *Monthly Notices of the Royal Astronomical Society*, 180:479–484.

Gavazzi, G., Fumagalli, M., Cucciati, O., and Boselli, A. (2010). A snapshot on galaxy evolution occurring in the Great Wall: the role of Nurture at z = 0. *Astronomy and Astrophysics*, 517:A73.

Gebhardt, K., Bender, R., Bower, G., Dressler, A., Faber, S. M., Filippenko, A. V., Green, R., Grillmair, C., Ho, L. C., Kormendy, J., Lauer, T. R., Magorrian, J., Pinkney, J., Richstone, D., and Tremaine, S. (2000). A Relationship between Nuclear Black Hole Mass and Galaxy Velocity Dispersion. *The Astrophysical Journal*, 539:L13–L16.

Goto, T., Yamauchi, C., Fujita, Y., Okamura, S., Sekiguchi, M., Smail, I., Bernardi, M., and Gomez, P. L. (2003). The morphology-density relation in the Sloan Digital Sky Survey. *Monthly Notices of the Royal Astronomical Society*, 346:601–614.

Hernquist, L. (1992). Structure of merger remnants. I - Bulgeless progenitors. *The Astrophysical Journal*, 400:460–475.

Hernquist, L. and Quinn, P. J. (1988). Formation of shell galaxies. I - Spherical potentials. *The Astrophysical Journal*, 331:682–698.

Hernquist, L. and Springel, V. (2003). An analytical model for the history of cosmic star formation. *Monthly Notices of the Royal Astronomical Society*, 341:1253–1267.

Hinshaw, G., Weiland, J. L., Hill, R. S., Odegard, N., Larson, D., Bennett, C. L., Dunkley, J., Gold, B., Greason, M. R., Jarosik, N., Komatsu, E., Nolta, M. R., Page, L., Spergel, D. N., Wollack, E., Halpern, M., Kogut, A., Limon, M., Meyer, S. S., Tucker, G. S., and Wright, E. L. (2009). Five-Year Wilkinson Microwave Anisotropy Probe Observations: Data Processing, Sky Maps, and Basic Results. *Astrophysical Journal Supplement Series*, 180:225–245.

Bibliography

Hubble, E. (1929). A Relation between Distance and Radial Velocity among Extra-Galactic Nebulae. *Proceedings of the National Academy of Science*, 15:168–173.

Hubble, E. P. (1936). *Realm of the Nebulae*.

Iannuzzi, F. and Athanassoula, E. (2013). The effect of softening on dynamical simulations of galaxies. *Monthly Notices of the Royal Astronomical Society*, 436:1161–1171.

Jansen, R. A., Franx, M., Fabricant, D., and Caldwell, N. (2000). Surface Photometry of Nearby Field Galaxies: The Data. *Astrophysical Journal Supplement Series*, 126:271–329.

Johansson, P. H., Naab, T., and Burkert, A. (2009). Equal- and Unequal-Mass Mergers of Disk and Elliptical Galaxies with Black Holes. *The Astrophysical Journal*, 690:802–821.

Kaufmann, T., Bullock, J. S., Maller, A. H., Fang, T., and Wadsley, J. (2009). Redistributing hot gas around galaxies: do cool clouds signal a solution to the overcooling problem? *Monthly Notices of the Royal Astronomical Society*, 396:191–202.

Kereš, D., Katz, N., Weinberg, D. H., and Davé, R. (2005). How do galaxies get their gas? *Monthly Notices of the Royal Astronomical Society*, 363:2–28.

Komatsu, E., Smith, K. M., Dunkley, J., Bennett, C. L., Gold, B., Hinshaw, G., Jarosik, N., Larson, D., Nolta, M. R., Page, L., Spergel, D. N., Halpern, M., Hill, R. S., Kogut, A., Limon, M., Meyer, S. S., Odegard, N., Tucker, G. S., Weiland, J. L., Wollack, E., and Wright, E. L. (2011). Seven-year Wilkinson Microwave Anisotropy Probe (WMAP) Observations: Cosmological Interpretation. *Astrophysical Journal Supplement Series*, 192:18.

Kravtsov, A., Vikhlinin, A., and Meshscheryakov, A. (2014). Stellar mass – halo mass relation and star formation efficiency in high-mass halos. *ArXiv e-prints*.

Kravtsov, A. V. (2013). The Size-Virial Radius Relation of Galaxies. *The Astrophysical Journal*, 764:L31.

Lees, J. F., Knapp, G. R., Rupen, M. P., and Phillips, T. G. (1991). Molecular gas in elliptical galaxies. *The Astrophysical Journal*, 379:177–215.

Lewis, A., Challinor, A., and Lasenby, A. (2000). Efficient Computation of Cosmic Microwave Background Anisotropies in Closed Friedmann-Robertson-Walker Models. *The Astrophysical Journal*, 538:473–476.

Longair, M. S. (2008). *Galaxy Formation*.

Loubser, S. I., Sánchez-Blázquez, P., Sansom, A. E., and Soechting, I. K. (2009). Stellar populations in the centres of brightest cluster galaxies. *Monthly Notices of the Royal Astronomical Society*, 398:133–156.

Lynden-Bell, D. (1967). Statistical mechanics of violent relaxation in stellar systems. *Monthly Notices of the Royal Astronomical Society*, 136:101.

Mathews, W. G. and Brighenti, F. (2003). Rapid Cooling of Dusty Gas in Elliptical Galaxies. *The Astrophysical Journal*, 590:L5–L8.

McDonald, M., Bayliss, M., Benson, B. A., Foley, R. J., Ruel, J., Sullivan, P., Veilleux, S., Aird, K. A., Ashby, M. L. N., Bautz, M., Bazin, G., Bleem, L. E., Brodwin, M., Carlstrom, J. E., Chang, C. L., Cho, H. M., Clocchiatti, A., Crawford, T. M., Crites, A. T., de Haan, T., Desai, S., Dobbs, M. A., Dudley, J. P., Egami, E., Forman, W. R., Garmire, G. P., George, E. M., Gladders, M. D., Gonzalez, A. H., Halverson, N. W., Harrington, N. L., High, F. W., Holder, G. P., Holzapfel, W. L., Hoover, S., Hrubes, J. D., Jones, C., Joy, M., Keisler, R., Knox, L., Lee, A. T., Leitch, E. M., Liu, J., Lueker, M., Luong-van, D., Mantz, A., Marrone, D. P., McMahon, J. J., Mehl, J., Meyer, S. S., Miller, E. D., Mocanu, L., Mohr, J. J., Montroy, T. E., Murray, S. S., Natoli, T., Padin, S., Plagge, T., Pryke, C., Rawle, T. D., Reichardt, C. L., Rest, A., Rex, M., Ruhl, J. E., Saliwanchik, B. R., Saro, A., Sayre, J. T., Schaffer, K. K., Shaw, L., Shirokoff, E., Simcoe, R., Song, J., Spieler, H. G., Stalder, B., Staniszewski, Z., Stark, A. A., Story, K., Stubbs, C. W., Šuhada, R., van Engelen, A., Vanderlinde, K., Vieira, J. D., Vikhlinin, A., Williamson, R., Zahn, O., and Zenteno, A. (2012). A massive, cooling-flow-induced starburst in the core of a luminous cluster of galaxies. *Nature*, 488:349–352.

McDonald, M., Swinbank, M., Edge, A. C., Wilner, D. J., Veilleux, S., Benson, B. A., Hogan, M. T., Marrone, D. P., McNamara, B. R., Wei, L. H., Bayliss, M. B., and Bautz, M. W. (2014). The State of the Warm and Cold Gas in the Extreme Starburst at the Core of the Phoenix Galaxy Cluster (SPT-CLJ2344-4243). *The Astrophysical Journal*, 784:18.

McNamara, B. R., Rafferty, D. A., Bîrzan, L., Steiner, J., Wise, M. W., Nulsen, P. E. J., Carilli, C. L., Ryan, R., and Sharma, M. (2006). The Starburst in the Abell 1835 Cluster Central Galaxy: A Case Study of Galaxy Formation Regulated by an Outburst from a Supermassive Black Hole. *The Astrophysical Journal*, 648:164–175.

Monaghan, J. J. (1992). Smoothed particle hydrodynamics. *Annual review of astronomy and Astrophysics*, 30:543–574.

Murphy, J. D., Gebhardt, K., and Cradit, M. (2014). The Rising Stellar Velocity Dispersion of M87 from Integrated Starlight. *The Astrophysical Journal*, 785:143.

Naab, T., Jesseit, R., and Burkert, A. (2006). The influence of gas on the structure of merger remnants. *Monthly Notices of the Royal Astronomical Society*, 372:839–852.

Bibliography

Naab, T., Johansson, P. H., and Ostriker, J. P. (2009). Minor Mergers and the Size Evolution of Elliptical Galaxies. *The Astrophysical Journal*, 699:L178–L182.

Naab, T., Oser, L., Emsellem, E., Cappellari, M., Krajnovic, D., McDermid, R. M., Alatalo, K., Bayet, E., Blitz, L., Bois, M., Bournaud, F., Bureau, M., Crocker, A., Davies, R. L., Davis, T. A., de Zeeuw, P. T., Duc, P.-A., Hirschmann, M., Johansson, P. H., Khochfar, S., Kuntschner, H., Morganti, R., Oosterloo, T., Sarzi, M., Scott, N., Serra, P., van de Ven, G., Weijmans, A., and Young, L. M. (2013). The ATLAS$^{\rm{3D}}$ project - XXV: Two-dimensional kinematic analysis of simulated galaxies and the cosmological origin of fast and slow rotators. *ArXiv e-prints*.

Nelson, D., Vogelsberger, M., Genel, S., Sijacki, D., Kereš, D., Springel, V., and Hernquist, L. (2013). Moving mesh cosmology: tracing cosmological gas accretion. *Monthly Notices of the Royal Astronomical Society*, 429:3353–3370.

Oser, L., Ostriker, J. P., Naab, T., Johansson, P. H., and Burkert, A. (2010). The Two Phases of Galaxy Formation. *The Astrophysical Journal*, 725:2312–2323.

Perlmutter, S., Aldering, G., Goldhaber, G., Knop, R. A., Nugent, P., Castro, P. G., Deustua, S., Fabbro, S., Goobar, A., Groom, D. E., Hook, I. M., Kim, A. G., Kim, M. Y., Lee, J. C., Nunes, N. J., Pain, R., Pennypacker, C. R., Quimby, R., Lidman, C., Ellis, R. S., Irwin, M., McMahon, R. G., Ruiz-Lapuente, P., Walton, N., Schaefer, B., Boyle, B. J., Filippenko, A. V., Matheson, T., Fruchter, A. S., Panagia, N., Newberg, H. J. M., Couch, W. J., and Supernova Cosmology Project (1999). Measurements of Omega and Lambda from 42 High-Redshift Supernovae. *The Astrophysical Journal*, 517:565–586.

Ponman, T. J., Allan, D. J., Jones, L. R., Merrifield, M., McHardy, I. M., Lehto, H. J., and Luppino, G. A. (1994). A possible fossil galaxy group. *Nature*, 369:462–464.

Price, D. J. and Monaghan, J. J. (2007). An energy-conserving formalism for adaptive gravitational force softening in smoothed particle hydrodynamics and N-body codes. *Monthly Notices of the Royal Astronomical Society*, 374:1347–1358.

Remus, R.-S., Burkert, A., Dolag, K., Johansson, P. H., Naab, T., Oser, L., and Thomas, J. (2013). The Dark Halo—Spheroid Conspiracy and the Origin of Elliptical Galaxies. *The Astrophysical Journal*, 766:71.

Richstone, D. and Sargent, W. L. W. (1972). A New Determination of the Mass of M32. *The Astrophysical Journal*, 176:91.

Riess, A. G., Filippenko, A. V., Challis, P., Clocchiatti, A., Diercks, A., Garnavich, P. M., Gilliland, R. L., Hogan, C. J., Jha, S., Kirshner, R. P., Leibundgut, B., Phillips, M. M., Reiss, D., Schmidt, B. P., Schommer, R. A., Smith, R. C., Spyromilio, J., Stubbs, C., Suntzeff, N. B., and Tonry, J. (1998). Observational

Evidence from Supernovae for an Accelerating Universe and a Cosmological Constant. *Astronomical Journal*, 116:1009–1038.

Rubin, V. C., Ford, W. K. J., and Roberts, M. S. (1979). Extended rotation curves of high-luminosity spiral galaxies. V - NGC 1961, the most massive spiral known. *The Astrophysical Journal*, 230:35–39.

Scannapieco, C., Wadepuhl, M., Parry, O. H., Navarro, J. F., Jenkins, A., Springel, V., Teyssier, R., Carlson, E., Couchman, H. M. P., Crain, R. A., Dalla Vecchia, C., Frenk, C. S., Kobayashi, C., Monaco, P., Murante, G., Okamoto, T., Quinn, T., Schaye, J., Stinson, G. S., Theuns, T., Wadsley, J., White, S. D. M., and Woods, R. (2012). The Aquila comparison project: the effects of feedback and numerical methods on simulations of galaxy formation. *Monthly Notices of the Royal Astronomical Society*, 423:1726–1749.

Schauer, A. T. P., Remus, R.-S., Burkert, A., and Johansson, P. H. (2014). The Mystery of the σ-Bump—A New Signature for Major Mergers in Early-type Galaxies? *The Astrophysical Journal*, 783:L32.

Sonnenfeld, A., Treu, T., Gavazzi, R., Marshall, P. J., Auger, M. W., Suyu, S. H., Koopmans, L. V. E., and Bolton, A. S. (2012). Evidence for Dark Matter Contraction and a Salpeter Initial Mass Function in a Massive Early-type Galaxy. *The Astrophysical Journal*, 752:163.

Springel, V. (2005). The cosmological simulation code GADGET-2. *Monthly Notices of the Royal Astronomical Society*, 364:1105–1134.

Springel, V., White, S. D. M., Jenkins, A., Frenk, C. S., Yoshida, N., Gao, L., Navarro, J., Thacker, R., Croton, D., Helly, J., Peacock, J. A., Cole, S., Thomas, P., Couchman, H., Evrard, A., Colberg, J., and Pearce, F. (2005). Simulations of the formation, evolution and clustering of galaxies and quasars. *Nature*, 435:629–636.

Springel, V., White, S. D. M., Tormen, G., and Kauffmann, G. (2001a). Populating a cluster of galaxies - I. Results at [formmu2]z=0. *Monthly Notices of the Royal Astronomical Society*, 328:726–750.

Springel, V., Yoshida, N., and White, S. D. M. (2001b). GADGET: a code for collisionless and gasdynamical cosmological simulations. *Nature*, 6:79–117.

Teyssier, R. (2002). Cosmological hydrodynamics with adaptive mesh refinement. A new high resolution code called RAMSES. *Astronomy and Astrophysics*, 385:337–364.

Thomas, J., Saglia, R. P., Bender, R., Thomas, D., Gebhardt, K., Magorrian, J., Corsini, E. M., and Wegner, G. (2007). Dynamical modelling of luminous and dark matter in 17 Coma early-type galaxies. *Monthly Notices of the Royal Astronomical Society*, 382:657–684.

Tormen, G., Bouchet, F. R., and White, S. D. M. (1997). The structure and dynamical evolution of dark matter haloes. *Monthly Notices of the Royal Astronomical Society*, 286:865–884.

van de Sande, J., Kriek, M., Franx, M., van Dokkum, P. G., Bezanson, R., Bouwens, R. J., Quadri, R. F., Rix, H.-W., and Skelton, R. E. (2013). Stellar Kinematics of z ~ 2 Galaxies and the Inside-out Growth of Quiescent Galaxies. *The Astrophysical Journal*, 771:85.

van Dokkum, P. G., Franx, M., Kriek, M., Holden, B., Illingworth, G. D., Magee, D., Bouwens, R., Marchesini, D., Quadri, R., Rudnick, G., Taylor, E. N., and Toft, S. (2008). Confirmation of the Remarkable Compactness of Massive Quiescent Galaxies at z ~ 2.3: Early-Type Galaxies Did not Form in a Simple Monolithic Collapse. *The Astrophysical Journal*, 677:L5–L8.

Wei, L. H., Kannappan, S. J., Vogel, S. N., and Baker, A. J. (2010). Gas Mass Fractions and Star Formation in Blue-Sequence E/S0 Galaxies. *The Astrophysical Journal*, 708:841–861.

Young, L. M., Bureau, M., Davis, T. A., Combes, F., McDermid, R. M., Alatalo, K., Blitz, L., Bois, M., Bournaud, F., Cappellari, M., Davies, R. L., de Zeeuw, P. T., Emsellem, E., Khochfar, S., Krajnović, D., Kuntschner, H., Lablanche, P.-Y., Morganti, R., Naab, T., Oosterloo, T., Sarzi, M., Scott, N., Serra, P., and Weijmans, A.-M. (2011). The ATLAS^{3D} project - IV. The molecular gas content of early-type galaxies. *Monthly Notices of the Royal Astronomical Society*, 414:940–967.

Young, L. M., Scott, N., Serra, P., Alatalo, K., Bayet, E., Blitz, L., Bois, M., Bournaud, F., Bureau, M., Crocker, A. F., Cappellari, M., Davies, R. L., Davis, T. A., de Zeeuw, P. T., Duc, P.-A., Emsellem, E., Khochfar, S., Krajnovic, D., Kuntschner, H., McDermid, R. M., Morganti, R., Naab, T., Oosterloo, T., Sarzi, M., and Weijmans, A.-M. (2013). The Atlas3D project – XXVII. Cold Gas and the Colours and Ages of Early-type Galaxies. *ArXiv e-prints*.

Acknowledgements

I wish to thank all the people who supported me during my work on this thesis.

First of all I would like to thank Prof. Andreas Burkert for providing me with this interesting topic, giving me the opportunity to write my masters thesis in his CAST group, and for many helpful discussions. It was a real pleasure to be part of such an interesting working group.

I also want to thank PD. Dr. Klaus Dolag, without whom it would not have been possible to perform the simulations which are the basis of this work. He introduced me to the GADGET-3 and ZIC codes, helped me through many ups and downs with the code, and made lots of helpful suggestions and good coffee.

Furthermore, I want to thank Dr. Alexander Beck and Rhea-Silvia Remus for many fruitful discussions on scientific and simulation matters. Their excitement about my work had significant part in its development. Thanks are due to Florian Stecker as well for finding my galaxies in the voids of Dianoga, and to Tadziu Hoffmann for all matters concerning failing computers. I also want to thank my fellow Master Students Anna Schauer, Stefan Heigl, Lisa Bachmann and Adelheid Teklu for the fun and the shared discussions.

Finally, last but not least, I want to thank my family for their love and support in good and difficult times. They always were of great help.

Selbstständigkeitserklärung

Hiermit versichere ich, die vorliegende Arbeit selbstständig verfasst zu haben. Ich habe keine anderen als die in der Arbeit angegebenen Quellen und Hilfsmittel benutzt.

Mir ist bekannt, dass Zuwiderhandlung auch nachträglich zur Aberkennung des Abschlusses führen kann.

München, May 15, 2014